First Annual Report for RWM participation in DECOVALEX-2015 Tasks A and C1

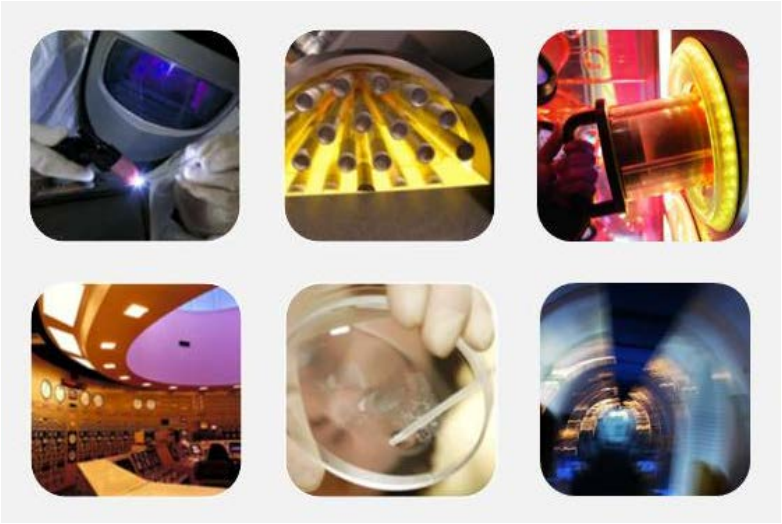

Technical Report

RWM Coupled Processes Project

First Annual Report for RWM participation in DECOVALEX-2015 Tasks A and C1

Alex Bond, Kate Thatcher, Neil Chittenden – Quintessa Ltd
Chris McDermott, Andrew Fraser-Harris – University of Edinburgh

AMEC Report Reference	18040-TR-002
Client Reference	RWMD/03/020
Client Name	RWM
Issue Number	Version 2.1
Report Date	09/07/2014

Document Issue Record

Document title	RWM Coupled Processes Project: First Annual Report for RWM participation in DECOVALEX-2015 Tasks A and C1
Project Reference	18040
Quintessa Reference	QRS-1612A-R1-v2.1

Purpose of Issue	Final approved version
Security Class	Official

Issue	Description	Originator	Checker	Approver	Date dd/mm/yy
Issue 1 Draft 1	First draft for comment. (Unapproved)	AE Bond	P Robinson		22/07/2013
Issue 2 Draft 1	First draft of second version for checking, following review from RWM, BGS and Amphos21	AE Bond	P Robinson		27/02/2014
Issue 2	Internally reviewed and approved	AE Bond	P Robinson	A Guida	13/05/2014
Issue 2.1 Final	Updated following comments from RWM	AE Bond	P Robinson	A Guida	09/07/2014

Previous issues of this document shall be destroyed or marked **SUPERSEDED**.

This report has been prepared by AMEC Nuclear UK Ltd under contract to the Nuclear Decommissioning Authority (NDA), Radioactive Waste Management Directorate (RWMD) and forms part of an ongoing programme of research commissioned by NDA RWMD to underpin the long-term safety of a geological disposal facility for higher-activity radioactive wastes. Before it was published RWMD became a wholly owned subsidiary of the NDA (on 1 April 2014) called Radioactive Waste Management Limited.

The report has been reviewed by Radioactive Waste Management Limited. However, references to NDA and RWMD in the text have been retained as they are appropriate for the period when this research was being performed. The views expressed and conclusions drawn in this report are those of AMEC Nuclear UK Ltd and do not necessarily represent those of the NDA RWMD or Radioactive Waste Management Limited.

Conditions of publication

Bibliography

If you would like to see other reports available from Radioactive Waste Management Limited and the NDA, a complete listing can be viewed at our website www.nda.gov.uk, or please write to our Communications department at the address below.

Feedback

Readers are invited to provide feedback to the Radioactive Waste Management Limited on the contents, clarity and presentation of this report and on the means of improving the range of reports published. Feedback should be addressed to:

Head of Stakeholder Engagement and Communications
Radioactive Waste Management Limited
Building 587
Curie Avenue
Harwell Oxford
Didcot
OX11 0RH
UK

Email: rwmdfeedback@nda.gov.uk

Preface

Radioactive Waste Management Limited (RWM) is responsible for implementing geological disposal of higher-activity radioactive wastes in the UK. RWM's research into geological disposal considers safety during waste transport to a disposal facility, during waste disposal operations, and once the facility has been closed.

RWM's Coupled Processes Project comprises three tasks:

Task A: Participation in DECOVALEX-2015 Case Study A.

Task C: Participation in DECOVALEX-2015 Case Study C1.

Task 3: General Support to RWM on Coupled Processes

Tasks A and C provide for the contractor team to work with RWM on two case studies that form part of the DECOVALEX-2015 international applied research project. DECOVALEX – DEvelopment of COupled models and their VALidation against EXperiments – has been running continuously since 1992 in a series of six phases, and the current phase (2012-2015) encompasses modelling of thermal-hydrological-mechanical-chemical (THMC) process couplings based on results from *in situ* and laboratory experiments.

Task 3 provides for the contractor team to work with RWM to understand and document what work has been done on coupled processes as part of the UK programme, to understand approaches for treating coupled processes in performance assessments in overseas programmes, and to make recommendations for the RWM forward programme.

Work on the RWM's Coupled Processes Project is being undertaken by a team of organisations that together have substantial experience of the UK programme for management of higher-activity radioactive wastes and with the evaluation of coupled processes associated with geological disposal of these wastes.

AMEC is responsible for project management of the contractor team. Galson Sciences Ltd is responsible for managing the technical work programme and leading technical activities on Task 3, review of coupled processes in the UK programme and in overseas performance assessments, and advice on research requirements. Quintessa Ltd is responsible for managing the technical work programme and leading technical activities on Tasks A and C1, participation in case studies A and C1 of the international DECOVALEX project on coupled processes.

Quintessa Ltd prepared this report with support from the University of Edinburgh; it records work completed during the first year of the DECOVALEX-2015 project by the team funded by RWM.

Executive Summary

Radioactive Waste Management Limited is responsible for implementing geological disposal of the UK's higher-activity radioactive wastes. RWM's research into geological disposal considers safety during waste transport to a disposal facility, during waste disposal operations, and once the facility has been closed.

Coupled processes have been acknowledged by RWM and the wider international radioactive waste management community as being of potential major significance in the assessment of post-closure safety for geological disposal facilities (GDFs) for radioactive waste. The aim of RWM's Coupled Processes Project is to support RWM in addressing coupled process sets and understanding their potential significance to the assessments of post-closure safety that underpin the environmental safety case (ESC), site investigations, and design of a GDF in the UK.

RWM's Coupled Process Project comprises support for the contractor team to work with RWM on two case studies that form part of the DECOVALEX-2015 international applied research project on coupled processes, and a third task to provide general support to RWM on coupled processes.

This report provides an overview of the technical work completed by the RWM team during the first year of DECOVALEX-2015 under Task A (coupled hydraulic-mechanical behaviour of bentonite seals) and Task C1 (coupled thermal-hydraulic-mechanical-chemical evolution of single fractures), however it is not a general record of the progress made under Task A and C1. The report shows that good progress has been made, and the overall objectives of the project are expected to be met over the three-and-a-half years duration of DECOVALEX-2015.

Production of annual progress reports throughout the DECOVALEX-2015 project will ensure that the work funded by RWM is presented in the open literature in a timely manner as the project progresses. This will enhance transparency and enable the reader to understand the capabilities available to RWM in relation to the treatment of coupled processes in GDF relevant studies. It is also important in maintaining RWM's knowledge base, as reflected in the Status Reports.

Contents

Preface ..... **iv**
Executive Summary ..... **v**
List of Terms and Abbreviations ..... **viii**
1 Introduction **1**
1.1 Background and Objectives 1
1.2 Approach and Scope 2
1.3 Report Structure 3
2 Task A – SEALEX Experiment **4**
2.1 Task Overview 4
2.1.1 SEALEX Experiment 4
2.1.2 Task A Structure 8
2.1.3 Step 0 10
2.1.4 Step 1 12
2.2 Bentonite Overview 14
2.2.1 Bentonite (Montmorillonite) Structure 14
2.2.2 Forces and Bonds in Bentonite 17
2.2.3 Key Aspects 17
2.3 Approach to Task A 18
2.4 Step 0 19
2.4.1 Water Retention Curve 19
2.4.2 Oedometer Tests 23
2.4.3 Infiltration Test 29
2.5 Step 1 36
2.5.1 Approach 36
2.5.2 Semi-quantitative Predictions 37
2.5.3 Quantitative Predictions 38
2.5.4 Results 40
2.5.5 Comparison against Step 1 Predictions 45
2.6 Beginnings of a New Constitutive Model 45
2.6.1 Overview of Existing Model Approaches 46
2.6.2 New Proposed Non Linear Elastic Model Approach 47
2.7 Task A Summary 50
3 Task C – THMC processes in single fractures **51**
3.1 Task Overview 51
3.1.1 Experimental Overview 51
3.1.2 Novaculite Experiment 52
3.1.3 Granite Experiment 55
3.1.4 Task Structure 56

3.2 Approach to Task C1 57
3.3 Step 0 58
3.3.1 Geochemical Model 58
3.3.2 Geochemical Benchmark 63
3.3.3 High Resolution Approach for Step 0 64
3.3.4 Homogenised Approach for Step 0 80
3.4 Step 1 89
3.5 Task C Summary 92
4 Conclusions of the first year of DECOVALEX-2015 work by the AMEC team 93
4.1 Summary of Progress 93
4.2 Issues of Potential Significance to RWM 93
4.3 Way Forward 94
5 References 95
Appendix A . OpenGeoSys Formulation and Implementation of HMC model 101
A.1 Overview 101
A.2 Implementation of the Finite Element Scheme in OpenGeoSys 102
A.3 Task C: Implementation of the H(MC) analytical closure solution in OpenGeoSys 105
Appendix B – QPAC Formulation 108
B.1 System Discretisation 108
B.2 Process Models and Variables 109
B.3 The Finite Volume Method 110
B.4 Modules 112

List of Terms and Abbreviations

BBM	Barcelona Basic Model for swelling clays
BExM	Barcelona Expansive Model for swelling clays
Cam-Clay	A standard mechanical model for clays
Darcy Flow	Flow of a fluid through porous media where the flow rate is proportional to the pressure gradient
DECOVALEX	DEvelopment of COupled models and their VALidation against EXperiments
DDL	Diffuse Double Layer. In the context of bentonite this relates to the layer of anions and cations in water around the perimeter of a bentonite grain with excess positive charge.
FEBEX	Full-scale Engineered Barriers EXperiment at Grimsel, Switzerland
GDF	Geological Disposal Facility
HLW	High-level (heat generating) Waste
ILW	Intermediate-level (low-heat generating) Waste
LLW	Low-level Waste
IRSN	Institute for Radiological Protection and Nuclear Safety in France
MCC	Modified Cam-Clay. Constitutive mechanical model for clays based on critical state theory, modified to be more suitable for numerical analysis.
MX-80	A commercial formulation of bentonite-rich clay
MRWS	Managing Radioactive Waste Safely programme
MPF	Multi-Phase-Flow: QPAC module
Novaculite	Rock formation consisting dominantly of micro-crystalline quartz found in the Ouachita Mountains of Arkansas and Oklahoma and in the Marathon Uplift of Texas
Oedometer	Laboratory tool for loading soil samples and measuring deformation
OpenGeoSys	Open source coupled modelling code
OGS	OpenGeoSys
QPAC	Coupled-modelling code developed by Quintessa
Saturation	Fractional volume of pore space occupied by a given fluid.
Suction / Capillary Pressure	Difference in pressures between immiscible fluids in a partially saturated porous medium. The variation with saturation is termed the [Water] Retention Curve or Capillary Curve.
SEALEX	Long term engineered seal experiment at the Tournemire URL
SEM	Scanning Electron Microscope

Technological Void	A term from Task A referring to the gap between the seal and the containing structure caused by the limitations of technology when constructing the test
THMC	Thermal-Hydraulic-Mechanical-Chemical coupled processes
UoE	University of Edinburgh
URL	Underground Rock/Research Laboratory
Void Ratio	Ratio of voids volume to solid volume in a given rock or soil sample
Water Content	The mass of water divided by the mass of solid in a given volume of porous medium
Wood's Metal	Metal alloy with a low melting point of approximately 70°C

1 Introduction

1.1 Background and Objectives

As part of its Managing Radioactive Waste Safely (MRWS) programme, the UK Government issued a White Paper in June 2008 setting out a framework for implementing geological disposal of the UK's higher-activity radioactive waste (Defra *et al.* 2008). Radioactive Waste Management Limited, a wholly owned subsidiary of the Nuclear Decommissioning Authority (NDA), is responsible for managing the delivery of geological disposal of higher-activity radioactive wastes. Higher-activity radioactive wastes include high-level waste (HLW), intermediate-level waste (ILW), and the small fraction of low-level waste (LLW) that cannot be managed under the UK Government policy for the long-term management of the UK's solid LLW. In addition to these wastes, spent fuel (SF), separated plutonium (Pu) and separated uranium (U) may need to be managed through geological disposal, and are included in a Baseline Inventory, which is an estimate of the current waste inventory and materials that may need to be treated as waste in the future.

Coupled processes have been acknowledged by RWM and the wider international radioactive waste management community as being of potential major significance in assessing the post-closure safety of a GDF. In addition, the Government's Committee on Radioactive Waste Management (CoRWM) has commented on the research requirements associated with coupled processes (e.g. CoRWM 2009, paragraph A.74) and has questioned the sufficiency of the UK skills basis in this area (CoRWM 2009, paragraph 4.45). The issue of coupled processes has also been commented on by several other reviewers of the RWM work programme, and considerations about coupled processes are an important component of several of the "issues" identified within RWM's issues register (NDA RWMD 2012), as follows:

- Engineered barrier resaturation.
- Long-term cement backfill evolution.
- Impact of coupled thermal, hydrogeological, and chemical processes.
- Evolution of the geosphere.

With this as background, the aim of RWM's Coupled Processes Project is to support RWM's efforts in addressing coupled process sets and understanding their potential significance to the assessments of post-closure safety that underpin the environmental safety case (ESC). The Coupled Processes Project comprises three tasks:

Task A: Participation in DECOVALEX-2015 Case Study A.

Task C: Participation in DECOVALEX-2015 Case Study C1.

Task 3: General Support to RWM on Coupled Processes

Tasks A and C provide for the contractor team to work with RWM on two case studies that form part of the DECOVALEX-2015 international applied research project. DECOVALEX – DEvelopment of COupled models and their VALidation against EXperiments – has been running continuously since 1992 in a series of six phases, and the current phase (2012-

2015) encompasses modelling of thermal-hydrological-mechanical-chemical (THMC) couplings based on results from *in situ* and laboratory experiments.

The present phase of the DECOVALEX project (2012-2015) was launched in 2012. RWM is involved in Tasks A and C of DECOVALEX-2015:

- Task A focuses on the SEALEX project, which involves emplacement of a clay-based seal at the Tournemire URL. The objectives are to investigate the hydraulic performance for different chemical and physical forms of the clay, the impact of construction on hydraulic properties, and the impact of incomplete saturation on swelling pressure. The task considers a series of 'steps' starting with smaller, laboratory-based experiments, before moving on to modelling the full-scale emplacements. The steps involve attempting to understand and represent experimental results using numerical models, and then using those models in blind predictions at the laboratory and field-scale.

- The objective of Task C is to examine THMC process couplings in single fractures in low permeability, low porosity ('high strength') host rocks, with a data set based on two historical laboratory experiments. The experiments consist of single fractures where mechanical loading, groundwater chemistry and thermal characteristics were varied, and water outflow rates or pressure gradients, out-flowing geochemistry, and mechanical load response were measured. Models produced as a result of this work will be one of very few attempts at THMC coupling in fractured media (e.g. Taron et al. 2009).

Compacted and pelletized bentonite is an important material for many international radioactive waste disposal concepts (e.g. SKB 2011; Nagra, 2002; Andra 2005). Its low intrinsic permeability on compaction and high degree of swelling during resaturation can make it attractive for use as a hydraulic seal, bulk backfill (often as part of a mixture with sand or crushed rock) and as a buffer around individual waste packages.

1.2 Approach and Scope

This report provides an overview of the technical progress made through the first year of DECOVALEX-2015 (April 2012 to April 2013). The information presented here represents the status of the work as presented at the DECOVALEX workshop hosted in the Republic of Korea in April 2013. It should be noted that the report does not attempt to present a chronological progress report, but rather discusses the present status of work against the separate project components ('Steps') under each Task at the time of writing. The report also only discusses the work of the RWM team and does not attempt to discuss the work from other contributors to the respective Tasks.

It should be noted that the Tasks, at present, are relatively independent in terms of their technical work and so are discussed quite separately.

1.3 Report Structure

The remainder of this report is structured as follows:

- Section 2 provides an overview of Task A and the technical work conducted under it, specifically results for Step 0 and 1. This is then followed by an outline of the expected way forward for the following twelve months.

- Section 3 provides an overview of Task C1 and the technical work conducted under it, primarily Step 0 and some early work for Step 1. This is then followed by an outline of the expected way forward for the following twelve months.

- Section 4 provides a summary of progress, the main themes for work going forward and highlights any issues of potential significance to RWM.

2 Task A – SEALEX Experiment

2.1 Task Overview

2.1.1 SEALEX Experiment

The SEALEX experiment is a field-scale investigation into geological disposal facility (GDF) engineered seal performance, currently underway at the Tournemire Underground Rock Laboratory (URL). The Tournemire URL is a railway tunnel constructed approximately 125 years ago through the Larzac Plateau in the south of France close to Rochefort and Tournemire (see Figure 2.1, Figure 2.2). No longer in use as a railway tunnel, since 1992 the tunnel has been owned and operated by IRSN, the principal French nuclear regulatory organisation, as an experimental facility.

The URL is primarily constructed in the Toarcian argillite, an indurated clay formation consisting of shales and marls, with a very low permeability to saturated water flow. The formation shares many characteristics of other indurated clays being considered for radioactive waste disposal, such as the Callo-Oxfordian argillite and the Opalinus Clay, being of low intrinsic permeability (~1e-21 – 1e-18 m^2), significant porosity (~9%) and with a strong tendency to show hydraulic 'self-sealing' characteristics post excavation.

The SEALEX experiments are being conducted in a new drift (Figure 2.3) away from the main tunnel.

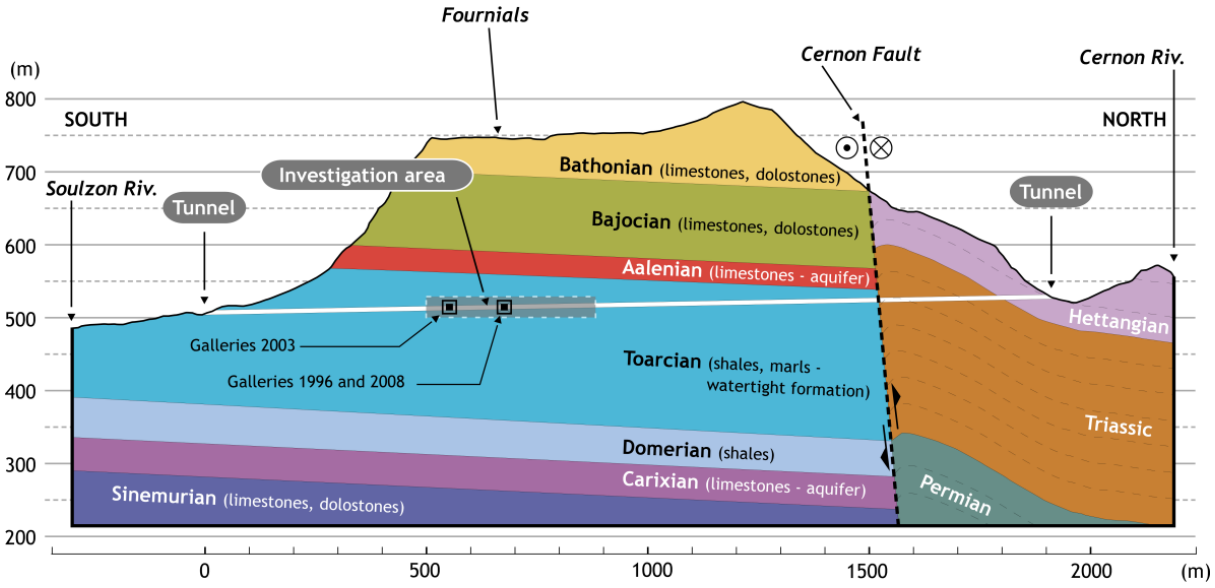

Figure 2.1 Geological section along the line of the Tournemire URL tunnel (IRSN, 2012).

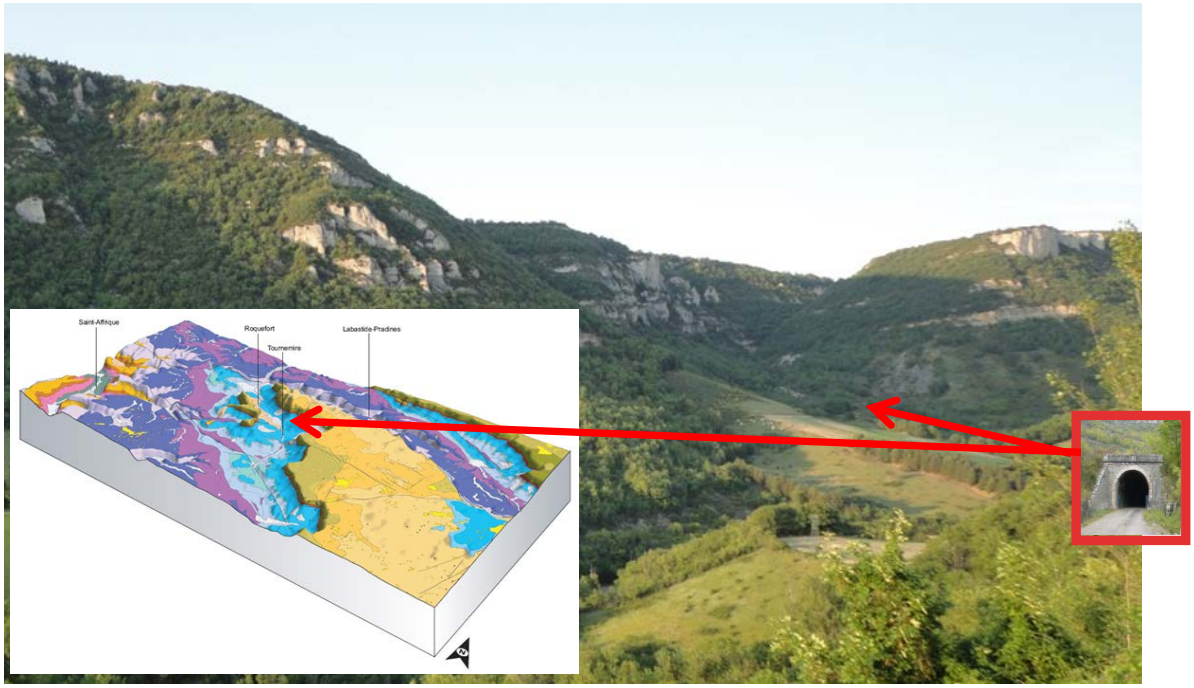

Figure 2.2 View of the southern side of the tunnel and (inset) the geology exposure of the Larzac Plateau, southern entrance marked in both cases (IRSN, 2012)

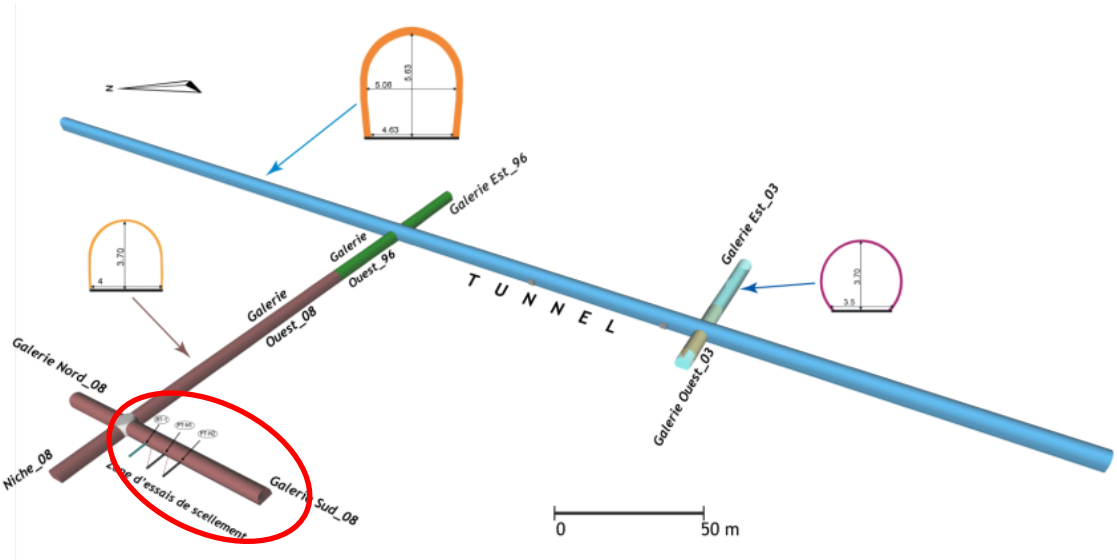

Figure 2.3 View of the Tournemire URL with the SEALEX experimental gallery marked in with the red ellipse (IRSN, 2012).

The main motivations for the experiment are as follows:

- Evaluation of the main perturbations caused by the installation of the seals and their influence on the radioactive waste confinement properties of the other geological disposal components, in this case primarily the host rock.
- Evaluate the technical feasibility of seals with respect to their:
    - Safety functions
    - Expected performance level (e.g. overall hydraulic conductivity).

The desired outcome of the experiment is to be able to understand and predict the overall performance of the clay seals, over the long-term, for a range of different evolution and installation conditions:

- Reference design and under expected evolution conditions
- For different technological choices (e.g. bentonite mix, installation method)
- In altered situations (e.g. loss of mechanical confinement).

The experimental approach involves the installation of a series of mocked-up seals in 60 cm boreholes drilled horizontally into the sides of the gallery. The seals were chosen to be this size in order that they are large enough to be considered 'field scale' and also because they are of a similar size and geometry to the seals currently considered in the ANDRA concept for plugging the end of HA (high activity, heat generating waste) horizontal deposition holes.

Two configurations of seal installation and instrumentation are considered – the so-called 'Reference Test' and the 'Performance Test'. The purpose of reference tests is to examine the interaction of the bentonite seal with the argillite host rock using conventional wired sensors. In contrast, following flooding of the 'technological voids' (engineered gaps) around the seals with water, and enhanced resaturation with a constant supply of water at the tunnel end of the seal, the performance tests were designed to enable the application of an induced hydraulic gradient across the seal in order to test the hydraulic performance of the installed seal. To this end, the performance tests use wireless sensors to avoid disturbing the installed seal, while the reference tests use a higher number of wired sensors.

For both tests the seals are isolated hydraulically and mechanically from the main tunnel drift via the use of hydraulic packers and fixed concrete, steel and epoxy confining structures (Figure 2.4, Figure 2.5). Initial resaturation of both types of test is achieved through flooding of the annular void around the seal with water (the void is required in order to get the seal in place) and then supplying water through one or both axial faces of the seal. The permeability of the intact host rock is such that natural resaturation would take too long for experimental purposes, hence the need for artificial resaturation. For the performance tests, once water saturation has advanced sufficiently, the hydraulic testing of the seal can then take place.

Current and future installations are shown in Figure 2.6. Monitoring of the installed experiments is expected to last at least a decade from the installation date.

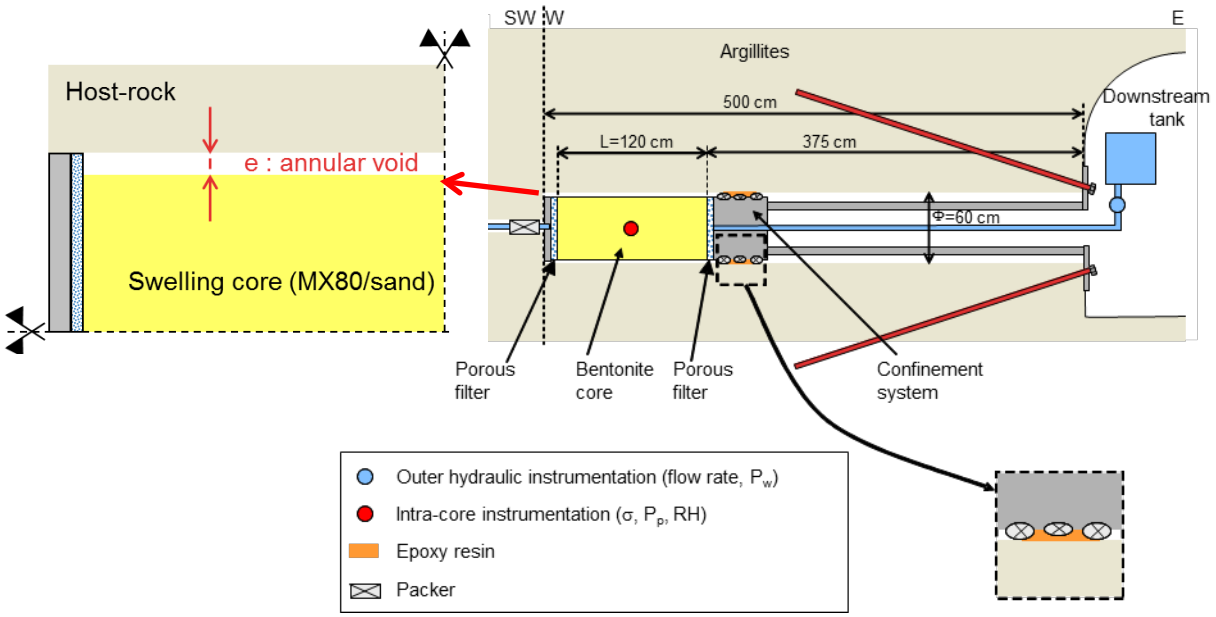

Figure 2.4. Schematic illustration of the experimental arrangement for a single seal (IRSN, 2012)

Reference Test configuration

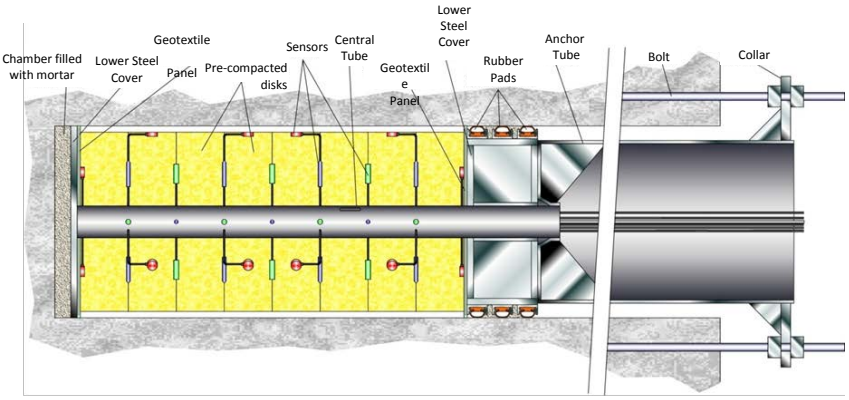

Performance Test configuration

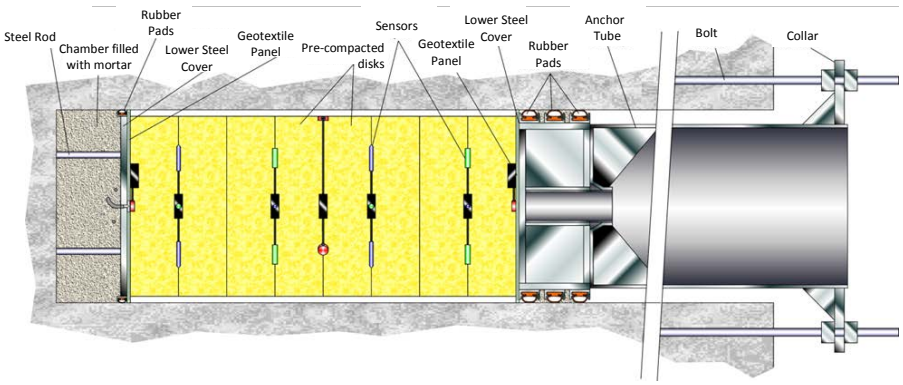

Figure 2.5. Arrangements for the reference tests (top) and performance tests (bottom) (modified from IRSN, 2012)

	Reference Tests	Performance Tests	Intra-core geometry Core conditioning Composition (MX80/sand)	Core view	Altered conditions	Emplacement date
Base case	RT-1	PT-N1	Monolithic disks Precompacted (70/30)		No	12/2010 06/2011
Variations / Base case	-	PT N2	Disks + internal joints (4/4) Precompacted (70/30)	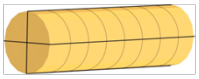	No	12/2011
	-	PT A1	Monolithic disks Precompacted (70/30)		Confinement loss	06/2012
	-	PT-N3	Pellets/powder In situ compacted (100/0)	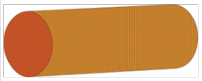	No	01/2013
	-	PT-N4	Pellets/powder In situ compacted (100/0)		Confinement loss	*09/2013*

Figure 2.6. Experimental schedule for the SEALEX experiment (IRSN, 2012). Black text indicates base case experiments and red text show variant experiments.

One further experiment was also conducted; WT-1, the water injection test. This experiment hydraulically seals and then injects water directly into the end of one of the mocked-up deposition holes, monitoring the injected quantity of water and pressure response between the confinement system and the host rock; no bentonite is involved in this test. The data can then be interpreted to derive field-scale hydraulic properties for the argillite. The determination of such hydraulic properties using these experimental results (intrinsic permeability and potential variation with time, storativity) is one of the exercises within Task A, with particular interest in evidence for temporal evolution of hydraulic properties.

2.1.2 Task A Structure

The present structure of the Task is itemised below. In essence, the task is divided into a series of Steps, each of which represents a significant change of emphasis or increase in complexity. The structure of the Steps is specified such that participating teams can build experience and improve modelling tools on more constrained data before culminating in attempting to model the large-scale, complex cases in the final part of the project. The Task structure (as administered by IRSN) is as follows.

- **Step 0**: Modelling of the bentonite/sand mixture hydro-mechanical (HM) behaviour, parameter identification from various laboratory 'unit' tests:
    - Water retention curve (free swelling and confined).
    - 1D confined infiltration test

  - Oedometer swelling and compaction testing

- **Step 1**: Modelling of the 1/10th mock-up (laboratory test). Blind prediction using model & parameters obtained in Step 0.
- **Step 2**: Modelling of the hydraulic behaviour of the rock surrounding the bentonite-sand plug, based on results of the WT-1 in-situ test.
- **Step 3**: Modelling of the in situ PT-N2 test.
- **Step 4**: Modelling of the in situ PT-A1 test

The RWM team is one of 5 teams contributing to the progress of the task. The presence of such a wide range of experience, approaches and expertise working on the same task in a cooperative manner is a key benefit of the DECOVALEX style project approach in that it maximises the opportunity for genuine progress in addressing such complex cross-disciplinary problems. The current participants under Task A are:

- IRSN (internal technical team and also managers of the Task)
- CNSC (Canada), funded by IRSN
- Quintessa and the University of Edinburgh, funded by RWM
- UGN (Czech Republic), funded by RAWRA
- US NRC (internal technical team)

This document only reports the work of the RWM team, but some comments will be made on other teams' approaches where appropriate.

The initial schedule for this work is shown in Figure 2.7. At this early point in the project teams were only expected to have attempted Step 0 and Step 1. The detailed specification of work for Step 0 and Step 1 is given in Millard and Barnichon (2013), but a brief overview is given in the following sections. It should be noted that as of the DECOVALEX meeting at the end of April 2013, a decision was made to delay the start of Step 2 and continue with Step 1 until at least the next meeting in November 2013 to allow the Step 1 data to be incorporated into the Step 0 models.

The PhD programme of work is designed to complement the RWM effort in supporting Task A, but will be largely independent of the milestones shown in Figure 2.7. It is intended that key outputs from the PhD will be incorporated into the Task A work as appropriate and presentations of progress will be given to the DECOVALEX project at key points throughout the PhD programme.

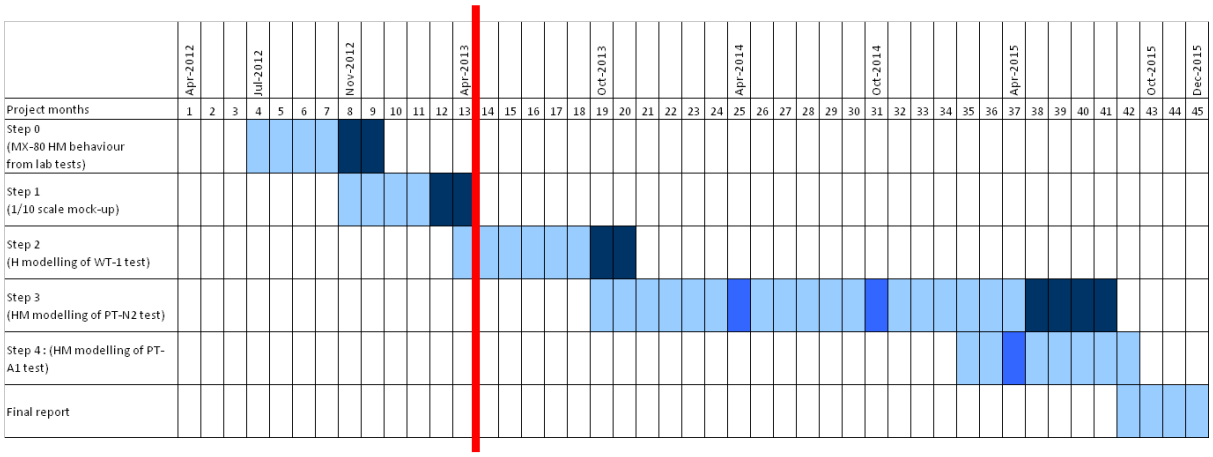

Figure 2.7. Initial schedule for Task A, DECOVALEX-2015 (from IRSN, 2012). The red-line indicates end of April 2013. It should be noted that as of the DECOVALEX meeting at the end of April 2013 a decision was made to delay the start of Step 2 and continue with Step 1 until at least the next meeting in November 2013 to allow the Step 1 data to be incorporated into the Step 0 models.

2.1.3 Step 0

Step 0 involves teams attempting to calibrate numerical models against three separate, but related experiments on 70:30 bentonite:sand mixtures with an initial water content of 11% by mass. This initial water content of the sample was determined to be approximately equivalent to 64 MPa of suction pressure. The three sets of experiments are as follows:

1. **Water retention curve**: The suction potential of 1.67 Mg/m^3 bentonite/sand samples are measured under different degrees of water content for unconfined (free swell) and fully confined (no net volume change) conditions (Figure 2.8).

2. **Oedometer testing**: This is a conventional soil mechanics testing method whereby a small sample is placed in a confining cylinder where both the relative humidity (and hence water suction and water content) of the sample can be controlled, and different axial loads can be applied. As the suction and axial loading are adjusted the change in volume of the sample (through axial volume changes) can be measured (see Figure 2.9). Such tests were run on three samples with an initial dry density of 1.67 Mg/m^3 at suctions of 4.2, 12.6 and 38 MPa. A further test was run on a sample of initial dry density of 1.97 Mg/m^3, with an applied suction of 0 MPa (assumed by the experimentalists to be fully water saturated), however the initial sample was smaller than the radius of the oedometer cylinder so that the sample can expand radially as well as vertically on hydration. Each sample was equilibrated to the specified suction, and then underwent a single loading and unloading cycle.

3. **Infiltration testing**: A 200 mm tall cylinder of 1.67 Mg/m^3 bentonite:sand mixture is mechanically confined, water made available at atmospheric pressure at the base of the sample causing the sample to re-hydrate. Relative humidity (and hence suction) is measured at four locations up the cylinder (see Figure 2.10).

The intention by the task organisers is that the three experiments give data on hydro-mechanical behaviour across a range of suctions and that by building and calibrating models to the experimental data, teams would be able to model later experiments and provide blind predictions, most notably against Step 1.

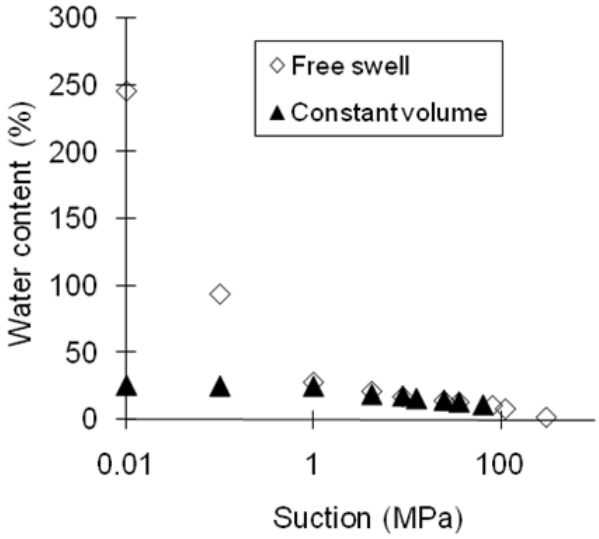

Figure 2.8. Water retention curve data supplied for Step 0 (from Millard and Barnichon, 2013). Note that water content as defined here is the mass of water divided by the mass of solid in a given volume.

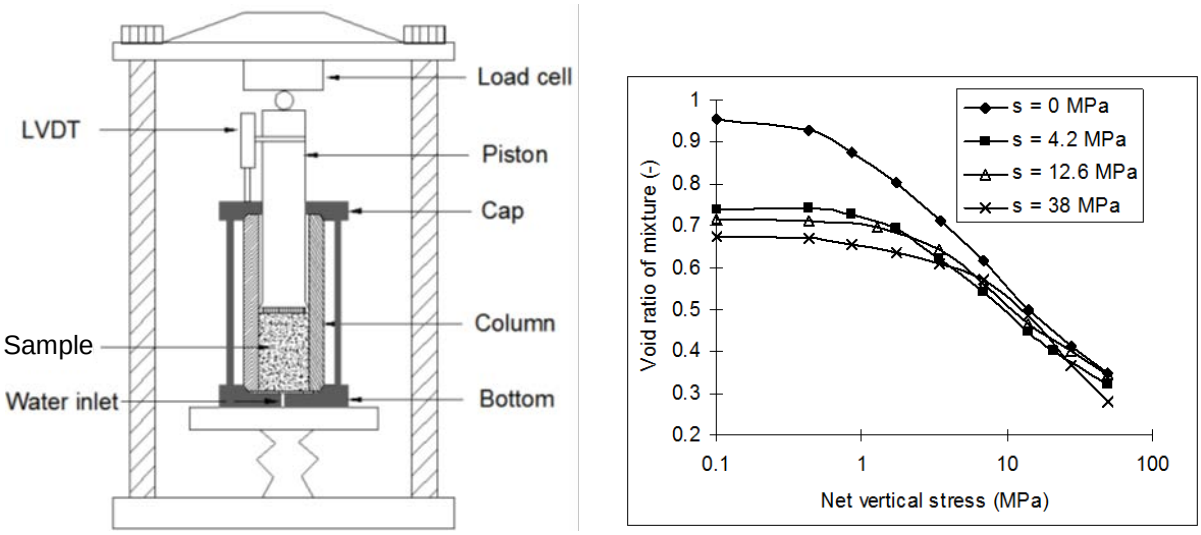

Figure 2.9. Schematic illustration of the oedometer used in Step 0 (left) and the compression phase results only for the four samples (right) from (Millard and Barnichon, 2013)

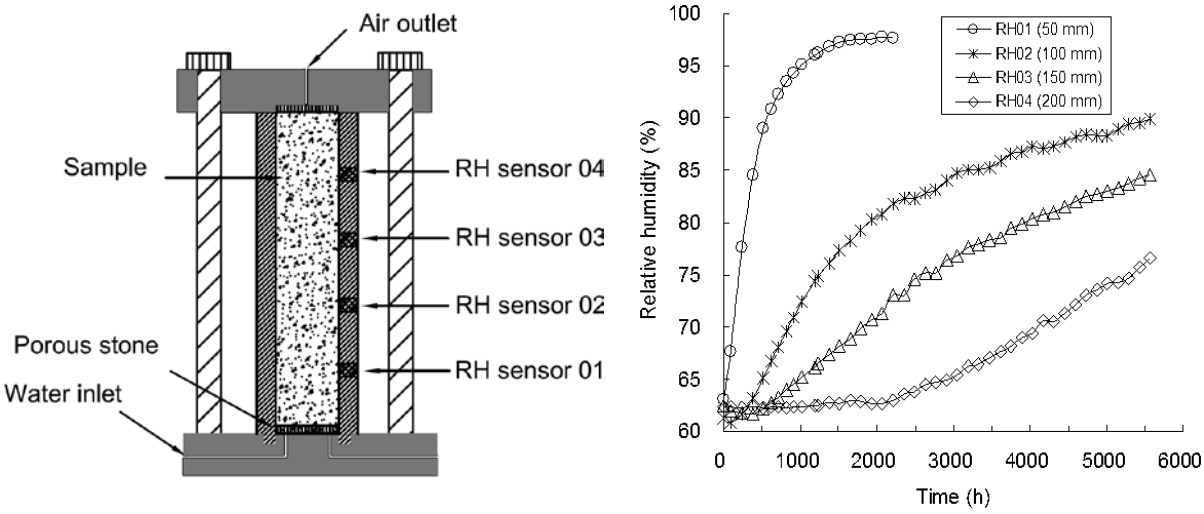

Figure 2.10. Schematic illustration of the infiltration experiment equipment used in Step 0 (left) and the observed change in relative humidity with time from (Millard and Barnichon, 2013)

2.1.4 Step 1

Step 1 considers a 1/10th scale mock-up of a SEALEX emplacement including modelling a removal of mechanical confinement (such as will be attempted for test PT-A1 – see Figure 2.7), but neglecting the hydraulic interaction with the host rock. The aim of Step 1 was to perform blind predictions of the key measurements (axial pressure and displacement) recorded during the various phases of the experiment based on the work conducted in Step 0. In addition, the modelling teams were asked to produce the variation of porosity and volumetric strains at various times and in particular at the end of the experiment for comparison with observations after dismantling the experimental setup.

The experiment consisted of a compacted sample of bentonite-sand mixture at 1.97 Mg/m^3 dry density of 120 mm height and 55.5 mm diameter placed in a rigid hydration cell of 60 mm inner diameter. The choice of the sample outer diameter versus the hydration cell inner diameter was made in order to simulate the initial 'technological' annular void which exists in the in situ SEALEX experiment between the plug and the surrounding rock-mass. However, unlike the SEALEX experiment, because the mock-up is oriented with the long-axis being vertical rather than horizontal, the annular void has a uniform thickness.

The confining piston is 60 mm in diameter and 150 mm long. At the bottom side in contact with the bentonite sample, there was a porous stone of 50 mm diameter with two water inlets (each 1 mm in diameter). A mechanical press was used to restrain the vertical displacement and a load cell was used to monitor the swelling pressure. A LVDT (linear variable differential transformer) fixed on the piston with an accuracy of 0.001 mm allowed monitoring the swelling strain as needed. The data (axial pressure and displacement) were recorded automatically to a data logger. The experimental setup is shown in Figure 2.11, together with the technological annular void.

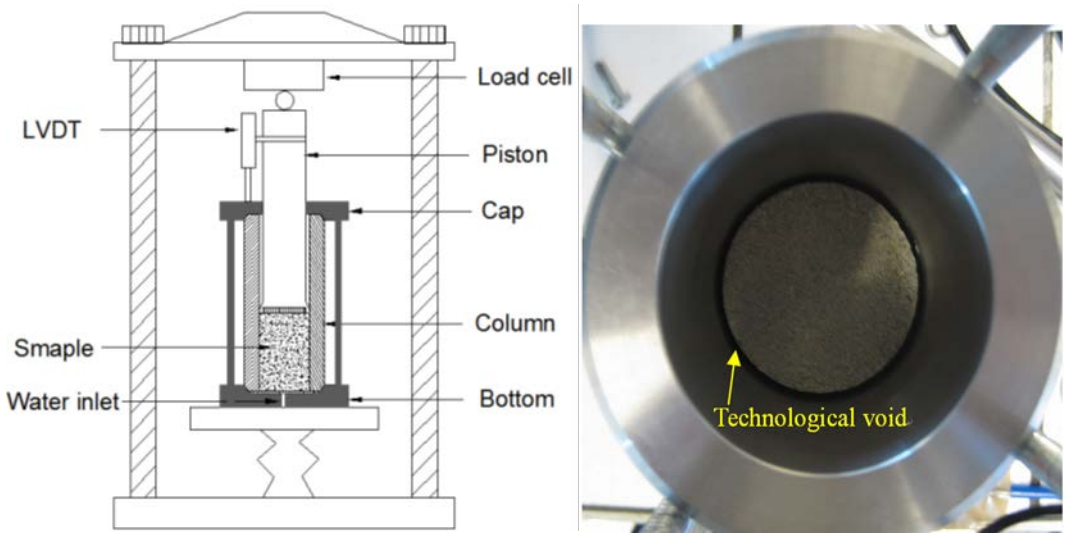

Figure 2.11. Experimental setup and detail of the technological void between sample and cell for Step 1 (from Millard and Barnichon, 2013)

The hydration was performed in three phases (as shown in Figure 2.12) simulating the evolution of the buffer material upon wetting when considering a technological void, consistent with the larger scale SEALEX experiments.

- Firstly, the vertical deformation was restrained and water was injected to the sample from the base. During this process the evolution of the vertical swelling pressure was monitored (Phase 1: initial saturation as shown in Figure 2.12).

- Once the hydration was finished, the confining pressure in the vertical direction was removed allowing the vertical free swelling. Changes in vertical strain with time were recorded (Phase 2: recovery of the vertical void). During Phase 2a only water injection from the base was permitted, but during phase 2b, water was injected from the top of the sample as well. Phase 2b started when the axial strain reached 2.8%.

- Once the vertical swelling strain reached the maximum value of 20%, the piston was again blocked and the evolution of swelling pressure was observed again (Phase 3: confinement).

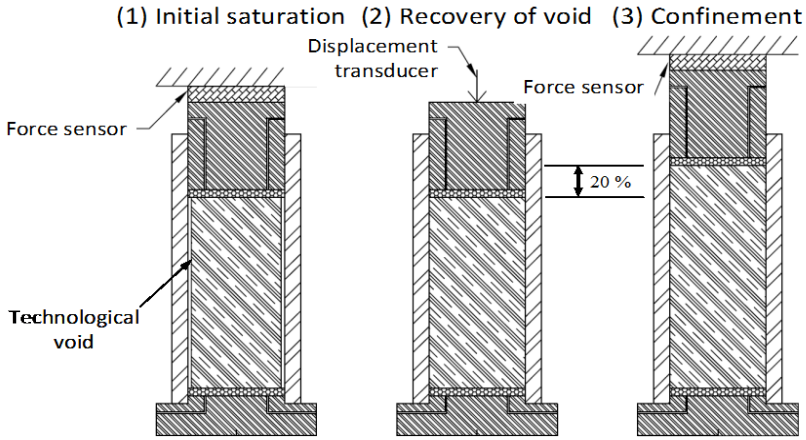

Figure 2.12. A schematic description of the three phases of the Step 1 experiment (from Millard and Barnichon, 2013)

2.2 Bentonite Overview

An important part of Steps 0 and 1 is the development of models to represent the hydro-mechanical behaviour of bentonite. Whilst there are a number of standard models that can be used, it is also useful to develop an understanding of the processes that control the interaction of water and bentonite, causing suction, swelling and stress. This understanding could contribute to the development of improved constitutive models for bentonite in the future. Before looking at the detailed work under Task A, this section provides a brief overview of the theory of bentonite structure, forces and the interaction with water. This provides some context to the experimental results and is a necessary pre-cursor to considering any possible better constitutive models for bentonite.

2.2.1 Bentonite (Montmorillonite) Structure

Bentonite is a naturally occurring clay formed from the weathering of volcanic ash deposits and principally composed of the swelling smectite mineral montmorillonite (Deer, Howie, & Zussman, 1992; Jönsson et al., 2009; Tang & Cui, 2010). In some commercial cases montmorillonite makes up 75-90% of the bentonite e.g. MX-80 (Tang & Cui, 2010). This mineral has the potential to take on water into the crystal structure thereby increasing the volume of the structure via swelling, and is responsible for giving bentonite its desirable properties for radioactive waste disposal. Fundamental to the macro-scale behaviour of bentonite is the nano-scale structural properties of montmorillonite and, as such the development of a constitutive model needs to be based on a good understanding of the processes occurring at this level (Cui et al., 2012; Gens & Alonso, 1992; Holmboe, Wold, & Jonsson, 2012; Lloret et al., 2003; Marcial et al., 2002; Pusch & Yong, 2003; Pusch et al., 1990).

Montmorillonite is a di-octahedral 2:1 smectite comprising a sheet of $Al_2(OH)_6$ between two sheets of silicate tetrahedra (Figure 2.13). The sheets are bound together by the sharing of the apical oxygen from the silicate tetrahedra with two out of three OH ions in the aluminium octahedra (Deer et al., 1992). This structure is similar to other sheet silicates such as

pyrophillite, but the key difference for montmorillonite is the isomorphic substitution of Mg^{2+} for Al^{3+} in the octahedral layer (Low, 1987). This results in the crystal lattice having a permanent negative charge, which is distributed diffusely over all the surface oxygens (MacEwan & Wilson, 1980). This charge is balanced by the adsorption of counter-ions to the surface of the montmorillonite sheet when the montmorillonite is in a dehydrated state, and as a result the diffuse negative charge becomes localised at the location of the counter-ion (MacEwan and Wilson, 1980; Low, 1987; Deer et al., 1992). Each dehydrated montmorillonite 2:1 sheet does not form a montmorillonite grain in its own right; a mineral grain is composed of a number of sheets depending on the interlayer cation charge and size (Marcial et al., 2002).

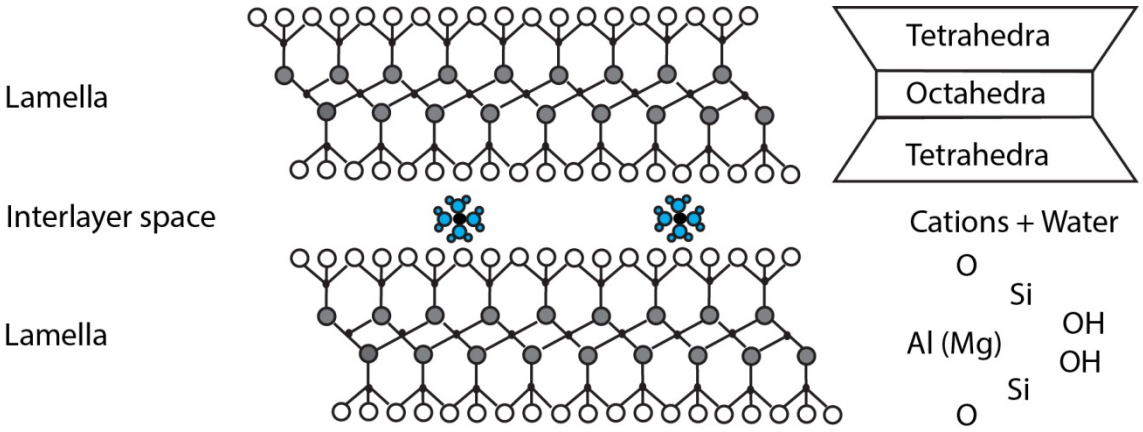

Figure 2.13: A schematic diagram of the 2:1 structure of montmorillonite sheets and the interlayer space (after Kröhn, 2003)

In radioactive waste disposal, montmorillonites that have been under the most scrutiny for practical use are ones in which the counter-ions are either Ca^{2+} or Na^{+} (Cui et al., 2002; Pusch et al., 1990; Ye et al., 2009). The greater strength of attractive forces between layers in Ca^{2+} montmorillonites results in a larger number of sheets in each stack e.g. >20-50 as opposed to *c.*5-10 in Na^{+} montmorillonites (Likos & Lu, 2006; Marcial et al., 2002; Pusch et al., 1990). The different counter-ions produce different macrostructural behaviours indicating that the chemical make-up of the mineral is an important control over the behaviour (Marcial et al., 2002). Some of the differences in behaviour have been attributed to the number of stacks that make up a montmorillonite grain (Likos & Lu, 2006; Pusch et al., 1990; Wayllace, 2008).

The presence of the counter-ions on the surface of each sheet within a stack results in a layer of micro-porosity on the nanometre scale. This porosity can be exploited by polar liquids, such as water, that hydrate the cations adsorbed to the surface (Olejnik, Posner, & Quirk, 1974). The dehydrated state of the cations produces a force that pulls water into the crystal structure and forces the montmorillonite sheets apart. Consequently, the ingress of water into the crystal structure causes a volumetric increase of the grain, i.e. swelling, and a change in porosity. This force is termed the suction pressure and is higher when the cations are dehydrated and reaches zero when the cations are fully hydrated. The structure of the water in the interlayer porosity is not entirely without dispute but it is generally considered to be well structured for sodium montmorillonites, comprising organised layers of water molecules, whereas interlayer water in calcium montmorillonites tends to form a 2D aqueous solution with the cation that is more stable (Pusch & Yong, 2006). The number of layers of

water in the interlayer can reach as many as four for Na^+ montmorillonites; two layers on each sheet (Holmboe et al., 2012; Pusch et al., 1990; Yong, 1999). The process of swelling by interlayer cation hydration is commonly termed 'crystalline swelling', although it is interchangeable in the literature with 'Type I swelling' (Low, 1980, 1987; MacEwan & Wilson, 1980), and is an important process to be able to simulate in the development of a constitutive model. Attempts to model this process include the work of Yong & Mohamed (1992) and Yong (1999) which indicated that the layers of water were held against the clay surface in the same manner as a Stern Layer, with the inner Helmholtz plane relating to the first layer of water and the outer Holmholtz plane corresponding to the second layer on each sheet (Figure 2.14). It has been shown that the layer charge and location are important factors in the swelling behaviour of montmorillonites (Sato, Watanabe, & Otsuka, 1992) and should also be a consideration in model development. Water held in the interlayer is considered to be immobile under normal hydraulic gradients (Pusch & Yong, 2006).

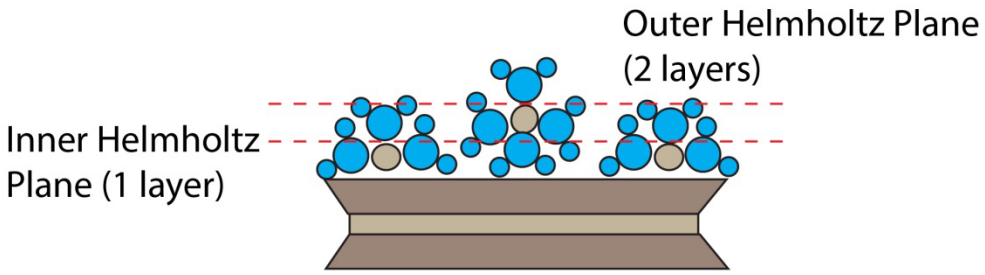

Figure 2.14: A schematic diagram showing the arrangement of interlayer water in the inner and outer Helmholtz planes corresponding to the number of layer hydrates (after Yong, 1999)

The principle of the crystalline swelling process is that the suction pressure pulling water into the interlayer overcomes the forces holding the layers together. At higher suctions the interlayer sites are dehydrated and subsequently pull the water in. However, the low water content indicates that the distance between the interlayers is small and so the attractive forces holding the layers together is *almost* as strong. At lower suctions the need for the interlayer sites to be hydrated is reduced. This is due to more water hydrating the cations between the layers, which produces larger distance between the layers. Consequently, as the suction reduces so do the attractive forces holding the layers together.

However, crystalline swelling is not able to describe all the observable behaviour for sodium montmorillonites. At low suction pressures i.e. when the interlayer cations are fully saturated by multiple layers of water molecules, sodium montmorillonites exhibit large increases in volumetric swelling if allowed to swell freely. This leads to a bi-linear shape to water retention curves (Marcial et al., 2002). This process cannot be accounted for by the alleviation of suction pressure alone and has been described by the Diffuse Double Layer (DDL) theory as proposed by Bolt (1956) and discussed by MacEwan and Wilson (1980), Low (1987), Zhang et al. (1995), Komine and Ogata (1996), and Komine and Ogata (2003) among many others. It has been shown that the process of swelling at basal spacings greater than 35Å is driven by osmotic forces and, consequently, is often termed 'osmotic swelling', but is also known as 'Type II swelling'. At interlayer distances <35Å and at very high concentrations of montmorillonite the DDL theory is not applicable, but this domain is covered by the swelling due to hydration of interlayer cations (Komine & Ogata, 1996;

Marcial et al., 2002; Villar, Gómez-Espina, & Gutiérrez-Nebot, 2012). This process is most common in Na^+ montmorillonites as the forces between sheets are weaker and the number of sheets in a stack is fewer (Likos & Lu, 2006). As the driving forces are osmotic, this process is heavily dependent on the concentration of ions in the pore water fluid.

In order for the DECOVALEX-2015 experiments to be sufficiently modelled both Type I and Type II swelling mechanisms must be sufficiently modelled. Modelling the hydromechanical behaviour of bentonite using the Barcelona Models has commonly implemented DDL theory as the basis for the microstructure model (Gens and Alonso, 1992; Lloret et al., 2003; Sánchez et al., 2005), whilst other authors have also used DDL theory to predict swelling pressures (Komine & Ogata, 1996, 2003). A non-linear elastic approach, similar to that suggested in this report, has been implemented by Cui et al. (2002) to reproduce the behaviour of Ca^{2+} bentonites, which show a large degree of reversibility. A state-surface poro-elastic approach has also been proposed to tackle the problem of volume change (Nguyen, Selvadurai, & Armand, 2005).

2.2.2 Forces and Bonds in Bentonite

The forces present in bentonite have been briefly touched on in the preceding section and can be divided into four main groups; suction, osmotic, attractive forces, and confining stresses. The suction pressure is the driving force of hydration causing crystalline swelling; osmotic forces are the driving force of osmotic swelling; the attractive forces are those acting between individual sheets and particles that counteract swelling; and confining stresses are both the confinement caused by surrounding particles and also the stress conditions of the sample as a whole e.g. in a oedometer or cell.

Sheets of montmorillonite are held together by bonds between the interlayer cation and tetrahedral oxygens, and hydrogen bonds between the hydrating water molecules, cations, and tetrahedral oxygens (Pusch & Yong, 2006). Montmorillonite particles are held together by primary valence, hydrogen, van der Waals, and electrostatic bonds (Pusch et al., 1990). Hydrogen bonds are weak- typically between 1-3 kCal/mol but large numbers can lead to a significant attractive force (Pusch & Yong, 2006). The strength of these bonds holding the sheets and particles together counteracts the expansion force produced by the alleviation of suction pressure.

2.2.3 Key Aspects

The major point to be taken from this brief description of the bentonite structure is that, unlike the assumptions in much porous medium theory, the water strongly interacts with the mineral structure, such that the conventional conceptual model of water only inhabiting some fraction the porosity (fraction of volume not filled by mineral grains) is clearly not an accurate description of the system. The unusual and desirable features of bentonite; the high swelling potential; plasticity; and low intrinsic permeability appear to be strongly related to this complex internal structure. It therefore follows that any constitutive model should take such complexity into account either through modification to existing soil or porous medium theory or through new process models.

2.3 Approach to Task A

The primary challenge to the successful involvement in Task A is to be able to generate an appropriate constitutive model to represent the hydro-mechanical evolution of a bentonite sand mixture. As discussed in the previous section, bentonite expresses a range of behaviour that is related to, but not necessarily well represented by conventional soil mechanics and hydraulic flow porous media. This is mainly because of the extreme swelling under hydration caused by the very high mass fraction of montmorillonite, one of the major features of bentonite that makes it desirable for use as a buffer or seal in geological disposal facilities for radioactive waste. The high degree of interaction between the solids and fluid phases in bentonite means that under certain conditions, bentonite does not behave as a conventional porous medium, and is considerably more complex.

While specialist models of bentonite do exist (e.g. the Barcelona Basic Model; Gens & Alonso, 1992; and as modified e.g. Sánchez et al., 2005), they are complex to implement, test and parameterise and require a great deal of supporting experimental data to be used effectively for predictions (also see Section 2.6.1). Given the overall desire to keep process models as simple as possible, but also to explore alternative models than those in the literature, we approached this Task using two distinct tracks:

- Use of relatively simple pre-existing hydro-mechanical process models wherever possible (e.g. standard Darcy groundwater flow for one or more fluid phases, linear elasticity), and extension of those process models using 'standard' literature approaches as required. This approach provides understanding on how much sophistication in the process models is required in order to replicate the experimental observations. This is discussed in Section 2.4 and 2.5.

- Development of novel or complementary process models, building on 'standard' approaches where practicable. The primary aim of such models is to attempt to tie in parameterisation more closely to readily measurable characteristics of the bentonite-water-air system with less recourse to the very empirical, and sometimes arbitrary parameterisation seen in the more complex bentonite hydro-mechanical models. This is where the understanding of fundamental bentonite behaviour developed in Section 2.2 potentially becomes important. This work is discussed in Section 2.6.

The latter of the two approaches will be the main focus of the work conducted by the PhD student at the University of Edinburgh. By following these two lines in parallel it was expected that full and rapid participation in the Task could be achieved, while at the same time, attempting to create alternative, and simpler models of bentonite that have good predictive power. Also, by running these lines of work together, the opportunity arises for cross-comparison of the approaches and hence confidence building in any novel models that are developed.

2.4 Step 0

2.4.1 Water Retention Curve

The experimental data made available provide both a free swell (unconstrained) suction profile with water content and a constant volume profile (Figure 2.8, Table 2.1), capturing the suction for two end-member mechanical conditions. Any numerical model that deals with partially confined bentonite, as is the case for the SEALEX experiment, requires a means to calculate where between the two suction curves a given volume of bentonite rests, given the physical conditions of the bentonite and the strain history.

Table 2.1: Water retention curve data as supplied in Millard and Barnichon (2013).

Free swell		Constant volume	
Suction (MPa)	**Water content (%)**	**Suction (MPa)**	**Water content (%)**
0.01	246	0.01	25.42
0.1	94.33	0.1	24.86
1	28.5	1	24.63
4.2	21.72	4.2	18.6
9	17.6	9	17.59
24.9	14.7	12.6	15.61
36	13.51	24.9	14.3
82	11.1	36	13.06
113	8.6	65	10.88
309	2.3		

Before considering a suitable approach some simple observations need to be made about the data. The water retention curve under constant volume conditions shows an increase in water content from 10.88 wt% at 65 MPa suction to 25.42 wt% at 0.01 MPa suction. This corresponds to 4.17E-6 m^3 of water injected into the sample, assuming water density of 1000 kg/m^3. The initial pore volume of the sample was 3.82E-6 m^3 which shows that the volume of water injected is almost 10% greater than that predicted by the initial pore volume. This suggests that either the bentonite 'solids' are being compacted under load or the density of water when included in the crystalline structure of the bentonite interlayers is actually at a higher density (e.g. Jacinto et al., 2012). In any case, this simple analysis shows that naïve use of concepts such as water saturation and porosity may cause significant errors in terms of estimates of water uptake by bentonite-rich materials.

Secondly, the free suction curve does not show it tending to zero suction for a given water content; there remains a finite suction even at 250% water content by mass. This is an effect of the swelling of the bentonite increasing net volume, and the tendency of the bentonite to form a gel with the water at very high water contents. Essentially, because of the chemical interaction of the water and the bentonite, there is always a finite suction even when water becomes the dominant phase. Again this illustrates that the conventional porous media model used for soils may be difficult to apply for bentonites at high water contents.

From the literature there are two general approaches to moving between these two curves. The first by Croney et al. (1958) and used by Duerk (2005), takes the free swell curve for the current water content and subtracts the current average confining pressure to arrive at the effective suction for the current conditions. The second approach is that of Gens & Alonso (1992) where the constant volume retention curve is used for all circumstances, but is parameterised in terms of water saturation, rather than water content. If a sample is not fully confined the increase in volume keeps the water saturation lower than in the fully confined case, hence giving a higher water content for the given suction.

The advantage of the first method is that it more closely ties stress and suction together, however the method no-longer uses porosity to represent the total water capacity of the bentonite. Hence at higher water contents the method can imply water saturations that are greater than 1, without further corrections to the notional 'porosity' of the sample (although this is observed experimentally, as noted above). This makes using this approach with conventional multi-phase flow simulators problematic under certain circumstances. Also, because of the approximately log-linear relationship between free suction and water content, small variations in the suction model can give rise to large variations in water content for a given suction. In contrast the second approach is fully compatible with conventional soil mechanics theory and hence is easier to model, but is possibly less thermodynamically self-consistent and may not always reproduce the free swell curve unless the swelling characteristics under unconfined conditions are carefully parameterised, however it is the standard approach for the BBM and BExM.

As a starting point for fully coupled hydro-mechanical models, it was decided to adopt the Duerk (2005) model as it has been used successfully in modelling the Canister Retrieval Test (Bond et al., 2009). Therefore a functional form was developed for the observed free-swell water retention curve using a form often seen in the literature and used in other experiments:

$$\varphi_f = F(\exp(a - bW) + \exp(c - dW)) * 1 \text{ [MPa]} \quad (1)$$

Where φ_f is the free suction (MPa), F is the mass fraction of bentonite (kg/kg), W is the water content by mass (mass of water per mass of solids - kg/kg) and a-d are fitting parameters (all dimensionless) with the following values.

a=7.15, b=24, c=-0.5, d=1.5 (2)

Following the method described by Duerk (2005), the confined swell pressure (φ_c) is therefore derived as follows where p is the mean confining stress.

$$\varphi_c = \varphi_f - p \quad (3)$$

A confined swelling pressure of 3 MPa is assumed from data published by Wang et al. (2012, Figure 2.15), which for the plots below is assumed to increase linearly with change in water content from zero MPa at the initial water content. In fully-coupled cases this will not necessarily be the actual evolution, but it is a sensible first-order approximation. It should be noted that this is not a general model for suction in bentonite, but by necessity, very much an empirical calibration against this particular bentonite starting at a dry density of 1.67 Mg/m^3 and an initial water content of 11%.

The resultant curves are shown in Figure 2.16 and Figure 2.17. The fit is reasonable, but the data show a considerable quantity of variation from a smooth functional form, and as such the derived curves are somewhat idealised.

For fully- or closely- confined cases a simple lookup function of the confined curve can be used in preference to the above model because it reduces the complexity of the analysis. Consideration of the saturation-based model will be considered as a variant approach later in the project.

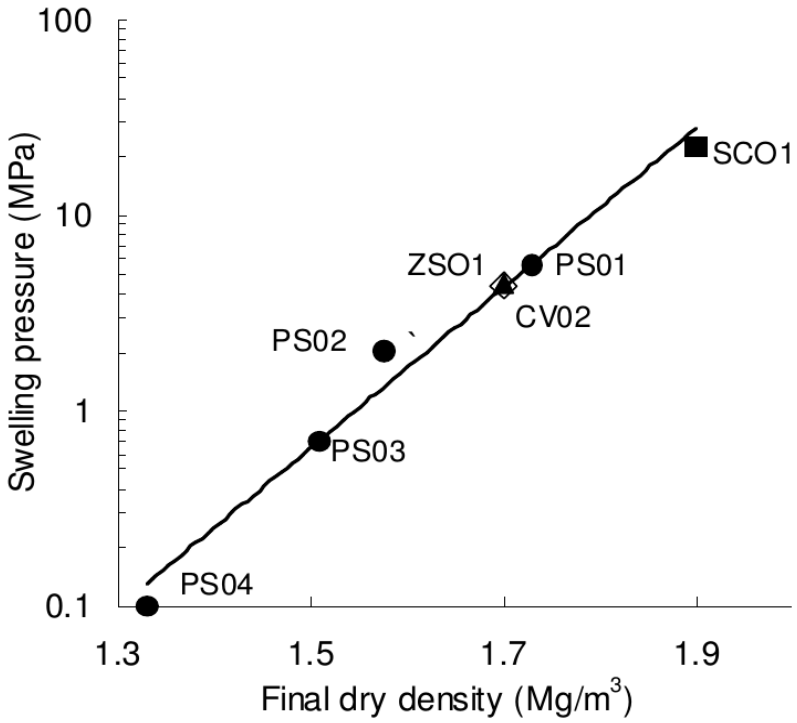

Figure 2.15 Confined swelling pressure versus dry density from Wang et al. (2012)

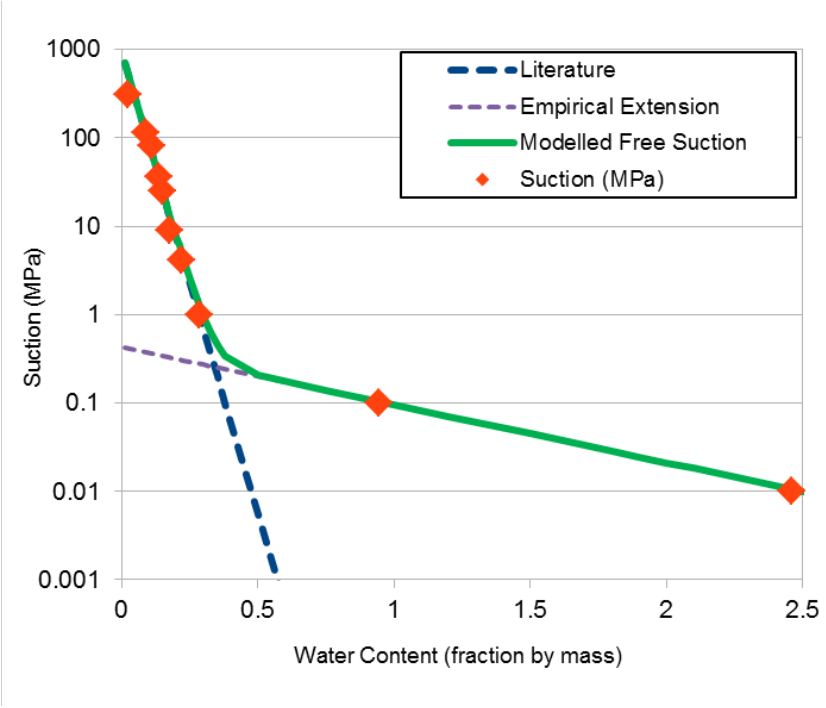

Figure 2.16 Proposed free suction curve

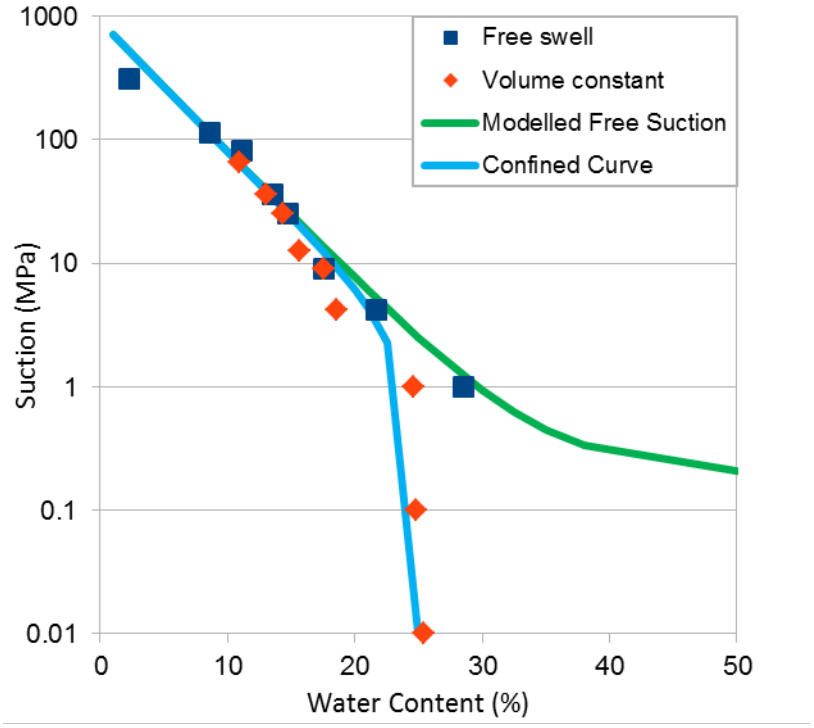

Figure 2.17 Proposed confined suction curve using the confining stress to cause the deviation from the free to confined curve (after Duerk, 2005)

2.4.2 Oedometer Tests

In analysing the oedometer tests, two forms of analysis were conducted. The first used the basic approach which underpins the BBM and BExM, the Cam-Clay model. This is a standard approach for representing elastic-plastic deformation in soils and has been very widely applied, especially for understanding oedometer tests; however this is just one of a family of empirical models (Section 2.5). The second approach considered a non-linear elastic model, attempting to take a more physical view of the bentonite/sand microstructure – this is discussed in Section 2.6 in the context of a new bentonite model.

The Cam-Clay model is a moderately complex model for the development of elastic (recoverable) and plastic (non-recoverable) deformation in soils. It works on the principle of a yield surface which is a function of the current stress state and the plastic deformation history of the sample. If the yield surface is encountered when the sample is under constant load, then the soil will undergo plastic deformation such that the soil returns to a condition of stability, i.e. the condition is no-longer within the yield surface. The elastic and plastic deformation that occurs is typically assumed to be taken up by porosity, hence the change in total strain can be linked directly to the void ratio.

The full description of the model is quite lengthy (a good discussion can be found in Schofield, 2006), however the salient points for this discussion are:

1. The elastic modulus of the sample increases with average stress, i.e. the sample becomes elastically stiffer with applied load.

2. When the sample deforms plastically the yield surface increases in size such that the stress required to cause further deformation goes up with the volumetric plastic strain raised to some power (i.e. compaction appears linear on a linear:log plot of strain (or void ratio) versus applied stress. This size of the yield surface is described as the 'preconsolidation pressure', p_c.

3. Elastic loading and unloading shows little or no hysteresis (i.e. purely elastic loading and unloading cycles follow the same stress, strain pathway).

This form of deformation is illustrated in Figure 2.18, showing the onset of plastic deformation with increasing load. The model is typically characterised by four parameters:

- p_{c0}: Virgin (reference) preconsolidation pressure (MPa)
- M: Gradient of the critical state line (dimensionless)
- K: Swell/Compression index (elastic)
- λ: Consolidation index (plastic)

and two definitions of stress:

- p: mean stress (MPa)
- q: deviatoric stress (MPa)

where

$$p = \frac{1}{3}\left(tr(\boldsymbol{\sigma})\right) \tag{4}$$

$$q = \frac{3}{2}\sqrt{\|\xi\|},\ \xi = \boldsymbol{\sigma} - p \tag{5}$$

noting that $\boldsymbol{\sigma}$ is the Cauchy stress tensor (Howell et al. 2009) and tr() is the trace function (sum of the diagonal entries of a tensor). The compression/swell index is normally expressed in terms of the Young's Modulus (E [MPa]) and Poisson's Ratio (ν), with the Young's Modulus increasing with increased applied stress so the clay becomes stiffer under increasing load. The exact form of the relationship depends on the implementation of the elastic model in the code performing the analysis.

The Modified Cam-Clay (MCC) model is adapted from the original to make the model more amenable to numerical solution and the yield surface is described by the following relationship:

$$f = \left(\frac{q}{M}\right)^2 + p(p - p_c) \leq 0 \tag{6}$$

Unlike the standard Cam-Clay model, but consistent with the typical BBM approach, swelling is handled through an incremental additional volumetric strain term (ε_s) which itself is a function of water content and stress state (a relationship that is derived empirically for different densities of bentonite and mineralogical content). To avoid 'double-counting' of expansion due to swelling, the classical effective stress term is modified so that

$$\sigma'_{ii} = \sigma_{ii} - \max\left(P_a, P_w\right) \tag{7}$$

Where σ_{ii} is a diagonal entry on the total stress tensor (MPa), P_a is the pressure of air (MPa) and P_w is the water pressure.

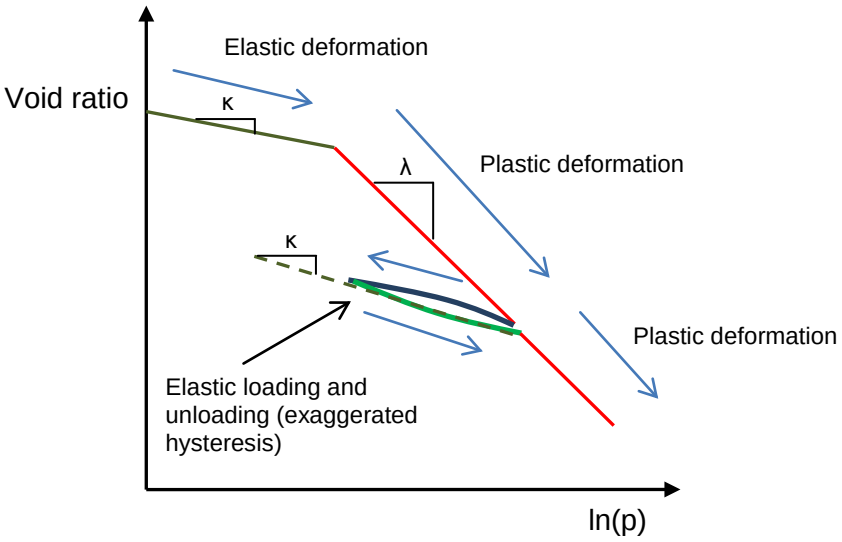

Figure 2.18 Stylised oedometer test showing the typical cam-clay model representation of compaction. Blue arrows show the evolution, from the starting condition.

The MCC model was implemented as a QPAC user model to interface with the QPAC mechanical module (Bond, 2013a), and the model calibrated against the experimental data. Due to the lack of radial stress data from the oedometer experiments, it was found that wide range of MCC parameterisation could be made to fit the experimental data acceptably, depending on the assumptions made on the degree of radial compaction under swelling, Poisson's ratio and the M and λ MCC parameters. Radial stress values could be estimated, however it is necessary to know both the magnitude of plastic strain in the radial direction as well as the Poisson's Ratio. The lateral plastic strain is not known experimentally and can only be estimated from the MCC model evolution itself. Therefore any radial stress estimates are not independent and hence do not significantly constrain the models.

Also, consistent with the BBM and BExM, in order to get very good fits versus the experimental data it was necessary to decrease the reference preconsolidation pressure as suction decreased and at the same time slightly increase the consolidation index. The exception was for the zero suction test where it was clear that the majority of compaction was actually elastic, deviating from the trend shown by the other samples and the expected results from other bentonite models such as the BBM. The reason for this was unclear, whether it is an experimental artefact, or a function of the much higher starting dry density of 1.97 Mg/m^3 (noting that the zero suction experiment contained a radial void to allow it to expand radially as well as vertically to take it down to approximately 1.67 Mg/m^3 dry density). Furthermore the elasticity shown by the zero suction case suggests a lower elastic modulus than the other samples.

The first attempt at calibration attempted to get a good fit across all four tests with minimum variation in parameters between them. While this model fitted the oedometer data well it has an unfortunate side-effect of making the evolution of stress when wetted under fully confined conditions non-monotonic and increase significantly (and to a very high swell pressure, much more than predicted in Figure 2.15) at low suctions. The conclusion was that the zero

suction case was distorting the behaviour, hence two further models were produced, one which was calibrated against the three higher suction tests (low density model - Figure 2.19), and another that was calibrated well against the zero suction experiment (high density model - Figure 2.20). The form of the two models are extremely similar, however there are differences in the reference pre-consolidation pressure, elastic modulus function and the swelling model (Table 2.2).

Both models perform sensibly under fully-confined conditions when wetted to zero suction, although the maximum swell pressure of the high density model is higher than predicted by Wang et al. (2012) at approximately 5.8 MPa, rather than 3 MPa. The reason for this higher stress is that in order to match the early swelling behaviour better, the water retention curve was shifted from the reference parameterisation by 0.03 water content units, such that a given water content gives a higher suction (Table 2.2). The change is not large and is justified on the basis that no direct suction data on the higher density material were provided and that higher density bentonites tend to show higher suctions at a given water content (e.g. Duerk, 2005), and is certainly within the bounds of error of the data presented in the literature (e.g. Wang et al. 2012). Clearly this variation in saturated swelling stress may impact on the accuracy of predictions for Step 1.

These models, while not perfect, and containing considerable uncertainties, were felt to be sufficient for Step 0. Given the intention of the Task structure is to understand the level of data required to make successful blind predictions, it was decided that these models were also appropriate for use in Step 1. However it is likely that these Step 0 and Step 1 bentonite models would need to be improved and extended with additional data and more sophisticated functional forms in preparation for the later Steps.

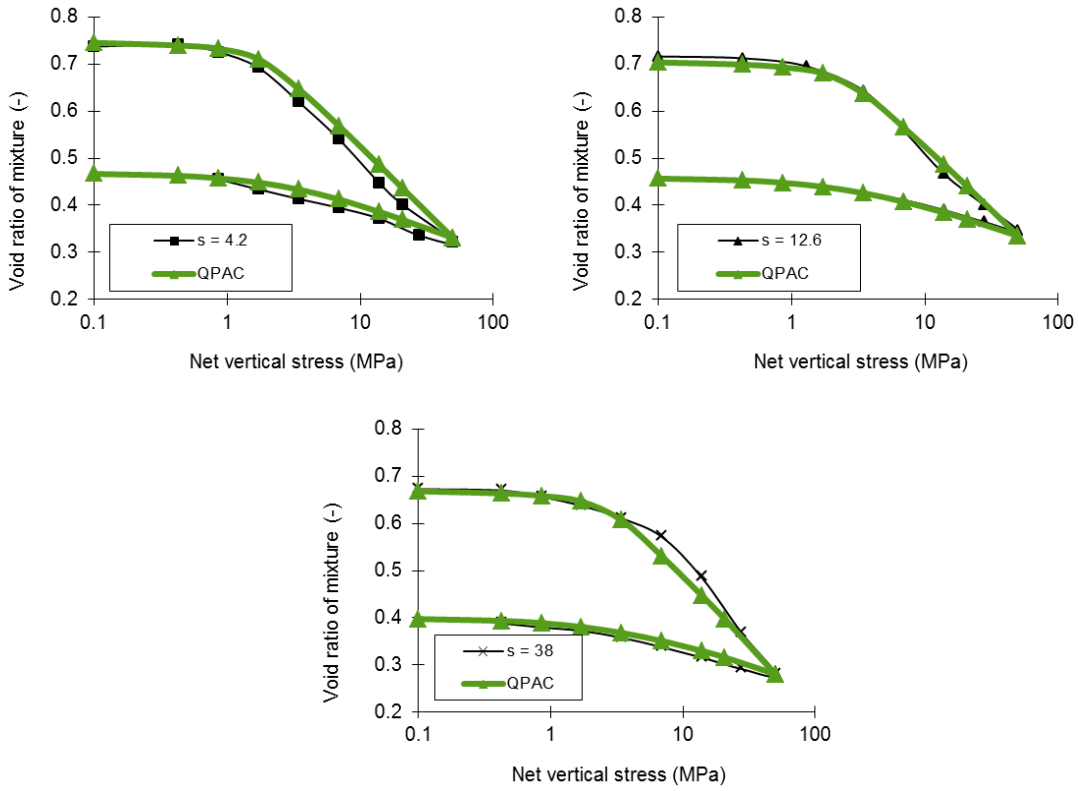

Figure 2.19. Calibration against the experimental data using the 'low density' model. Suctions (s) are in MPa.

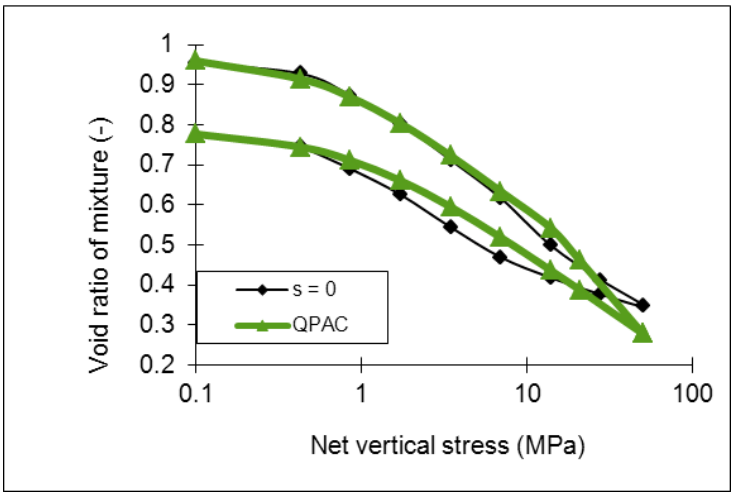

Figure 2.20. Calibration against the zero suction data using the 'high density' model

Table 2.2. Parameterisation for the 'low density' and 'high density' MCC model (see previous section for a discussion on the parameters and their meaning)

Parameter	Value/Function (low density model)	Value/Function (high density model)	Comments
E_0	0.075 GPa	0.1 GPa	Reference Young's Modulus
E	E_0 + p (850/38)	E_0 + p (350/38)	Fitted
p_{c0}	1.5 [MPa] * *PScaleFactor*	15 [MPa] * *PScaleFactor*	Fitted
PScaleFactor(φ_c)	0 [MPa] -> 0.4 [-] 4.2 [MPa] -> 0.6 [-] 12.6 [MPa] -> 1.0 [-] 38 [MPa] -> 1.2 [-]	0 [MPa] -> 0.4 [-] 4.2 [MPa] -> 0.6 [-] 12.6 [MPa] -> 1.0 [-] 38 [MPa] -> 1.2 [-]	Fitted, linear interpolation with suction (φ_c)
M	1.5 * *MScaleFactor*	1.35 * *MScaleFactor*	Fitted
MScaleFactor(φ_c)	0 [MPa] -> 1.0 [-] 4.2 [MPa] -> 1.0 [-] 12.6 [MPa] -> 1.0 [-] 38 [MPa] -> 1.0 [-]	0 [MPa] -> 1.0 [-] 4.2 [MPa] -> 1.0 [-] 12.6 [MPa] -> 1.0 [-] 38 [MPa] -> 1.0 [-]	Note no change with suction (φ_c)
λ	25**CIScaleFactor*	25**CIScaleFactor*	
CIScaleFactor(φ_c)	0 [MPa] -> 1.1 [-] 4.2 [MPa] -> 1.1 [-] 12.6 [MPa] -> 1.0 [-] 38 [MPa] -> 0.85 [-]	0 [MPa] -> 1.1 [-] 4.2 [MPa] -> 1.1 [-] 12.6 [MPa] -> 1.0 [-] 38 [MPa] -> 0.85 [-]	Fitted, linear interpolation with suction (φ_c)
ε_s – Swell Strain	$(W - W_0)*(\rho_d/\rho_w)*D$	$(W - W_0)*(\rho_d/\rho_w)*D$	W = water content W_0 = initial water content ρ_d = dry density ρ_w = water density
$D(\varphi_c)$	0 [MPa] -> 0.35 [-] 4.2 [MPa] -> 0.40 [-] 12.6 [MPa] -> 0.55 [-] 38 [MPa] -> 0.9 [-]	0 [MPa] -> 0.9 [-] 4.2 [MPa] -> 0.9 [-] 12.6 [MPa] -> 0.9 [-] 38 [MPa] -> 0.9 [-]	Increased for high-density model to account for radial swelling. Fitted, linear interpolation
φ_c Suction Pressure	As per Section 2.4.1	As per Section 2.4.1, but offset by +0.03 water content units	Offset of water retention curve justified by various published data (e.g. Duerk, 2005); Börgesson, 2007

2.4.3 Infiltration Test

The overall objective in the infiltration test was to try and obtain a calibration using standard process models that reflected the general resaturation timescale of the sample and the form of the transient resaturation up the sample. It was expected that hydraulic-only models would likely be inadequate to give a good general representation of the system and there was an expectation that some link to the mechanical processes or further non-linearity in the hydraulic process model would be required.

2.4.3.1 Reconnaissance Model

In order to investigate the degree of hydro-mechanical coupling required to replicate the infiltration test, an initial piece of work was conducted using OpenGeoSys to attempt a calibration using typical relative permeability curves. The model used Richard's equation for the water flows which for a unit volume can be expressed:

$$\mathbf{q} = -\frac{\mathbf{k}}{\mu_w}.k_r(\nabla P_w + \rho_w \mathbf{g}) \tag{8}$$

$$\frac{\partial(\theta S \rho_w)}{\partial t} + \nabla \cdot (\rho_w \mathbf{q}) - \rho_w Q_w = 0 \tag{9}$$

Where $\mathbf{k}$ is the intrinsic permeability tensor (m^2), k_r is the relative permeability for water, P_w is the water pressure (MPa), ρ_w is the density of water (kg/m^3), μ_w is the viscosity of water (Pa s), $\mathbf{g}$ is the gravity vector (m/s^2), Q_w is an external source of water for the unit volume (s^{-1}), θ is the porosity (-), $\mathbf{q}$ is the flow velocity (m/s) across a unit area and *S* is the saturation (-).

This formulation assumes water is the active phase and air is essentially passive and at a constant pressure. A 1D geometry was used with twenty equal-sized linear 1D elements in the vertical direction. The confined water retention curve was used as a simple lookup function to define the suction with water saturation.

Calibration attempts were unsuccessful in producing a model that gives a good match across all four sensors using standard functional forms for relative permeability. In order to assist the future modelling, rather than using typical curves, completely arbitrary curves were used, including components that could vary in time and location, as well as by water saturation. The intent of such an exercise was to reveal where and when the likely mechanical coupling would have to occur and hence what coupling processes might be required in the full hydro-mechanical model, rather than producing a physical model. For example, there might be more of a spatial or temporal control on the adjustments, which might imply porosity rather than stress being the dominant influence on the permeability changes.

For this non-physical model the relative permeability model took the form of

$$k_r = f1(S_w).f2(t).f3(S_w) \tag{10}$$

where S_w is the water saturation and t is the elapsed time since water injection started. The resulting fit and relative permeability scaling factors are shown in Figure 2.21 and Figure 2.22. The intrinsic permeability for modelling was set at 1.8e-19 m^2, although as the highest

combined curve value was 0.1, this equates to an initial value of 1.8e-20 m^2 for a normalised relative permeability curve

While the model results and data do not fit precisely, it illustrates a need to reduce net permeability with time as the bentonite swells and compresses internally in order to obtain a better representation of hydration of the specimen. The missing element in the hydraulic only model appears to be sufficient enhancement of permeability at the early times. All of these elements point to a requirement to have intrinsic permeability as a strong function of change in local volume (and hence porosity if the dry solids are assumed to be of constant volume), noting that the net volume of the sample remains constant.

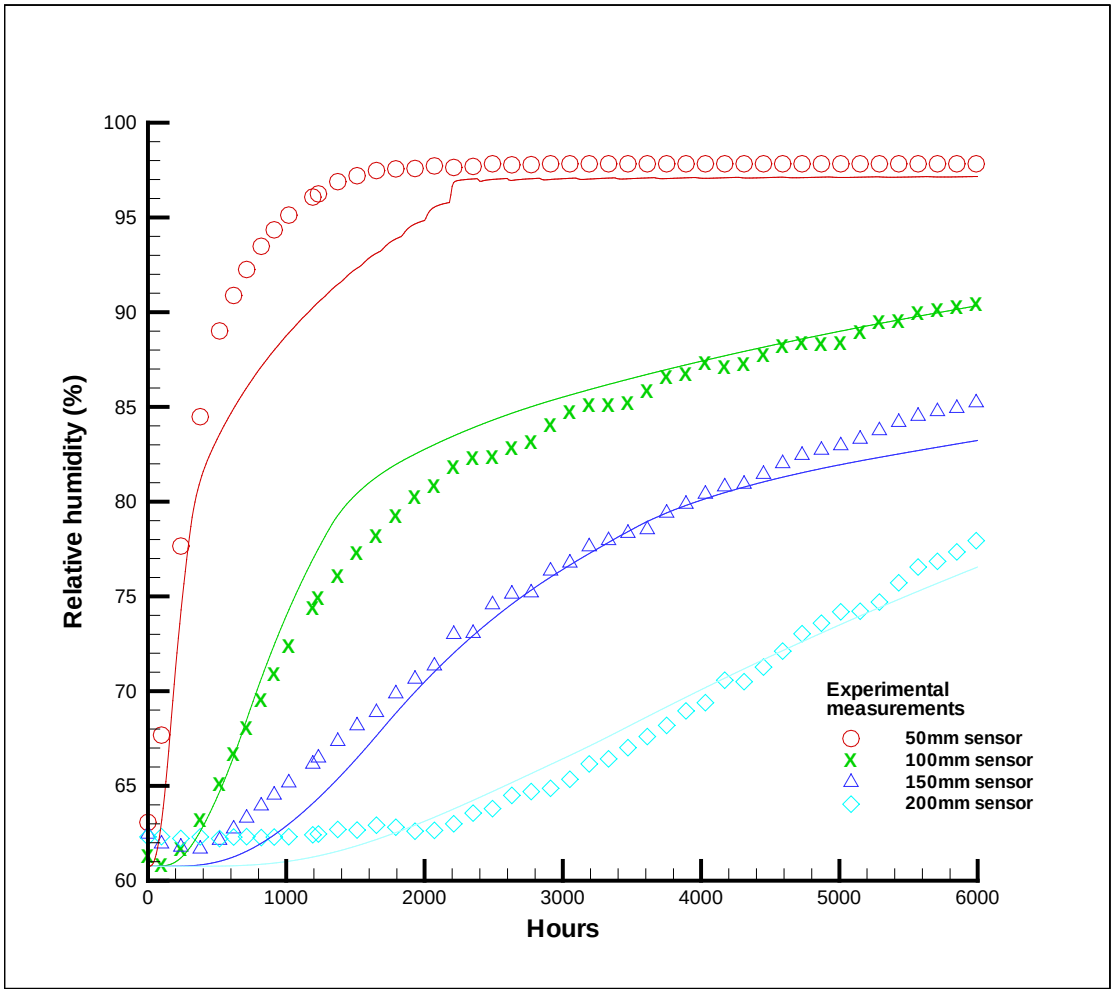

Figure 2.21. Fit for the OpenGeoSys infiltration model using the non-typical relative permeability functions.

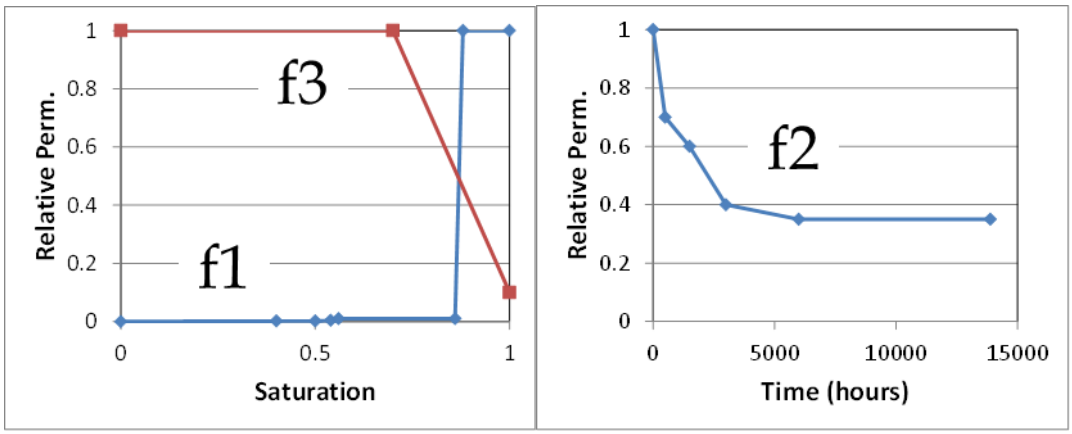

Figure 2.22. Components of the non-typical relative permeability functions (to compare with equation 10)

2.4.3.2 Coupled HM Infiltration Model

A modified QPAC infiltration model was created using the multi-phase flow (MPF) module, which considers Darcy flow for water and an arbitrary number of non-water phases, in this case only air was considered as a gas (Bond and Benbow, 2009). The discretisation and model domain are shown in Figure 2.23.

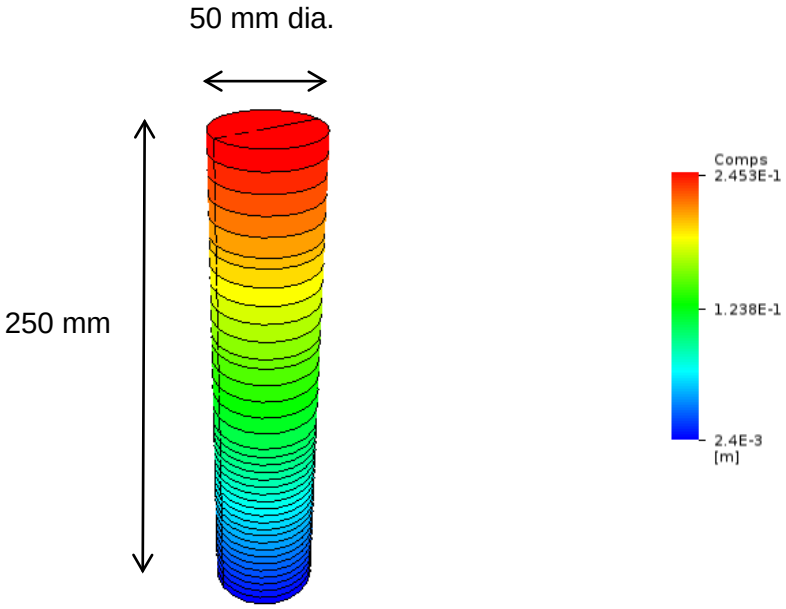

Figure 2.23 Grid for the QPAC infiltration calculations, coloured by elevation (m)

The bottom boundary is fully water saturated with a water pressure of 1 atmosphere while the top boundary is assumed to be fully gas saturated with a gas pressure of 1 atmosphere, however no water is permitted to leave through the top surface, reflecting the experimental setup. Early versions of the model were constructed using hydraulic-only processes to

compare back to the OpenGeoSys reconnaissance models and were found to give very similar results.

Consistent with reconnaissance models, using hydraulic-only processes and conventional relative permeability curves it was found to be extremely difficult to match all four sensors equally well. Fits to the top and to a certain extent the bottom sensor could be achieved by using a high intrinsic permeability of the order of 1e-19 m^2 and a very sharp relative permeability curve ($k_r = {S_w}^6$), but the fits to the middle two sensors were very poor (k_r is the relative permeability of water and S_w is the saturation of water. The relative permeability of air was assumed to be one at all times to be as consistent as possible with the reconnaissance models). The calibration for this case is shown in Figure 2.24.

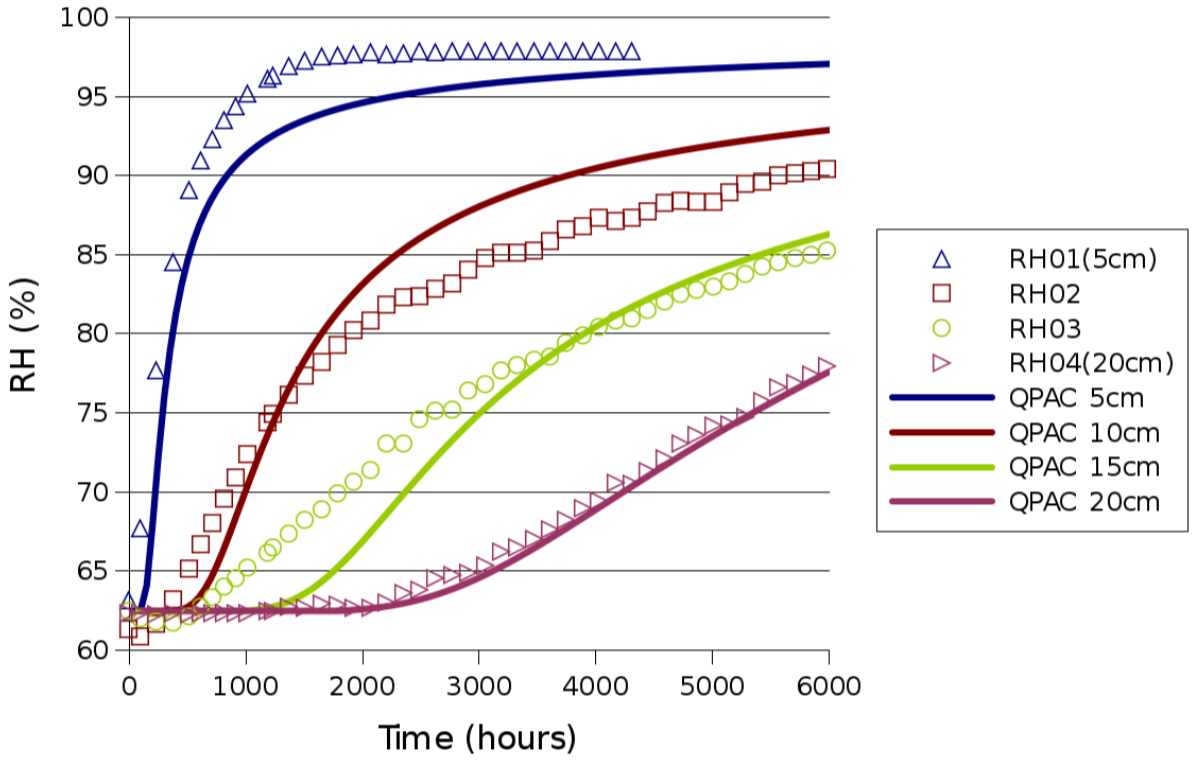

Figure 2.24. A reasonable calibration for a hydraulic-only model using high intrinsic permeabilities and sharp relative permeability curves.

Some consideration was given to the work of Sánchez et al. (2007) which examined the impact of water flows through saturated FEBEX bentonite at a variety of head gradients. It was established that at higher compaction densities, head gradients of the order of 1000 (m/m) were required in order to provoke water flow, a so-called 'threshold gradient phenomenon' (Figure 2.25).

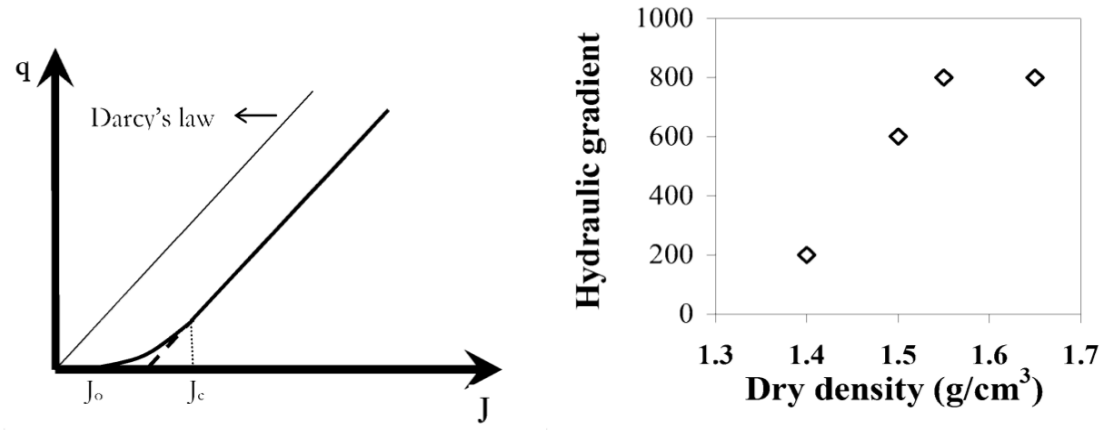

Figure 2.25 (left) Threshold gradient phenomenon (q= Darcy flow, J= hydraulic gradient). (right) Minimum hydraulic needed to get measurable flows as a function of the dry density of the FEBEX bentonite (from Sánchez et al. 2007)

At low gradients this effectively prevents water movement, perhaps indicative of the types of behaviour seen in the Canister Retrieval Test (Börgesson, 2007) and other large-scale bentonite resaturation experiments, while at higher gradients the impact is simply a reduction in the flow rate for a given gradient.

A simple representation of the model was implemented and tested in QPAC using the following scaling factor applied to all water flows

$$ND = \begin{cases} 0 & J < J_T \\ 1 - \frac{J_T}{J} & J \geq J_T \end{cases} \quad (11)$$

Where *ND* is the non-Darcy scaling factor, *J* is the hydraulic gradient (m/m) and J_T is the threshold gradient for flow to occur.

There were no suitable data for such threshold behaviour in MX-80/Sand mixtures so a threshold of 1500 (m/m) was assumed for the bentonite used in the infiltration test, noting the MX-80 is known to have a lower permeability than FEBEX. Implementing such a model using the early versions of the QPAC model without mechanical coupling produced a small change in behaviour away from the calibration shown, which was easily corrected by increasing the intrinsic permeability by a factor of 1.25.

The result is perhaps not surprising given the large hydraulic gradients caused by the large suctions in the model, but such a process could be important over longer timescales and larger samples, especially if the threshold gradient is higher.

For the Step 1, the non-Darcy model was retained because of its present low impact in the infiltration test but potential for significance in other models. Future work during later Steps should attempt to characterise and understand the potential impact of such a process in more detail, ideally supported by more data.

The low density oedometer model was used directly and fully-coupled to the modified MPF model. Because the swelling is significant, especially in the lower parts of the model, the

output was changed such that relative humidities were linearly interpolated between compartments at the key measurement points rather than reporting from a compartment at the appropriate height at the start of the simulation.

A calibration was sought to the data and this was achieved using the following parameterisation:

$$k = k_0 \left(1 + 10 \frac{(\theta - \theta_0)}{\theta_0}\right) \quad (12)$$

$$k_0 = 6.5x10^{-21}\, m^2 \quad (13)$$

$$k_r = {S_w}^4 \quad (14)$$

Where k_0 is the reference intrinsic permeability (m^2), θ_0 and θ are the reference porosity and porosity respectively. The correction to intrinsic permeability is purely an empirical fit to this experiment, after other more conventional formulations (e.g. Carman-Kozensky; Carman 1956) appeared not to perform as well. The relative permeability of air was set equal to 1 at all times. The results were significantly improved over previous implementations without mechanical coupling (Figure 2.26). Despite the improvements, there remain difficulties in matching the rapid resaturation at the lower end of the sample.

The impact of the selected functional form on the intrinsic permeability is shown in Figure 2.27. Taking a classical porous medium view of the system, the swelling at the base decreases the notional 'porosity' while compacting the bentonite at the upper end of the sample, reducing intrinsic permeability. As time progresses the swelling becomes more uniform, reducing the variation in the intrinsic permeability. The reality, where the water bentonite system is much more of a continuum, would give a more complex picture, however for the physical relationships presently being adopted this description is self-consistent.

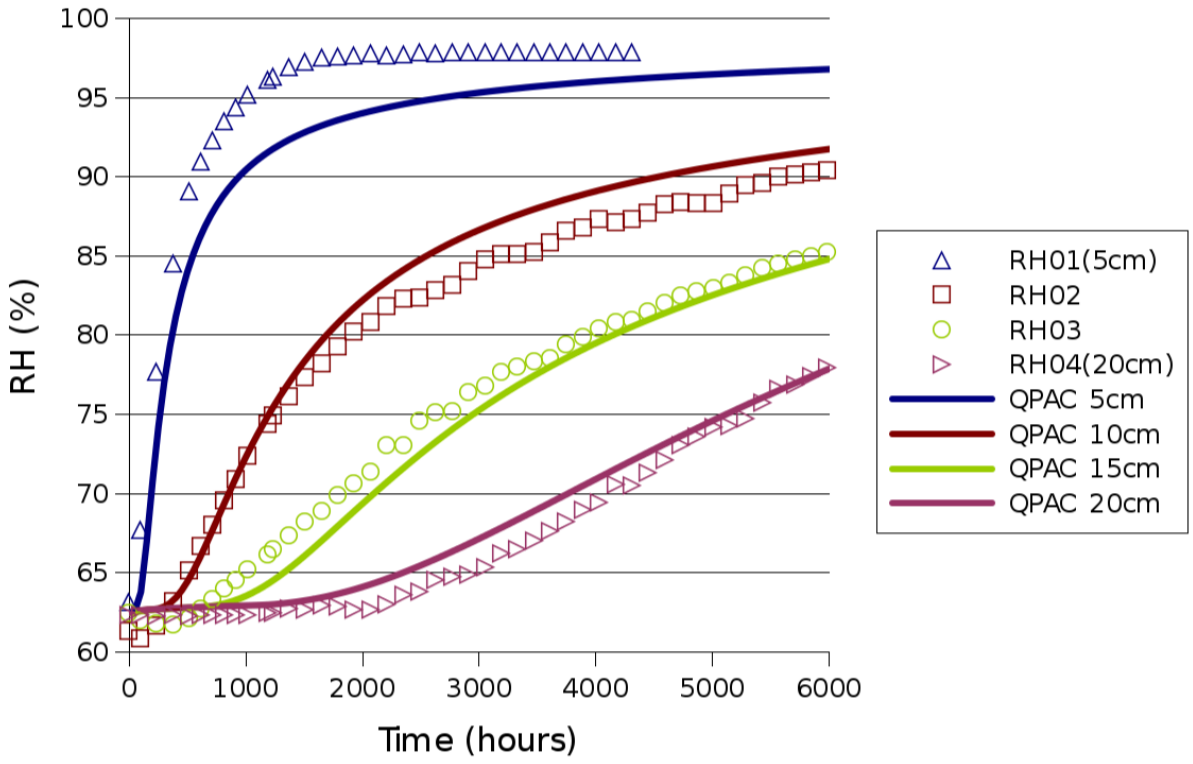

Figure 2.26. Calibration for the coupled hydro-mechanical QPAC model.

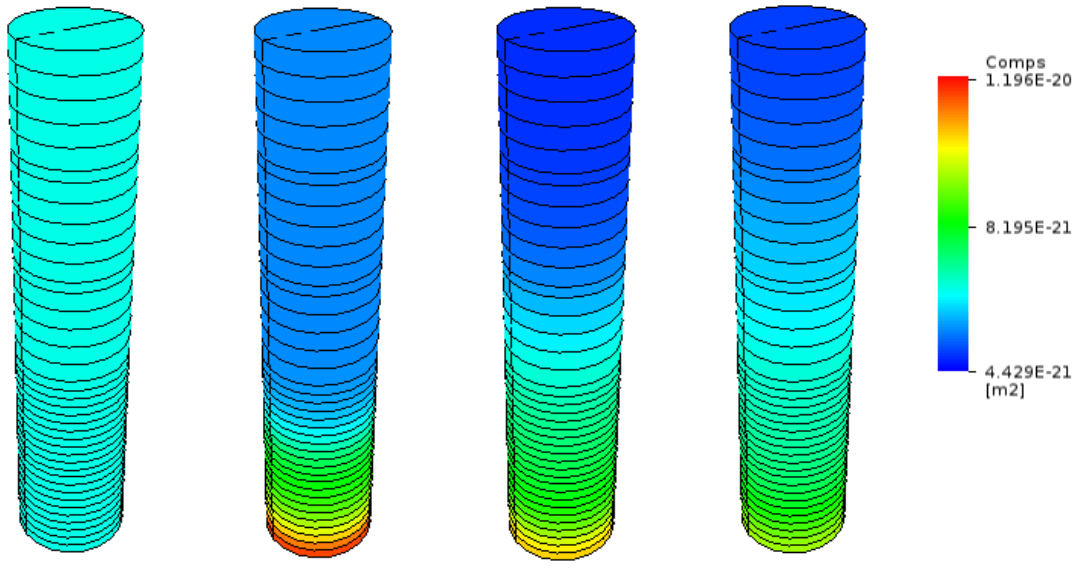

Figure 2.27. Intrinsic permeability in the model at (left to right), 0, 550, 1800 and 6000 hours respectively.

One area of potential significance that could explain the difficulties with the lower sensor is that the sensors themselves are quite large in volume. It is perhaps possible that the size of the lower sensor effectively reduces the volume of bentonite close to the water inflow such that resaturation appears faster. One might expect such effects to be more important close to the base of the model and not impact the higher measurement points to the same degree. Some adjustments to the QPAC model could be undertaken to investigate this effect later in the project. It is also possible that variations in compaction density (and hence permeability and porosity) could have been introduced during the construction process, although it is noted that from the experimental methodology, the experimentalists clearly took great care to prevent such variations.

Overall the coupled hydro-mechanical model provides a good replication of the Step 0 data and as such was sufficient for use for predictions in Step 1, but due to the lack of constraint on certain aspects of the model, providing accurate predictions purely on the basis of this model is likely to be challenging. It should also be noted that the consistency of the RWM model to the data was at least as good as any of the other teams' results in Task A, which also gives confidence that, given the processes being considered in the models, the result is as good as could be reasonably achieved at this stage of the work.

2.5 Step 1

2.5.1 Approach

The purpose of Step 1 was to provide blind predictions of the evolution of a 1/10th scale mock-up of one of the SEALEX performance tests on the basis of the Step 0 data and models. An overview of the experimental setup for Step 1 is given in Section 2.1.4. The primary outputs required from the predictions were:

- Vertical stresses with time and at the end of each phase.
- Vertical displacements with time and at the end of each phase.
- Total water inflow with time and at the end of each phase.
- Porosity distribution at the end of each phase.

The major problem in moving from Step 0 to Step 1 was that there is no single coherent dataset for the high density material being used in Step 1; nearly all of the samples used in Step 0 were at 1.67 Mg/m^3 dry density, while the Step 1 experiment was performed at a dry density of 1.97 Mg/m^3 (noting that the 1.97 Mg/m^3 dry density reflects the installed density at the field scale before expansion into the technological void during resaturation, which gives a final dry density of 1.67 Mg/m^3). The differences in density potentially gave rather different behaviours in Step 0 and the same could be reasonably expected in Step 1. This was notably the case in the zero suction oedometer experiment, which used the higher density bentonite/sand mixture, and showed dominantly elastic behaviour rather the dominantly plastic behaviour of the other samples (see Section 2.4.2). Whether this was due to the change in dry density (and hence microstructure) or due to the difference in suction (and hence water content) is unclear. However looking at more complex bentonite models such as the BBM (Gens and Alonso, 1992) suggests that the change in suction should not be having this effect; increases in water content should increase the likelihood of plasticity. This was exactly as observed in the other oedometer tests at 1.67 Mg/m^3 dry density and higher suctions.

Therefore, rather than immediately attempting Step 1 using an appropriate Step 0 hydro-mechanical model it was decided that it would be useful to use the literature to obtain a semi-quantitative prediction of the expected state of the bentonite at the end of each of the experimental phases.

2.5.2 Semi-quantitative Predictions

To provide some guidance on the expected outcomes of Step 1 for conditioning the models, some initial semi-quantitative estimates have been made. These estimates are based on data from Step 0 alongside understanding of bentonite behaviour from the literature.

Estimates of water uptake into the sample are made on the basis of the assumption that the volume of solid bentonite grains is constant and water fills the remaining free space (void space and technological void). Based on the Step 0 results, this assumption might be expected to underestimate the water injected into the sample. In Step 0, the water retention curve under constant volume conditions shows an increase in water content from 10.88 wt% at 65 MPa suction to 25.42 wt% at 0.01 MPa suction. This corresponds to 4.17E-6 m^3 of water injected into the sample, assuming water density of 1000 kg/m^3. The initial pore volume of the sample was 3.82E-6 m^3 which shows that the volume of water injected is almost 10% greater than that predicted by the initial pore volume.

Swelling pressure has been predicted based on the work of Wang (2012). Wang showed that swelling pressure is related to the final dry density of the sample after swelling into a technological void. Experiments were based on bentonite with a density of 1.97 Mg/m^3 that then swelled into different sized technological voids resulting in a range of final dry densities. A log-linear relationship was found between the swelling pressure and the final dry density. As these experiments are very similar in geometry to Step 1, the results of Wang (2012) are likely to be a good predictor of swelling pressures in Step 1. There is an assumption using these data that the samples were fully homogenised at the end of the experiment, but this was not fully verified.

The resaturation of the sample is expected to be initially heterogeneous. Bentonite closest to the water inlet and the technological void will swell as water enters the sample. The extent to which this heterogeneity remains in the experiment is unclear. Bentonite in resaturation experiments in the FORGE project (Talandier, pers. comm.) showed homogeneous resaturation at the end of the experiment, however there was evidence of differential swelling, locked in stresses and non-homogenous porewater pressure development. Since the samples in Step 1 are relatively small, we assume that saturation of the sample homogenises through the initial confined phase, although the observation that the experimentalists felt it necessary to add in water through the top of the sample during Phase 2b suggests there may be some inhomogeneity. During Phase 2 there will be greater swelling at the top of the sample because the bentonite is under less stress than the bentonite at the base of the sample. In Phase 3 there is likely to be some redistribution of water and solids back to a more homogeneous condition, although the final degree of homogeneity is unknown.

Estimates of the timing of the different phases in Step 1 depend on how quickly water moves through the sample as it saturates, which is a function of the permeability of the sample. In Step 0, we derived some permeability information by fitting the models to the infiltration test. However, the bentonite used in the infiltration test was compacted to 1.67 Mg/m^3 whereas the bentonite in Step 1 was compacted to 1.97 Mg/m^3 and then swells to 1.67 Mg/m^3 during

the initial resaturation and swelling into the technological void. A sample that has been compacted to 1.97 Mg/m^3 is likely to have a different arrangement of grains compared to a sample compacted at 1.67 Mg/m^3 and is therefore likely to have a different permeability. Even when the 1.97 Mg/m^3 sample swells to 1.67 Mg/m^3, the grain arrangement will be different from the sample compacted at 1.67 Mg/m^3 so there is no reason to think the permeability will be similar. Since we have no information on the intrinsic permeability of the bentonite, we are not confident in predicting the time dependent behaviour of the sample, however if the samples have reached an equilibrium (as the specification maintains), the we could potentially have more confidence in the end-state of each phase than the transient behaviour.

Based on the above discussion, quantitative predictions of the vertical stresses and the injected water mass at the end of each phase of the experiment have been produced to inform the quantitative predictions (Table 2.3).

Table 2.3. Estimates of vertical stress and injected water mass at the different phases of Step 1.

	Phase 1	Phase 2a	Phase 2b	Phase 3
Vertical stress (MPa)	3	0	0	0.2
Injected water mass (ml)	72.5	82	140	140

2.5.3 Quantitative Predictions

The limited amount of data available from Step 0, specifically the lack of radial stresses and complete information on swelling volumes under different stress states (these data are available for 0 and 0.1 MPa only), limited the confidence in the Step 0 hydro-mechanical model and its predictive application to Step 1. In order to provide some predictions, a two-model approach was taken in order to cover a range of reasonable behaviour. Because there is no coherent data-set from Step 0 that replicates the conditions found in Step 1, it was decided to combine different elements of the models from the Step 0 calculations through two different models. It was expected that by using both models as a prediction, the comparison would provide more information on the actual behaviour of the Step 1 experiment.

For the first model the semi-quantitative predictions (called 'SemiQuant') discussed in the previous section were used to calibrate a simplified version of the QPAC Step 0 hydro-mechanical model, using the standard suction formulation and mechanical model, but with a constant intrinsic permeability. The constant intrinsic permeability was chosen because the coupled permeability model developed for the infiltration test had only been used on a sample of density 1.67 Mg/m^3, and so there was little confidence that the model would be appropriate on the higher density sample. Calibration to the expected stresses was achieved through the adjustment of the relationship for elastic modulus.

For the second model (called 'Oedo'), the 'high density' version of the Step 0 zero suction mechanical model was used (Section 2.4.2), complete with adjusted suction model and the intrinsic permeability as a function of porosity, as used in the hydro-mechanical calculations (Section 2.4.3.2). This model combines all the dynamic elements developed during Step 0.

The QPAC model setup was identical for both models, as illustrated in Figure 2.28. The model is a 2D cylindrical representation, with non-linear time and displacement dependent boundary conditions enabling the initial lack of radial confinement, and the change in conditions at the upper boundary through the different experimental phases to be represented in a single run. In parameterising the model and the dynamic boundary conditions, it was assumed, in the absence of any other information, that based on the practicalities of conducting the experiment (the work was part of a PhD thesis), the initial confinement (Phase 1) lasted no longer than a year, and so the model would transition from Phase 1 to Phase 2 after one year, irrespective of the transient state of the experiment.

It should be noted that on the sides of the bentonite, a roller boundary was specified, thus specifying zero friction between the bentonite and the side of the confining cell. The degree to which this is reasonable is unknown, but in the absence of any other information provided in the specification, this seems a reasonable starting assumption.

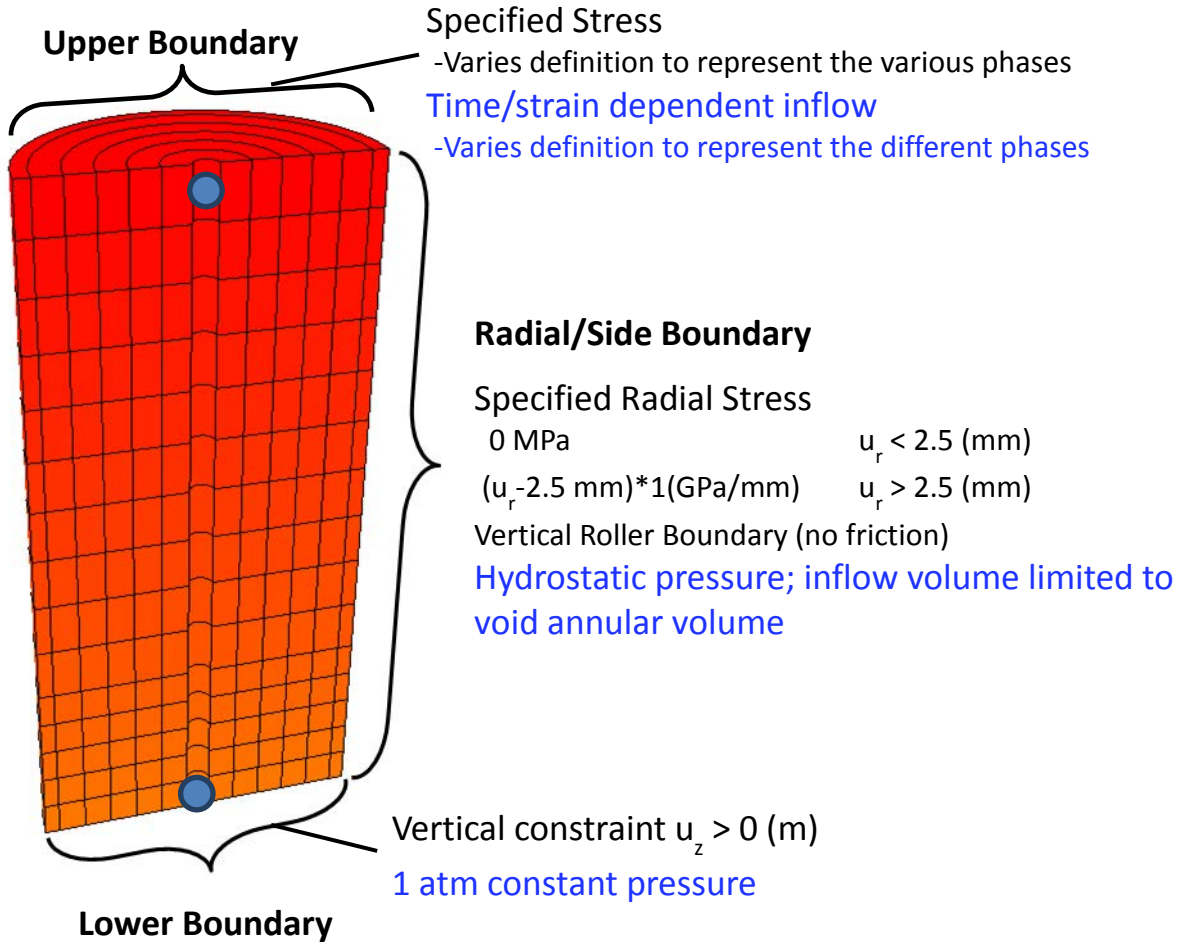

Figure 2.28. Illustration of the boundary conditions and discretisation used for the Step 1 models. Measurement locations for void ratio are shown with the blue circles.

On the dynamic mechanical boundaries, orthogonal confinement was represented by a non-linear stress boundary condition that increased linearly with displacement and very steeply once a threshold displacement was reached. In the case of the upper boundary, the stress was also controlled by the experimental phase, being set to zero during Phase 2.

The upper and lower hydraulic boundaries were simple constant fluid pressure conditions, the upper boundary allowing gas outflow at all times and the bottom boundary preventing gas inflow. The upper boundary only permitted water inflow once Phase 2b had been reached. In terms of the radial hydraulic boundary, following the information provided by Millard and Barnichon (2013), it was assumed that the technological void around the sample was initially flooded. This was replicated through a non-linear mixed boundary condition where the water was at a hydrostatic condition (it was assumed that the expanding bentonite did not significantly compress the water in the void, but rather it was drawn into the clay). The total inflow into the sample from the annular void was calculated dynamically and the inflow to the sample from the void was then reduced using a simple scaling factor f_w (equation 15), thus limiting the total water ingress from the sides of the sample.

$$f_w = 1 - \frac{I}{I_T} \tag{15}$$

Where I is the amount of water that has entered the sample from the annulus (kg) and I_T is the total amount of water in the annulus initially (kg).

2.5.4 Results

The evolution of the samples is shown in Figure 2.29 to Figure 2.31 for the SemiQuant case. The SemiQuant and Oedo cases give very similar displacements and water uptake, so there is little benefit in showing both sets of results. The expansion of the base of the sample before it impacts against the side of the test cell can be seen quite clearly in Figure 2.29 and Figure 2.30, and the extensive vertical expansion can be seen in Figure 2.30 and Figure 2.31.

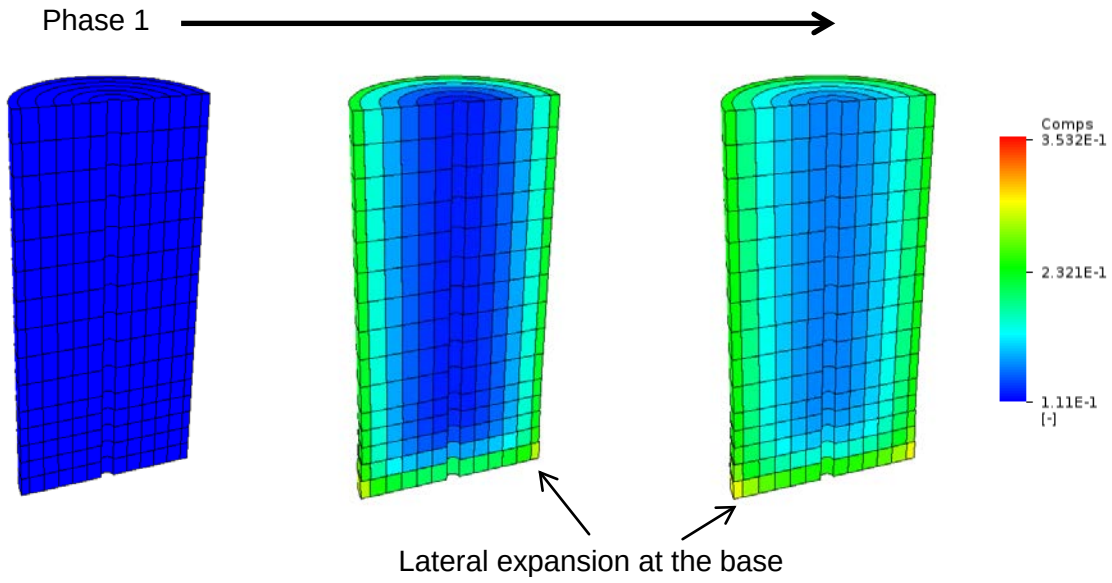

Figure 2.29. Early evolution of Phase 1, water content with no displacement exaggeration

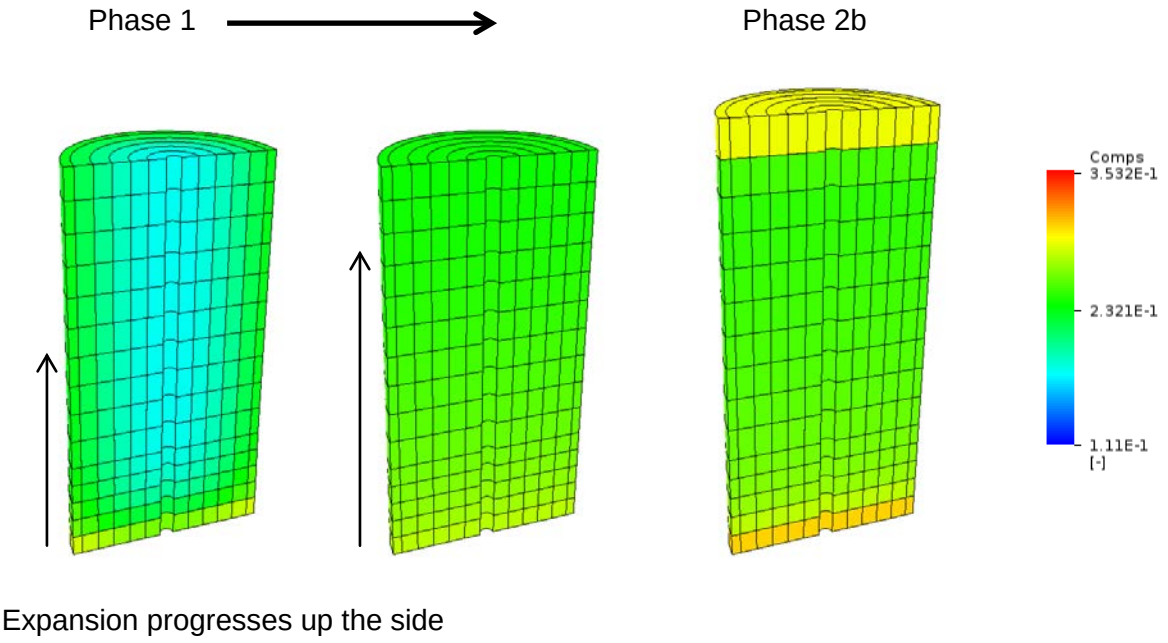

Figure 2.30. Late evolution of Phase 1 and the start of Phase 2b, water content with no displacement exaggeration

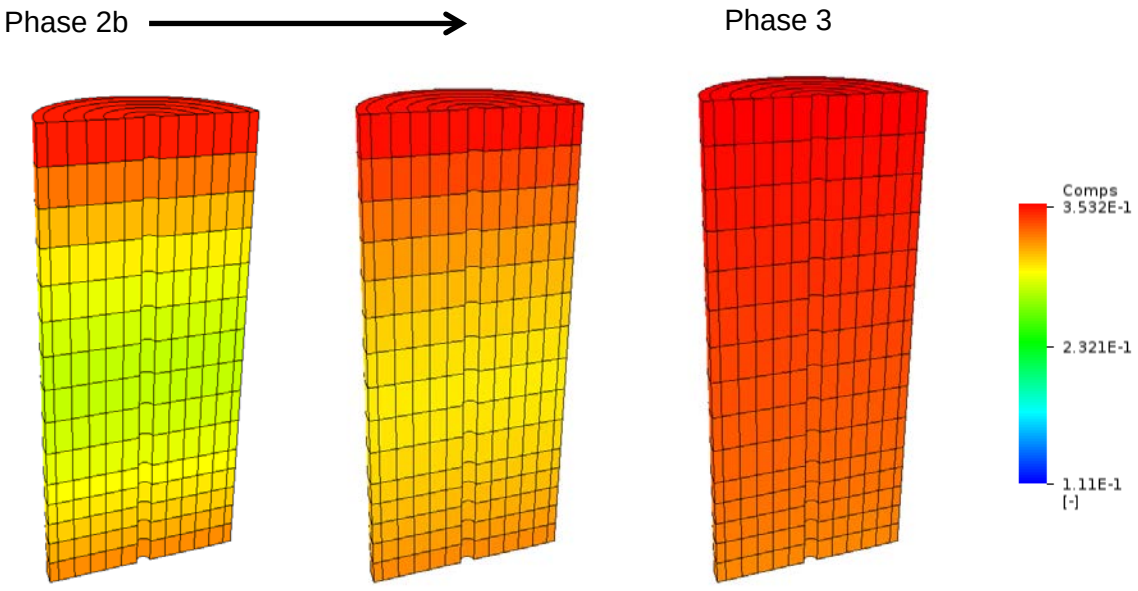

Figure 2.31. Late evolution of Phase 2b and the start of Phase 3, water content with no displacement exaggeration

The evolution of the average vertical stresses (simple weighting by area across the upper surface) for the two tests is shown in Figure 2.32 and Figure 2.33. As expected, the SemiQuant case shows vertical stresses approaching 3 MPa at the end of Phase 1 with negligible stresses in Phase 3 (they are of the order of 0.02 MPa), however the timescale of the response in Phase 1 is quite slow. In contrast the Oedo test with the dynamic intrinsic permeability shows a very fast response, equilibrating at approximately 5.8 MPa. Vertical stresses in Phase 3 are of the order of 0.2 MPa.

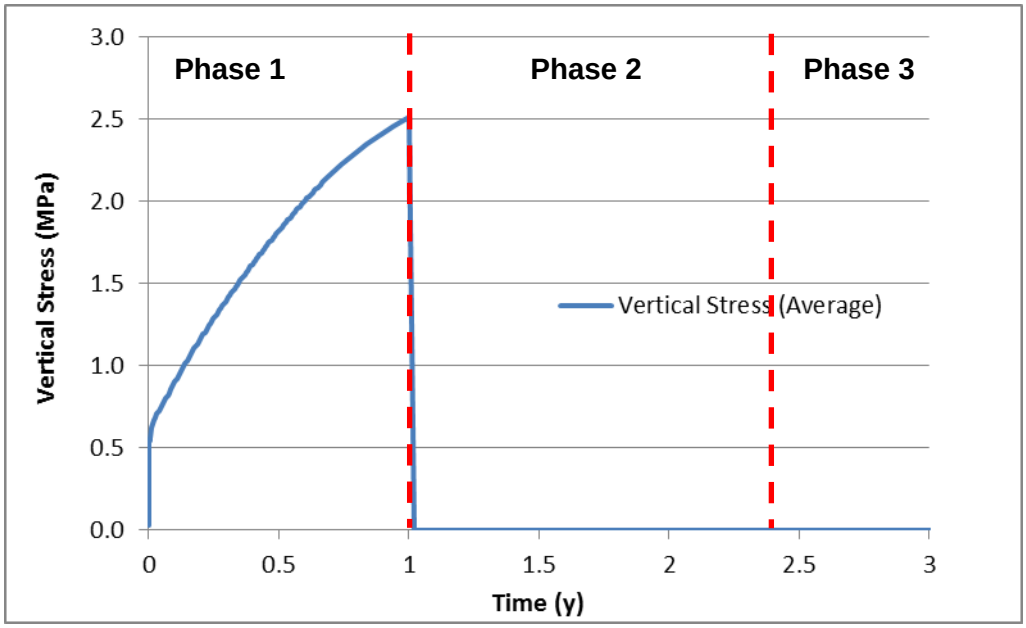

Figure 2.32. Vertical stress evolution for the SemiQuant case.

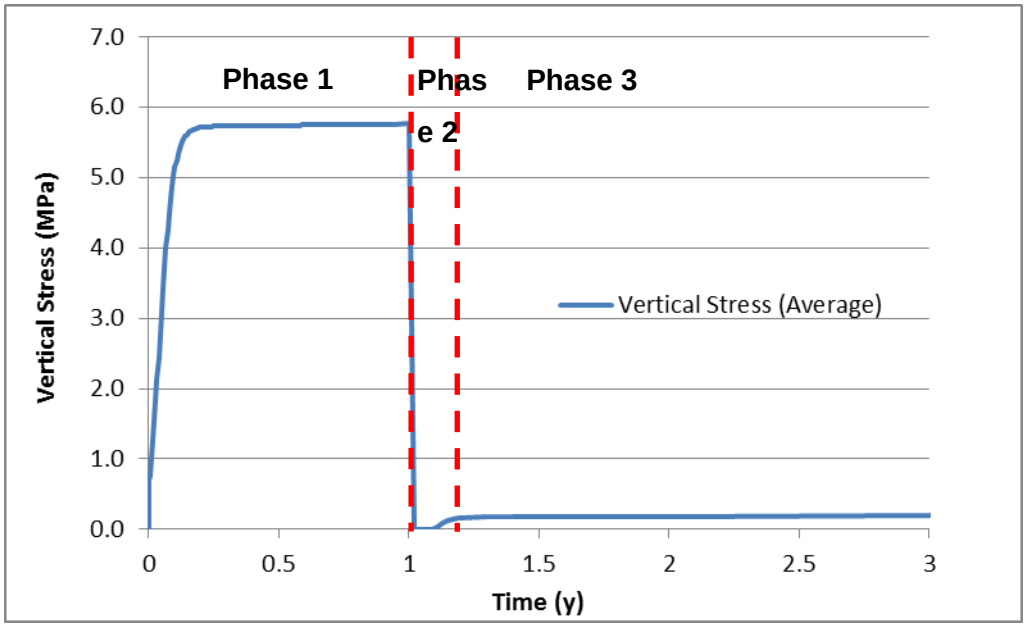

Figure 2.33. Vertical stress evolution for the Oedo case.

Void ratios at the upper and lower centre of the samples (Figure 2.28) for the two models show the expected evolution (Figure 2.34, Figure 2.35); the lower stresses of the SemiQuant case give rise to less plastic deformation hence the final void ratios are almost homogenous across the sample, whereas the Oedo case shows some minor variation. Both of these results are consistent with the Step 0 oedometer results, where significant compaction would not be expected at low vertical stresses, assuming the radial stresses, for which we have no data in Step 0, are also low. The rapid changes in void ratio at the start of Phase 2 (after 1 year) reflect the high degree of elasticity predicted at low suctions from the Step 0 data at 1.97 Mg/m^3; if the experimental data do not shown this response it suggests that the selected Step 0 model is unreliable for this case.

Total water uptake was similar for both models, with the Oedo case estimating slightly more total water uptake. The comparison of water uptake against Phase is given in Table 2.4. Overall the results are largely consistent, the differences mainly being caused by the differing water retention curve for the 'Oedo' case.

Table 2.4. Comparison of water uptakes by the two numerical models and the semi-quantitative estimates from the previous section.

Model	End Phase 2a (ml)	End Phase 3 (ml)
Semi Quantative Prediction (Table 2.3)	82	140
SemiQuant	84.6	129.2
Oedo	87.6	141.8

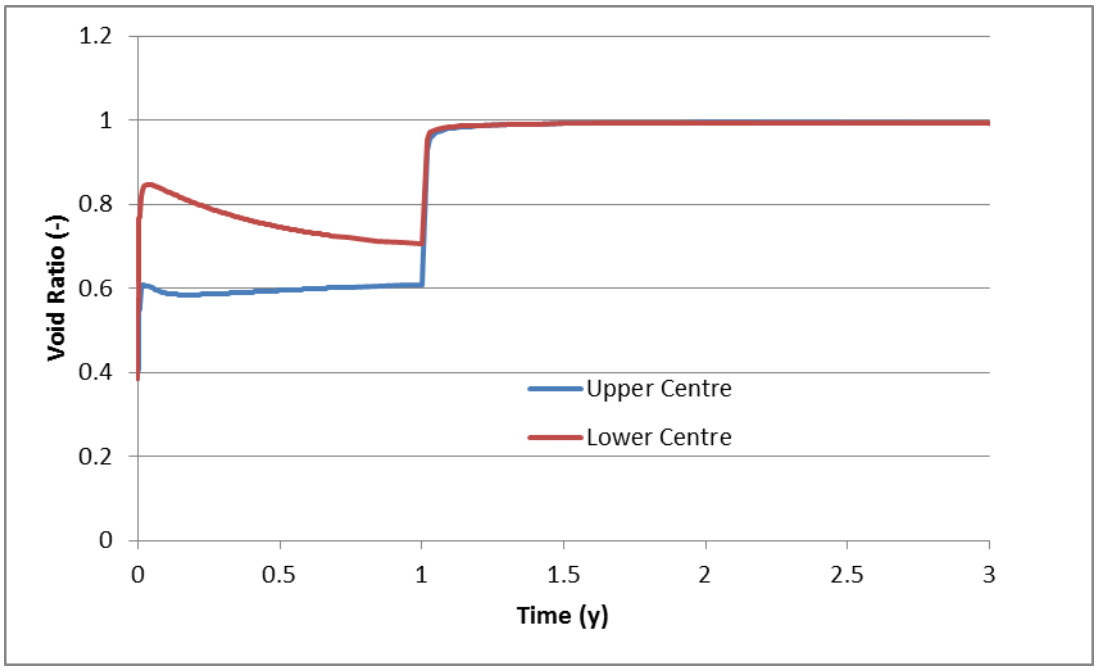

Figure 2.34. Void ratio evolution for the SemiQuant case.

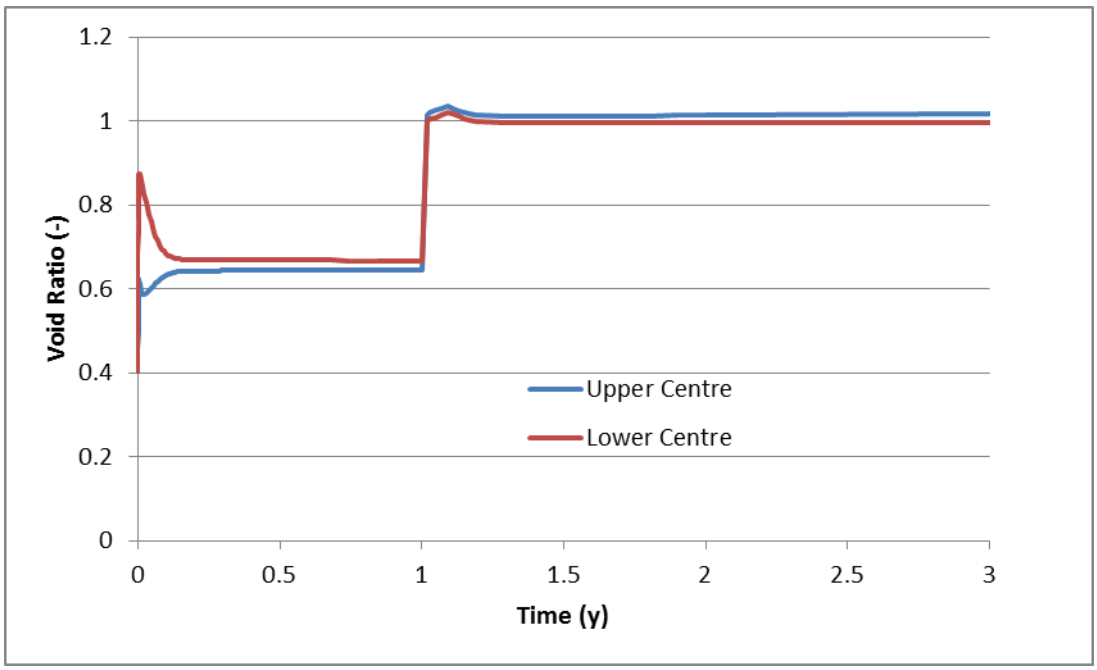

Figure 2.35. Void ratio evolution for the Oedo case.

2.5.5 Comparison against Step 1 Predictions

The Step 1 data have not yet been released to teams and hence only the Task management have been able to make comparisons. Some graphical comparisons were made at the April DECOVALEX workshop, and the following summary points can be made from what was presented:

- Of the teams in DECOVALEX Task A only the RWM team and IRSN (task management internal team) made any predictions against Step 1.
- The predictions of the IRSN team were made without any supporting documentation or comparisons against Step 0 and as such are difficult to comment on, other than to note their model gave the best overall response compared to the available data. The predictions were made using CodeBright with the BBM and utilising their extensive database of MX-80 parameterisation.
- The NDA team predictions generally bracketed the actual results as expected and gave a reasonably good prediction of timescales of evolution and water inflow rates.
- Stresses at the end of Phase 1 were overestimated by all of the RWM models, with the Step 1 experiment showing stresses of only ~2 MPa – surprisingly low; however stresses for Phase 3 were well reflected by the RWM models.

Not all the data are available from the experiment as yet because the sample is currently being dismounted and analysed for density variation.

Given the relative lack of suitable data from the Step 0 experiments to inform the Step 1 predictions, overall the degree of similarity between the RWM predictions and the experimental data is encouraging. However a full analysis of the blind prediction will need to wait until the experimental data are made fully available.

2.6 Beginnings of a New Constitutive Model

As noted in Section 2.3, in parallel with using and developing the more ‘standard’ approaches that have been attempted to represent HM processes in compacted bentonite, a parallel stream of work, largely under the PhD student, is being conducted attempting to produce better and simpler constitutive models of bentonite, starting from the essentials of bentonite mineralogy and looking beyond the standard soil mechanics approach often taken with swelling clays. At the present time RWM are the only team looking specifically at these issues within DECOVALEX-2015. The work is intended to complement the work described in the previous sections and use it to improve the formulations used in QPAC and OpenGeoSys for Task A when opportunities arise.

This summary outlines the fundamental points being investigated in the process of developing a new constitutive model of bentonite behaviour during saturation for DECOVALEX-2015. The work builds on the discussion of basic bentonite theory given in Section 2.2, provides a brief overview of current approaches (to complement the current work under Step 0 and 1) and suggests a way forward using the planned non-linear elastic approach.

2.6.1 Overview of Existing Model Approaches

Previous modelling approaches have used the concept of elasto-plasticity to explain the mechanical behaviour of bentonite e.g. the Barcelona Models (Gens & Alonso, 1992; Josa, Alonso, & Gens, 1990; Sánchez et al., 2005), the ClayTech model (Börgesson et al., 1995), and the Cam-Clay theory (Borja, 2004; Borja & Lee, 1990). It is this class of approach that was taken as a starting point to address Step 0 and 1 (Section 2.4 and 2.5). Alternatively, other modelling approaches include poro-elasticity within a state surface (Nguyen et al., 2005), and non-linear elastic models (Cui et al., 2002).

As discussed in Section 2.4.2 the Cam-Clay theory of elasto-plasticity defines the system behaviour in terms of the volumetric stress (p) and the deviatoric stress (q). A yield surface is defined which, once exceeded, causes plastic deformation i.e. irreversible strains develop within the sample. Elastic behaviour is observed under stress conditions less than the yield ellipse. The Cam-Clay approach can be used to fit experimental data but is not a constitutive model developed from first principles of the bentonite properties. Therefore it has the advantage that only 4 main parameters are required to describe the clay behaviour, but it does not explicitly address the balance of forces acting within the bentonite micro and macro-structure, and as such, calibration between the two different density materials becomes inconsistent.

The ClayTech elasto-plastic model is essentially a modified Cam-Clay method with an extra modification in order to more accurately represent strain hardening and softening behaviour. Elasticity is defined by empirically derived functions for the volumetric and deviatoric behaviour (Börgesson et al., 1995). In terms of the plasticity model, it uses a combined yield and failure surface for over-consolidated clays above the Cam-Clay critical state line and a transition line between the two. An associative flow rule is used for the yield surface cap while a non-associative flow rule defines the transition line (Börgesson et al., 1995). The concept behind the model is that the stress-strain curves obtained in experiments are not simply bi-linear elastic and plastic; the relationship is closer to a hyperbolic shape. Therefore the interpretation has been that an early onset of plasticity causes this change in the stress-strain relationship and the model was developed to reflect this (Börgesson et al., 1995).

The Barcelona models have become the standard tool for bentonite modelling and were developed to incorporate the importance of the microstructure and its interaction with the macrostructure. Similarly to the Cam-Clay model a yield surface is defined, but in these models the surface is in terms of three independent variables; net mean pressure (p), deviatoric pressure (q), and suction (s). In the BBM and BExM the yield surface in terms of p and s is termed the Loading-Collapse Curve (LC Curve) and is analogous to the failure ellipse in the Cam-Clay model (Gens & Alonso, 1992; Sánchez et al., 2005). Elastic deformation proceeds with increasing p until the LC curve is reached and then plastic deformation proceeds with the change in suction and pressure controlled by the location and shape of the LC curve (as defined in the failure ellipse). The key control of the interaction between the two structural levels is the definition of the failure ellipse. Two interacting functions that describe the fabric of the material control the location of the failure ellipse in p-q space i.e. if the fabric of the material is loosely packed this increases the importance of the macrostructure with respect to the microstructure and consequently reduces the size of the failure ellipse. Failure and irreversible strains can then occur in the macrostructure with less pressure. However if the material is densely packed then the volume of void that can undergo plastic deformation is greatly reduced and elasticity can be observed at greater

stress i.e. the failure ellipse is larger. In the BExM a function is included to allow the microstructure to invade the macrostructure porosity. This flexibility along with calibration databases from many experimental efforts e.g. FEBEX, BACHUS, and DECOVALEX, mean that the Barcelona models are widely used.

In contrast to the Barcelona models, a poro-elastic approach implementing a state-surface allowing the poro-elastic constants to be expressed in terms of the void ratio and applied load was used by Nguyen et al. (2005) to model the FEBEX heater experiment. This method uses a pseudo-Biot's coefficient and the experimentally derived state surface to determine the volumetric behaviour of the sample. A similar model approach was proposed for the modelling of the BACCHUS2 experiment, however, it is limited by not being able to model irreversible and path-dependent effects, nor considering the suction change induced by deviatoric strains and the influence of deviatoric stress on volumetric behaviour (Alonso et al., 1998).

Also, in contrast to the elasto-plastic method, an elastic non-linear model was developed to explain the volume behaviour of Ca^{2+} bentonite during dry-wetting and loading-unloading cycles (Cui et al., 2002). This model introduces the concept of a Critical Swelling Curve; (CSC) there is a threshold suction pressure at which the volume change (increase) due to reduction in suction pressure is neutralised by the applied stress. This CSC is used to determine whether the sample is undergoing volume change or if the applied stress is enough to keep the sample at a constant volume. A significant positive for this model is the simplicity - it only requires 6 parameters.

2.6.2 New Proposed Non Linear Elastic Model Approach

The constitutive mechanical model of a non-linear elastic model, is based upon the idea that the distance between the interlayers is proportional to the mechanical properties of the material i.e. the shorter the distance the stiffer the material becomes. As the distance between sheets is significantly controlled by the amount of water in the interlayers (especially during swelling), this produces a strong coupling between the water content and the mechanical properties. Bond strength between the interlayer water and cations with the clay surface is strongest in the first layer and decreases in strength with increasing water layers (Pusch et al., 1990; Yong, 1999). Pusch et al. (1990) and Pusch and Yong (2006) also indicate that the number of hydration layers in the interlayer give the montmorillonite stacks different stress/strain properties and also control the swelling potential. The effect of varying elastic properties with water content can also be seen in the consolidation tests at constant suctions where the higher suction samples appear to have a higher preconsolidation pressure. Lower suction samples have a lower preconsolidation pressure because the higher water content results in a weakening of the elastic constants that define the stiffness. The aim of developing this constitutive model is to relate the forces present in the bentonite system and the mechanical properties of the material.

The proposed non-linear elastic approach for the project is seeking to relate the elastic properties to the strain and the percentage water content by mass. The simple formulation does not require the definition of the plastic regime and the yield surfaces, and consequently is computationally cheaper. The aim in developing the constitutive model is to ground the empirically fitted functions in the physics of the system.

Fortunately, the high dry density of the samples used in the Task A experiments means that the fabric of the sample is likely to be dominated by the microstructure i.e. there will be few

macro-pores except as the bentonite swells into the annular void and, as such, the influence of the reversible microstructural behaviour dominates the process. This lends it to an elastic approach.

During swelling, percentage water content by mass increases i.e. the mass of the bentonite does not change but the water content increases. It has been shown that the mass of air within a sample of Ca^{2+} bentonite remains constant throughout repeated wetting and drying cycles (Delage et al., 1998). This study preceded the development of the non-linear elastic model of Cui et al*.,* (2002). If this can be extrapolated to Na^{+} bentonites (bearing in mind the differences in structure and behaviour between Ca^{2+} and Na^{+} bentonites) this means that the change in void ratio as a result of swelling deformation can be directly related to the water content.

Therefore, the plan is to assign a local void ratio, calculate the local volumetric strain after each time step and update the void ratio with the volume change. The coupling with the hydraulics arises because the change in suction pressure calculated from the hydraulics is used in the stress conditions of the mechanical formulation as a source term for deformation, and the change in void ratio during swelling is directly proportional to the change in water content. The elastic properties of the material will be a function of the strain history of the sample i.e. the Young's Modulus will increase with increasing compressive strain (similar to the Cam-Clay Swell/Compression Index) and decrease with expansion. In its current form the behaviour is described by an empirical formula relating strain to changing elastic properties. However, future work will investigate how a relationship between elastic properties and water content (which in swelling especially can be related directly to the strain) could be defined in terms of the balance of forces acting within the bentonite microstructure.

Some initial models using such an approach have been applied to the oedometer experiments (Figure 2.36). The results are currently preliminary, and the discussion somewhat lengthy, however initial results are very positive, providing at least as good a fit to the experimental data as those obtained using the more conventional Cam-Clay model in QPAC (Section 2.4.2). These results are preliminary and will be discussed in more detail in future reports.

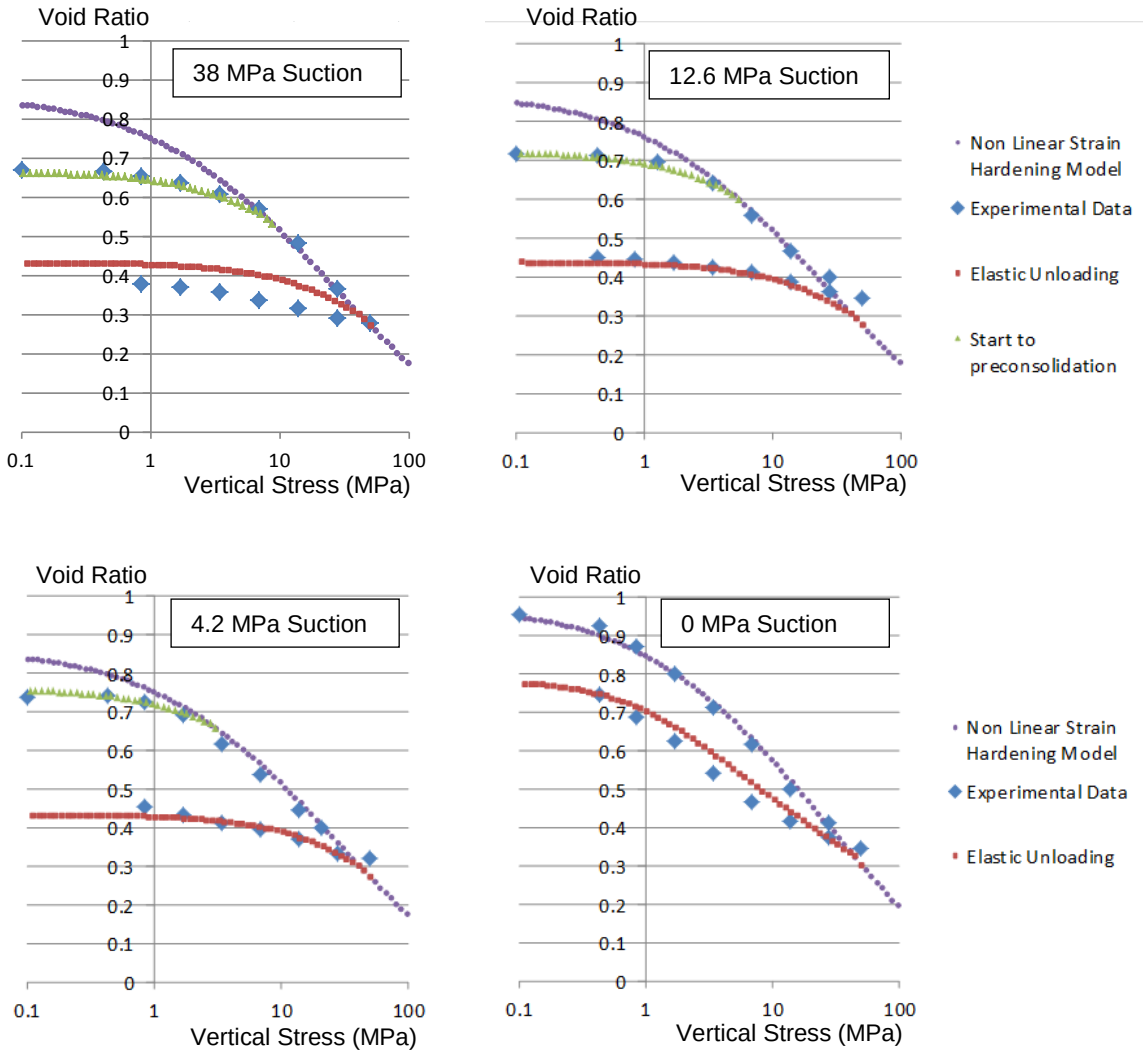

Figure 2.36. Comparison of fits using the prototype non-linear elastic model and the experimental data. Internally self-consistent parameterisation is used across the four oedometer tests

2.7 Task A Summary

Good progress has been made in participating in Task A of DECOVALEX-2015 and the Task A management Team have commented favourably on the amount of work that has been done by the RWM team. The work has followed two streams: The first using conventional and 'as simple as possible' formulations to reproduce laboratory experiments and to provide predictions of larger, more complex laboratory experiments – this work has been primarily done using QPAC; the second stream of work has been involved in understanding the previously developed constitutive models of bentonite and moving towards a newer model that is more physically-based, rather than empirically-based, and is consequently easier to parameterise (this work has been done primarily with OpenGeoSys as the modelling tool).

The work has illustrated that it is possible to reproduce the hydro-mechanical experiments using physically plausible models, but the use of even simple conventional process models requires a great deal of supporting empirical data, not all of which is available through the Step 0 or Step 1 experiments. As such it seems that to develop robust predictive models for the later parts of the project will require either:

- Interpretation and calibration against other experimental data in the literature in order to broaden the range of data used to constrain the models; or

- Adoption of well-proven but complex constitutive models such as the BBM, and hence being able to adopt the parameter database associated with such models without having to reinterpret multiple experiments.

Given that many elements of the BBM have been implemented already in the QPAC Task A models, and that the next Step (Step 2) is being delayed to allow teams to continue work on the bentonite model in light of the Step 1 data, it would seem to be most efficient to implement the BBM fully within the QPAC case files (note this does not require any code development – the BBM is essentially an input to the standard QPAC mechanical module). The QPAC BBM model can then be tested against standard literature cases as well as the Step 0 data, and the Step 1 data when they become available.

In terms of the work focussing on the new constitutive model, the implementation and testing of the BBM, as well as application to Step 0 and Step 1 data, would provide a valuable additional dataset to prove the validity of the new model, as well as allowing further consistency and confidence building between the two approaches.

Work is ongoing under this task and future plans include refining the Step 1 model and modelling the hydraulic behaviour of the host rock at Tournemire, before combining the bentonite and host rock models to attempt to represent the selected in-situ SEALEX experiments (Figure 2.7). Progress on this work will be presented in future annual reports.

3 Task C – THMC processes in single fractures

3.1 Task Overview

The RWM team is one of 6 teams contributing to the technical work of the Task:

- Chinese Academy of Sciences (CAS)
- Imperial College London (PhD student), funded by NDA
- Quintessa and University of Edinburgh, funded by NDA
- Technical University of Liberec, funded by RAWRA (Czech Republic)
- UFZ Leipzig, funded by BGR, Germany
- US NRC (internal team)

Consistent with Task A, only the results of Quintessa and the University of Edinburgh are reported here, but comments and comparisons with other teams' work is made where appropriate.

3.1.1 Experimental Overview

The coupling of chemical, hydraulic, thermal and mechanical processes for fractured rocks is an extremely complex area of scientific research which may have a significant bearing on the potential design and performance of radioactive waste disposal facilities. The purpose of Task C1 under DECOVALEX-2015 is to:

1. Investigate and mathematically model the results of the two experiments described by Yasuhara et al. (2006) and Yasuhara et al. (2011), which observe coupled THMC responses in single fractures.

2. Investigate, develop and test robust process models for the representation of coupled THMC processes in fractured rock by using the experimental data and the results of the modelling work above.

The emphasis of this work is to gain understanding of possible physical process models that can be used to explain the results of the experiments. The two experiments are well described in the two references given, hence only a summary is provided in Sections 3.1.2 and 3.1.3.

The two experiments consider hydraulic and chemical analysis of water flowing through laboratory samples of novaculite (Yasuhara et al., 2006) and granite (Yasuhara et al., 2011). In both cases, the fractures had been induced by the experimentalists, deionised water was used as the permeating fluid and the samples were under a significant confining pressure. The 'fresh' nature of the fractures and the use of deionised water ensure a rapid initial

chemical interaction between the fluid and the rock. The artificial nature of the fractures also means that mechanical effects may be significant early in the experiment; hence there is a need to be careful to separate the chemical and mechanical effects as far as practicable. It is also clear that there is significant uncertainty in all aspects of the parameterisation of the system and as such it will be important for the Task to be able to understand the significance of different teams' choices regarding approaches to processes and associated parameterisation.

Of the two experiments the novaculite is geochemically much simpler than the granite case and is much better constrained in terms of initial and final fracture aperture distribution. In contrast, for the granite case single measures of bulk 'aperture' are derived from the flow data and very little other fracture structure data appears to be available, aside from some interesting SEM data. As such the granite case has considerably greater uncertainty both from the relatively complex geochemistry and from the relatively sparse fracture structure information.

The experimental setup and results for each experiment are discussed briefly in the following sections.

3.1.2 Novaculite Experiment

The experiment consists of an artificially fractured novaculite (99.5% Quartz) placed in a hydraulically sealed pressure vessel (Figure 3.1) around which a constant confining pressure of 1.72 MPa was applied. De-ionised water is applied through the sample and differential pressures measured at the outlet and inlet. The whole apparatus can be heated, hence raising the temperature of the water, sample and pressure vessel.

Prior to assembly, both sides of the fracture were scanned using a 3D laser scanner system which gave measurements on a square grid of size 0.05 mm across the 50.0×89.5 mm fracture surface. This creates approximately 1.6 million datum points per surface. Statistical analysis of the fracture topography was not performed by Yasuhara et al. (2006), however this will be considered in future work.

The experimental procedure was relatively complex involving changes to both temperature and flow rates with time (see Figure 3.2). It can be seen that the early part of the experiment is isothermal, with only variations in water flow rates, however the variations in temperature and flow rate are quite large in the isothermal phase.

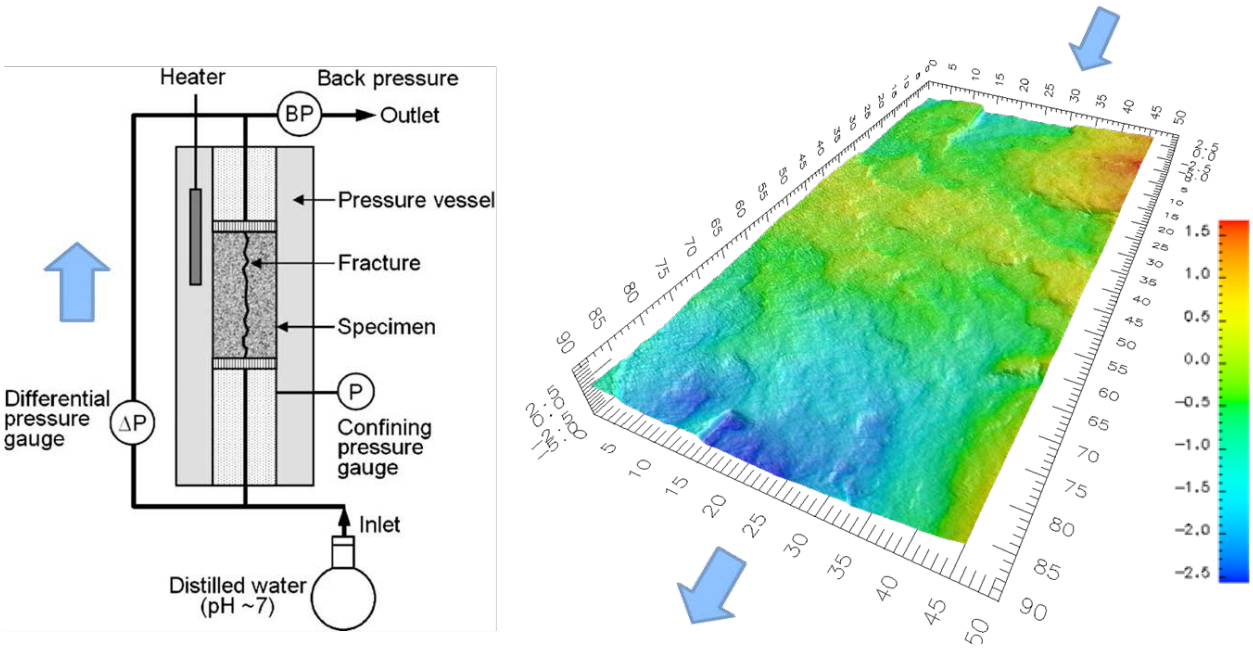

Figure 3.1. Schematic illustration of the experimental apparatus for the novaculite experiment (left, from Yasuhara et al., 2006) and the measured topography of the fracture surface (right, no vertical exaggeration). Blue arrows indicate the normal flow direction of water. Note that the confining fluid is not shown explicitly on the schematic diagram.

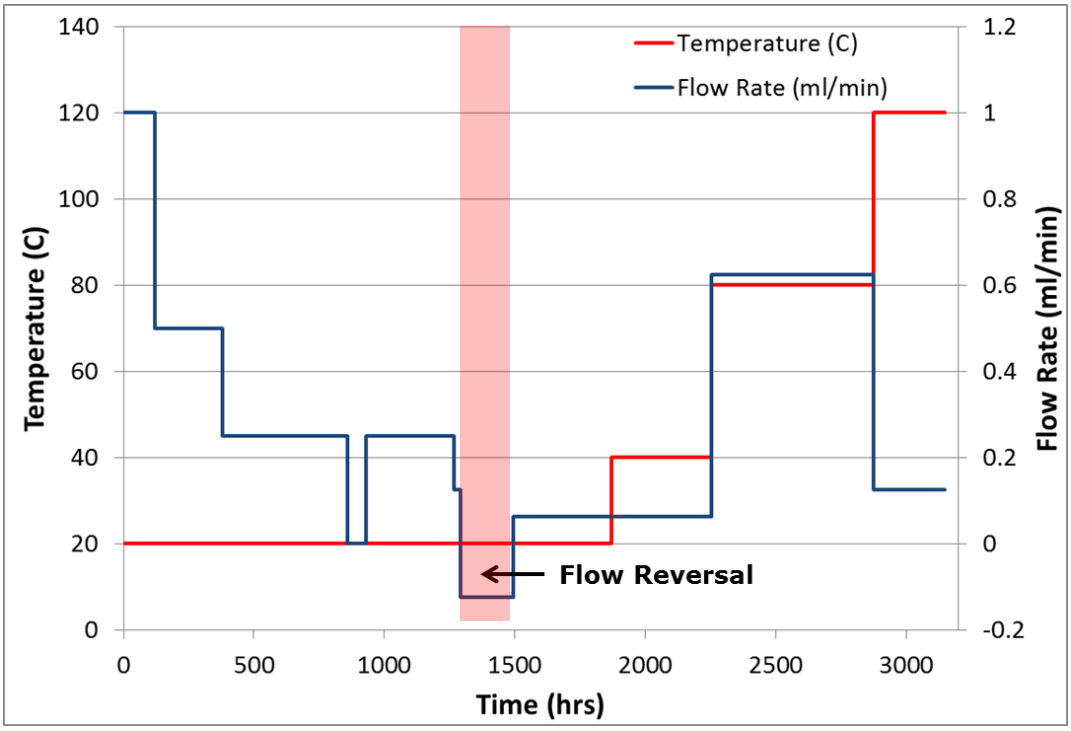

Figure 3.2. Temperature and flow rate across the sample with time. Flow reversal period is highlighted in red.

Overall the available data for the experiment are:

- Initial fracture surface topography (both surfaces – see above).
- Input water flow rates with selected pH measurements.
- Outflow water silicon concentrations (ppm) and selected pH measurements.
- Differential water pressure across the sample.
- Confining pressure (constant at 1.72 MPa)
- Post experiment X-Ray CT scan of the sample.
- Post-experiment aperture information from Wood's Metal injection.

The evolution of differential pressures and silicon concentrations are shown in Figure 3.3 and Figure 3.4. It is clear that there are strong correlations between flow rate changes and the implied hydraulic aperture and that the influence of temperature changes is particularly strong above 40 °C. However there is considerable 'noise' in the silicon concentrations and very little in the way of trend or sharp changes during the initial constant temperature period. It is unclear to what extent this 'noise' is masking any changes caused by the flow rate changes when the temperature is held at 20 °C.

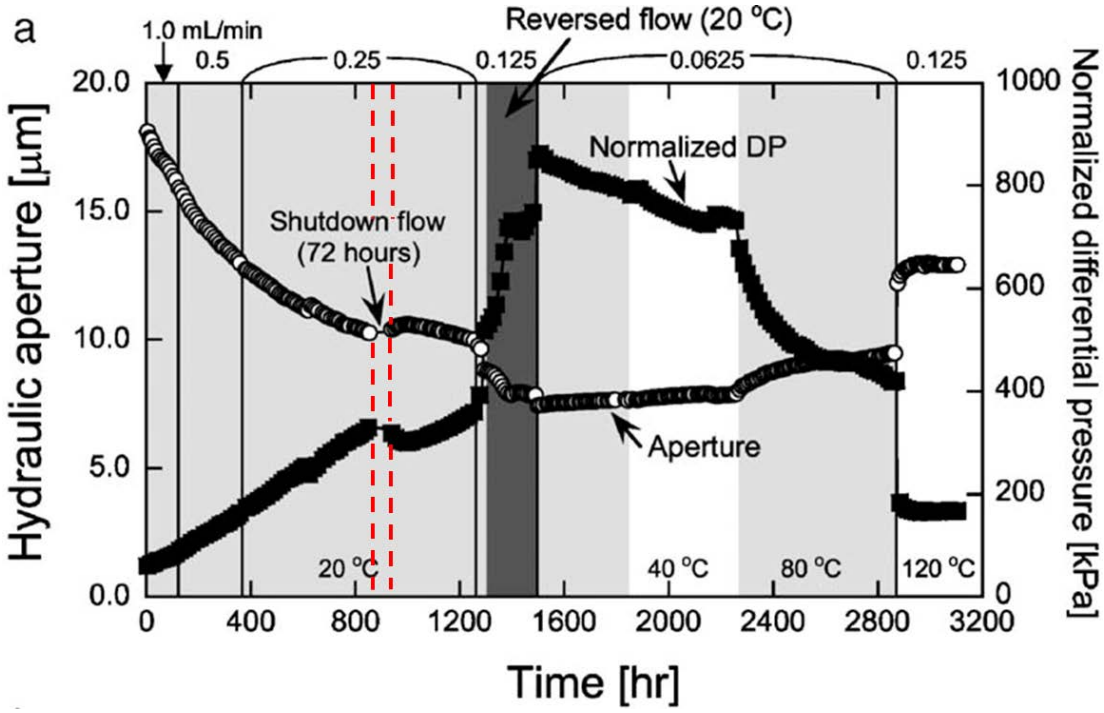

Figure 3.3. Normalised differential pressure across the sample and implied hydraulic aperture (using the parallel plate cubic law) for the novaculite experiment (adapted from Yasuhara et al. 2006). Grey/white shading indicates temperature changes.

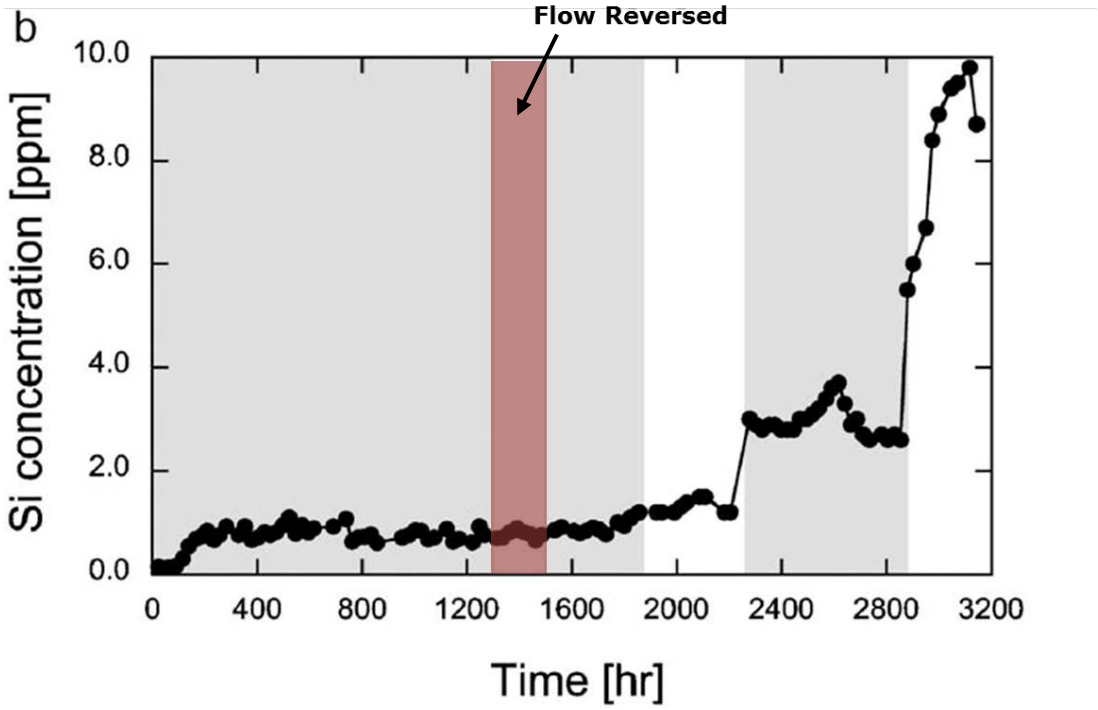

Figure 3.4. Measured Si concentration in the outflowing water for the novaculite experiment (adapted from Yasuhara et al. 2006). Flow reversal period is highlighted in red. Grey/white shading indicates temperature changes as per Figure 3.3.

3.1.3 Granite Experiment

The granite experiment is similar to the novaculite experiment, but with a few important details:

1. The experiment consists of three Mizunami granite samples each with an artificial fracture.

2. Each sample has a different combination of applied thermal load, confining pressure and differential water pressure. Maximum temperatures were 90 °C. Overall the flow and temperature evolution applied to the sample are much simpler than for the novaculite case.

3. There are no topography data for the fractures before the experiment started, only SEM data of the fracture surfaces upon completion.

The task leadership decided that because of the increased complexity of the granite experiment relative to the Novaculite, as well as the absence of fracture topography data, the granite experiments would be deferred for consideration until later in the Task (see Section 3.1.4). Hence, these experiments are not described further in this report.

3.1.4 Task Structure

A fuller discussion of the task structure and the reasoning behind the approach is given in Bond (2013b), however in summary, the following structure has been adopted:

- **Step 0**: Basic benchmarking - Novaculite:
    - Using primarily fracture topography data from Yasuhara et al. (2006) to reproduce the observed flow rate at the start of the experiment only. The objective here is to attempt, if possible, to reconcile the fracture topography data with the observed initial flow rates and the initial conditions for the fracture.
    - Represent simple batch experiments of silicate dissolution in deionised water with no flow in a notional 10μm aperture fracture and no mechanical coupling at 20 °C, 60 °C and 120 °C.
    - Construct a simple 0D/1D representation of the fracture with a constant starting aperture up to the start of the first reversal (1292 hr) attempting to reproduce the major features of the experimental results.
- **Step 1**: Attempt to model the novaculite case up to the end of the reversal of flow (isothermal) in 2D (if possible) using fully coupled formulations. Teams to attempt to understand the relative impacts of chemical dissolution versus early mechanical evolution. Teams should also attempt to understand the consequences of coarse or fine representations of the fracture surface.
- **Step 2**: Model the novaculite case up to the end of the experiment. Impacts of temperature are clearly significant in this phase (non-isothermal). Again sensitivities to chemical and mechanical processes are of interest.
- **Step 3**: Basic benchmarking – Granite
    - Represent simple batch experiments of granite dissolution in deionised water with no flow in a notional 10μm aperture fracture and no mechanical coupling at 25 °C and 90 °C. Compare dissolution rates, solubilities and pH between teams. Teams to optionally look at the impacts of different surface area models as dissolution progresses.
- **Step 4**: Attempt to model the granite case during the initial isothermal (20/25°C) period. Teams to attempt to understand the relative impacts of chemical dissolution versus early mechanical evolution.
- **Step 5**: Attempt to model the granite case over the full experimental period (20/25°C and 90 °C).
- **Step 6**: Application (Optional). The purpose of this exercise is to test the degree of difference between long-term predictions using well-constrained models calibrated against short-term data. The specification for this work has yet to be defined.

The proposed schedule for the project is given in Figure 3.5.

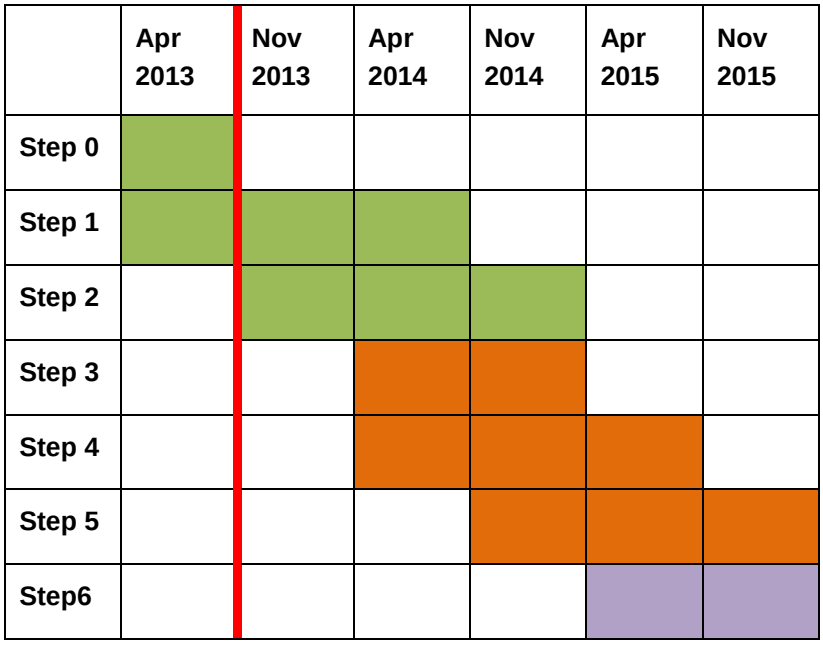

Figure 3.5. Task C1 schedule (from Bond, 2013b). Green cells indicate novaculite steps while the orange cells indicate granite steps. The end of April 2013 is marked with a red line.

It should be noted that the effective start to Task C1 occurred relatively late due to the scope of works not being defined until November 2012. However, the task is under different management and is now making progress. As such Task C1 is a little behind Task A in terms of progress.

3.2 Approach to Task C1

In order to address the requirements of the Task, we decided to adopt two complementary approaches. The first approach would take a detailed view of the fracture topography data, attempting to use a high resolution approach to represent the system. This approach would naturally lead on to Step 1 and was considered to provide the best chance of a good representation of the whole evolution of the novaculite experiment.

The second approach was to take a homogenised view of the fracture, attempting to reproduce the evolution of the system using as low a resolution as possible. The benefit of such an approach would come later in the task, noting that the granite experiment has no detailed information concerning fracture topography, and as such, some form of simplified method would be required.

In terms of the complexity of each approach, one might reasonably expect that the higher resolution approach to be problematic due to the pure size of the problem – over 1.6 million datum points per fracture surface are available (see Section 3.1.2). In contrast, a more homogenised approach is likely to require more sophisticated process models in order to represent the fracture topography through different means.

To play to the respective strengths of the AMEC team, it was decided that the University of Edinburgh would focus on the higher resolution approach using OpenGeoSys (OGS - Appendix A), while Quintessa addressed the homogenised approach using QPAC (Appendix B).

3.3 Step 0

3.3.1 Geochemical Model

3.3.1.1 Quartz Solubility Model

Yasuhara et al. (2006) suggest that in their experiment dissolved silica concentrations were lower than those associated with quartz solubility. Therefore it is very unlikely that there was precipitation of less stable SiO_2 polymorphs, such as chalcedony, or amorphous silica. Hence the only solid phase that needs to be included in the modelling is quartz. The experiment included deionised water and, given the lack of elevated pH conditions, it is expected that dissolved silica was present as $SiO_{2(aq)}$ only. Therefore, quartz dissolution is given by:

$$SiO_{2(s)} \rightarrow SiO_{2(aq)} \quad (16)$$

The equilibrium constant for this reaction (K) is given by:

$$K = a_{SiO_{2(aq)}}/a_{SiO_{2(s)}} \quad (17)$$

Where *a* is activity, which for a pure solid phase is taken to be 1. Therefore, the solubility of quartz (equilibrium activity of $SiO_{2(aq)}$) is equal to the K value for reaction (16):

$$K = a_{SiO_{2(aq)}} \quad (18)$$

The value of K for reaction 16 can be calculated from the Gibbs free energy of reaction (ΔG_r) under given T and P conditions given that:

$$\Delta G_r = -RT\ ln\ K \quad (19)$$

Where R is the gas constant (J/mol K) and T is temperature (K).

In the experiments there is variation in T and P, but for mineral-fluid interactions, T tends to predominate, unless the P difference is very large or the solid phase has a large compressibility. The approach typically taken in geochemical models of mineral-fluid equilibria is that total pressure is equal to 1 bar at T < 100 °C and that if T > 100°C, pressure is equal to the saturation vapour pressure for pure water. This approach has been widely adopted (in codes such as Geochemist's Workbench, Bethke, 2008).

However, the models described here require a consideration of P effects and hence, log *K* values have been calculated using 'SUPCRT92' (Johnson et al., 1992) and its database 'dprons96.dat'. SUPCRT92 is a software package for calculating the standard molal thermodynamic properties of minerals, gases, aqueous species, and reactions from 1 to

5000 bar and 0 to 1000 °C. Calculated log *K* values for reaction 1 under some of the T and P conditions of interest are summarised in Table 3.1.

Table 3.1. Calculated Log K values for quartz solubility under low T and P conditions (Equations 16-19)

T	P	log K
(°C)	(bar)	(-)
20	13.8	-4.099
40	13.8	-3.74
80	13.8	-3.257
120	13.8	-2.92

A plot of calculated log $a_{SiO2(aq)}$ values for quartz-water equilibrium as a function of P (under relevant T conditions) is given in Figure 3.6.

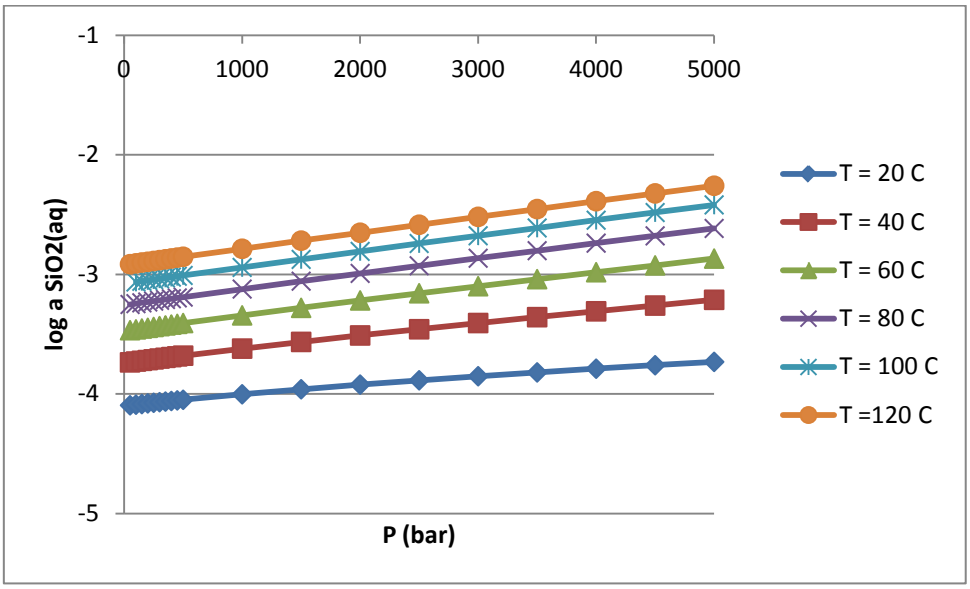

Figure 3.6. Calculated log *a* $SiO_{2(aq)}$ values corresponding to equilibrium solubility of quartz as a function of P under T conditions of the experiment by Yasuhara et al. (2006).

The log K values in Table 3.1 are equal to the activity of $SiO_{2(aq)}$ associated with the equilibrium solubility of quartz. In infinitely dilute solutions, solute concentration (molal units) is equal to activity, i.e., the mean activity coefficient (γ) used to convert between solute activity and concentration has a value of 1. In solutions other than pure water, interactions between ions means that activity decreases as a function of increasing ionic strength (by Coulomb's law, electrostatic forces vary inversely with the square of distance of ion separation). However, in this model we only have one neutral, nonpolar, aqueous species. Activity coefficients for species such as $SiO_{2(aq)}$ generally obey the Setchenow equation up to quite high ionic strength (I) values[1]. The Setchenow equation is

[1] Ion strength of a solution (I) = $\sum_i m_i z_i^2$, where m_i is species molality and z is charge.

$$log\ \gamma_i = K_i I \quad (20)$$

where K_i is a constant, ranging from 0.02 to 0.23 at 25 °C (Langmuir, 1997). In the 'B-dot' extended Deybe-Hückel model used to calculate mean activity coefficients in Geochemist's Workbench (Bethke, 2008), the activity coefficients of electrically neutral, non-polar species such as $SiO_{2(aq)}$ are calculated from ionic strength using an empirical relationship:

$$log\ \gamma_0 = aI + bI^2 + cI^3 \quad (21)$$

where γ_0 is the activity coefficient of a neutral, nonpolar species and a, b, and c are polynomial coefficients that vary with temperature (Figure 3.7).

However, as Yasuhara et al. (2006) used deionised water in their experiment the solution should have a negligible ionic strength. Given the plot of activity coefficients as a function of I in Figure 3.6, the following approximation can be used without the introduction of significant error:

$$a_{SiO_{2(aq)}} = \gamma m_{SiO_{2(aq)}} \approx m_{SiO_{2(aq)}} \quad (22)$$

where m is solute concentration (molal).

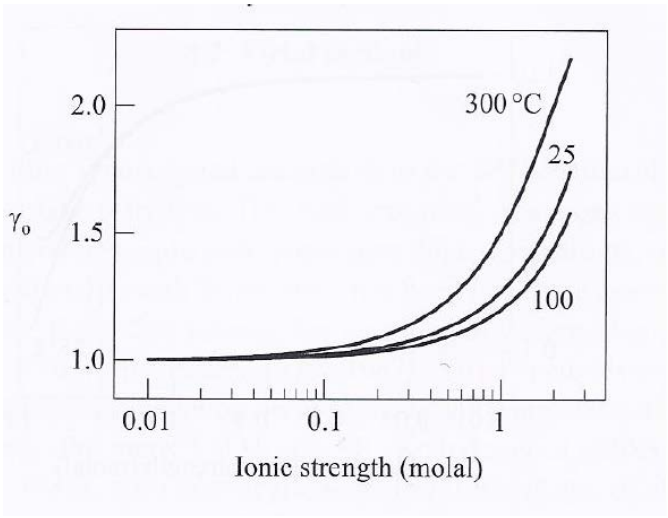

Figure 3.7. Activity coefficients (γ_0) for neutral, nonpolar species as a function of ionic strength (molal) at 25 °C, 100 °C and 300 °C (from Bethke, 2008)

3.3.1.2 Calculated vs. Measured Data on Quartz Solubility

As summarised by Gunnarsson and Anórsson (2000), studies of quartz solubility in water along the liquid-vapour curve are many and, in the temperature range 100° to 250° C, the results show good conformity with few exceptions, but at temperatures below 100°C and above 250°C considerable discrepancy exists between reported results, possibly due to equilibrium not being attained due to slow reaction rates. As discussed by Gunnarsson and Anórsson (2000), Rimstidt (1997) presents quartz solubility from 21° to 96 °C which suggests that quartz has a higher solubility than previously reported. Using the SUPCRT92

database, the calculated log K value for the quartz dissolution reaction given in Equation (16) at 25 °C, 1 bar is -4. This is the value included in the EQ3/6 and Geochemist's Workbench databases (Wolery, 1992; Bethke, 2008). The mineral data in SUPCRT92 are largely from Helgeson et al. (1978). In contrast, the log K value for this reaction in the recent 'thermoddem' geochemical database developed by BRGM (2011), is -3.74. There is therefore some variation in the quartz solubility values adopted in geochemical databases for low T and P conditions. The difference of 0.26 log units, corresponds to a difference in $SiO_{2(aq)}$ concentration (according to Equation 22) of 8.2 10^{-5} molal, or 4.93 mg/kg. Of course, there is also some variation and uncertainty associated with measured solubility data under higher T and P conditions (Figure 3.8).

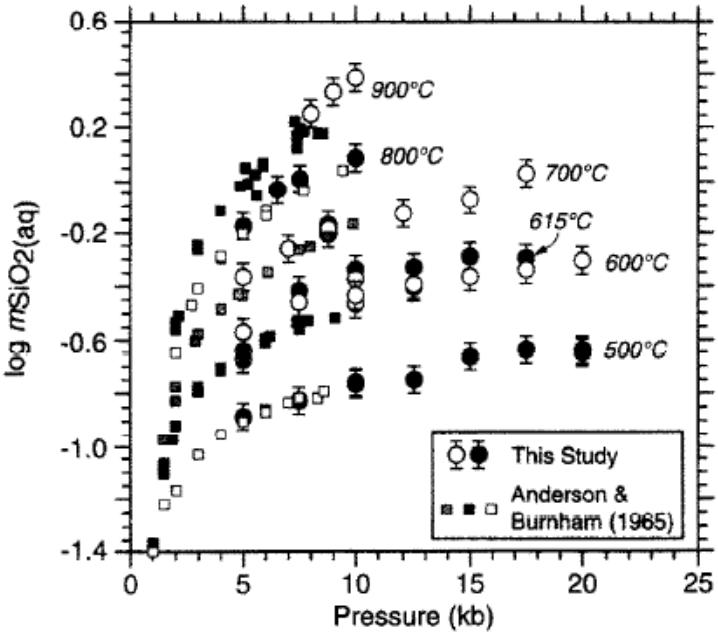

Figure 3.8. Example of range in measured quartz solubilities under elevated T and P conditions (from Manning, 1994).

3.3.1.3 Quartz Dissolution Kinetics

With regard to quartz dissolution rates, a range of data have been published for different pressure, temperature and chemical conditions. Palandra and Kharaka (2004) review mineral dissolution rate data and recommend data from Tester et al. (1994) for quartz dissolution in pure water under a wide range of T conditions.

The rate of dissolution of a solid as a function of temperature (under far-from-equilibrium conditions) can be expressed as:

$$\frac{dm}{dt} = k = -Ae^{-E/RT} \quad (23)$$

where the rate $dm\ /\ dt$ (or k) is in mol/m^2/s, A is the Arrhenius pre-exponential factor (mol/m^2/s), E is activation energy (J/mol), T is temperature (K) and R is the gas constant.

On the basis of the data given by Tester et al. (1994), Palandra and Kharaki (2004) give a value of 276 mol/m^2/s for A and an activation energy (E) of 9.01 10^4 J/mol. Values of quartz dissolution rate calculated using these data are given in Table 3.2. Quite often, mineral dissolution rates are catalysed by H^+ or OH^- (or other solutes) and reaction rates include terms to account for such behaviour. However, for the conditions of the experiments reported by Yasuhara et al. (2006), a pH neutral rate expression can be adopted. A commonly adopted approach is to have dissolution rate that is reduced as equilibrium conditions are approached, according to Transition State Theory (TST):

$$\frac{dS}{dt} = kA(S)\left(1 - \frac{Q}{K}\right) \tag{24}$$

where S is the quantity of a solid of interest (mol), t is time (s), $A(S)$ is the mineral reactive surface area (m^2), Q is the ion activity product for the solid of interest (dimensionless) and K is the equilibrium constant for mineral dissolution (dimensionless).

The surface area term $A(S)$ with vary as a function of mineral abundance and intrinsic reactive surface area. Mineral dissolution rates are often measured on samples for which surface area is either measured, (using electron microscopy, atomic force microscopy or more commonly, gas adsorption i.e. 'BET' techniques) or they may be estimated using geometric assumptions. For example, equant grains of a mineral can be taken to have a surface area that is similar to spheres of that mineral. If the density of the mineral is known, the surface area for a given mass of material assuming spherical grain morphology may be calculated. In the Yasuhara et al. (2006) experiments, the evolving surface area of the fracture surface and its asperities may need to be taken into consideration, rather than grain morphology used for porous media calculations.

Table 3.2. Reaction rates for quartz dissolution under neutral pH conditions under T conditions associated with the experiments described by Yasuhara et al. (2006)

T (°C)	rate (mol/m^2/s)
20	2.437E-14
40	2.583E-13
80	1.301E-11
120	2.953E-10

3.3.2 Geochemical Benchmark

The geochemical benchmark, considering dissolution of quartz into a 10 μm constant aperture fracture, with no flow or mechanical effects, was implemented in both OpenGeoSys and QPAC, giving functionally identical answers. In addition to the three temperatures, consideration of the effects of different surface area roughness factors was also included to cover the range of potential uncertainty, as discussed in the previous section.

The comparison of dissolved concentrations (Figure 3.9) and dissolution rates (Figure 3.10) illustrates the very strong effect of temperature on the dissolution of quartz in terms of both saturated concentrations and rate of dissolution. The impact of surface roughness (implemented here by scaling the fracture areas) is comparatively small, but remains significant in terms of rates of dissolution. This emphasises the need for consistency in dissolution rates and the assumed effective surface area.

The results also illustrate that as a process, simple silicate dissolution is unlikely to be significant at the lower temperature range, simply because the kinetic rates are so slow, however it may be significant at higher temperatures. It is interesting to note that in comparison with the net dissolution rates required by Yasuhara et al. (2006) (i.e. the amounts of Si going into solution by **all** processes – see Figure 3.10), the dissolution rates predicted are considerably lower; by at least an order of magnitude lower, tending to confirm that the aqueous geochemistry may be a second order process.

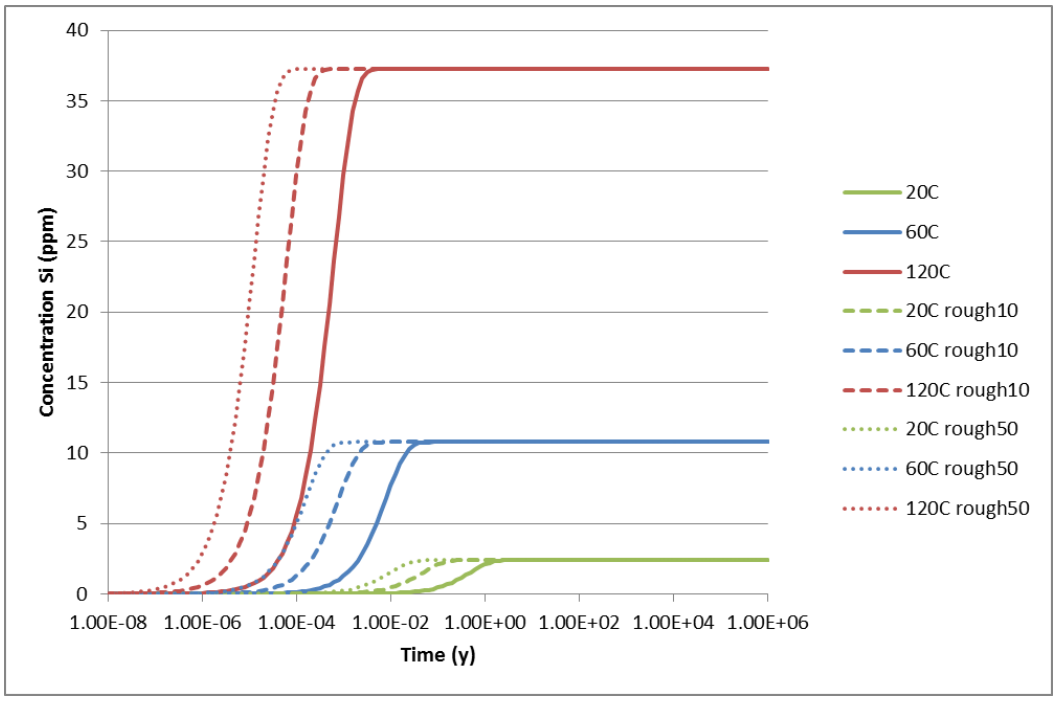

Figure 3.9. Dissolved Si concentrations with time for the geochemical benchmark at the prescribed three different temperatures and for three fracture surface area roughness factors.

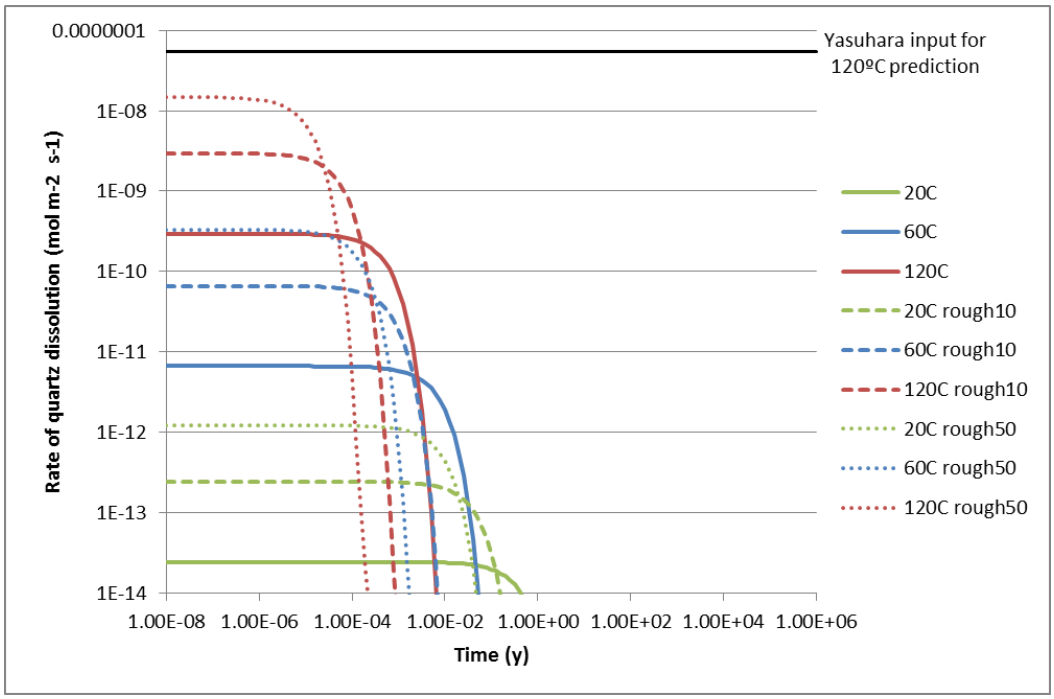

Figure 3.10. Dissolution rates of quartz with time for the geochemical benchmark at the prescribed three different temperatures and for different fracture surface area roughness factors. Net (all processes) dissolution rate for 120°C from Yasuhara et al. (2006) also shown.

3.3.3 High Resolution Approach for Step 0

3.3.3.1 Approach

University of Edinburgh investigated the novaculite data from the perspective of the detail available through the high resolution topography of the fracture surfaces. The approach comprised two components:

1) A simplified "1D" type equivalent parameter model of the fracture during closure was developed to enable assessment of the impact of changing the fracture resolution. This allowed the identification of the most efficient resolution of the fracture surface data.

2) OpenGeoSys was modified to allow a numerical solution of the hydraulic mass balance equations coupled with an analytical solution of the mechanical and chemical behaviour to allow a coupled representation of the fracture system in 2D. As part of this exercise, different pressure solution and chemical solution models are considered.

3.3.3.2 Equivalent Parameter Model

As noted in Section 3.1.2 an extremely detailed data set for the fracture surface profile is available for both upper and lower surfaces. There are 3,271,640 measurements which translate to 1,635,820 points of fracture aperture. Two known issues need to be dealt with regarding this data set to enable calculation of the flow properties:

1) The resolution of these values needs to be reduced in order to cope computationally with the data on a normal PC.

2) There is a datum mismatch in that the lower surface projects through the upper surface in a number of places.

The resolution of the data set was reduced by selecting point by point information from the fracture profile at larger resolutions than the data set. Data were selected at several different resolutions, and the resulting fracture profile data sets were simulated in closure using a simplified closure model. The aim of this approach was to enable as large a resolution as possible of the data set to be simulated without losing key attributes of the behaviour of the fracture.

At this stage it was assumed that the lower or upper fracture surface profile has a complete statistical probability distribution of the fracture aperture heights, and that the heights are distributed randomly. This means that a minimal x,y mismatch in the data sets is considered not to be significant in terms of the overall behaviour of the fracture surface. Channel geometries are typically characterised at a larger scale then aperture resolution; Walsh et al. (2008), and references therein discuss the concept of aperture mismatch. We can safely assume that the scale of the experimental mismatch of the fracture surfaces is significantly less than the mismatch leading to the development of the channelling within the fracture surface. It is also the case that the topography data do not cover the complete surface of the fracture (49.5 x 88.9 mm profiled versus 50.0×89.5 mm in the experiment) which gives rise to the possibility of lateral mismatches between the two surfaces as measured. Both of these are aspects which may be chosen for further investigation.

Method applied to reduce the resolution of fracture data

The fracture data are provided in column, row and height format that provides regular gridded data. The FE code OpenGeoSys requires mesh elements to be able to discretise an area and an initial decision was taken to use quad elements in line with the geometry of the data provided.

Code has been written which extracts node corners from the data set and then provides the middle point of the defined quad. This is then used to provide OpenGeoSys with mesh data, element data, and other reference geometrical data as well as aperture and permeability data.

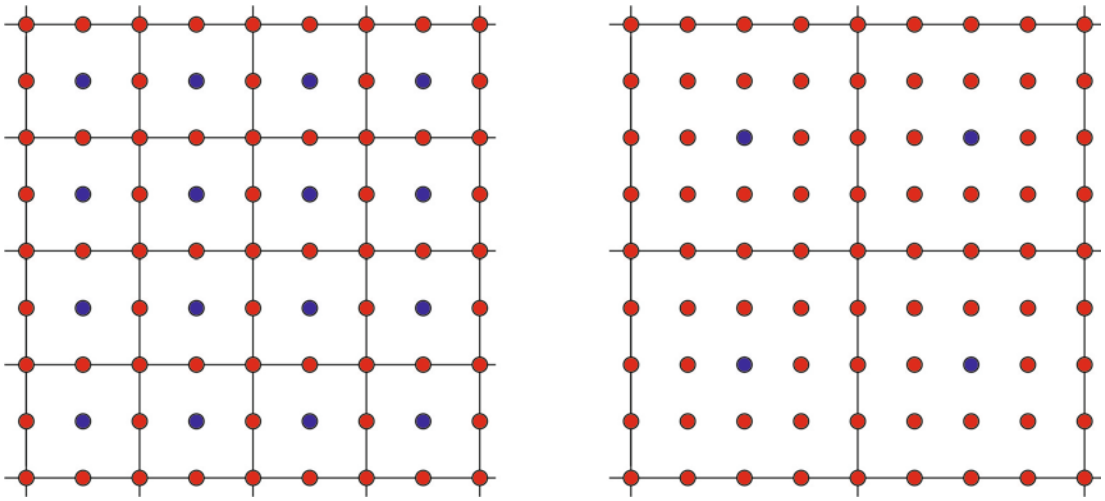

Figure 3.11. Reduction of 1.6 M data points to usable meshes.

The red points in Figure 3.11 represent locations where topography was measured. The lines are the edges of the quads used in the finite element calculations; the blue points represent the middle of the elements, topography was also measured at these points. The resolution of sampling was measured by the number of points skipped in the x and y direction. To the left of Figure 3.11 the resolution of sampling was 2, to the right the resolution was 4.

Different methods were considered to assign the element value including

1) Unfiltered selection, i.e. only the centre point of the element was used

2) Average value, the average of all points contained within the element

3) Distance weighted value, distance weighted values for the element.

For the simulations presented, only method (1) above has been evaluated. Both option (2) and (3) were considered to remove the extremes of the data set and lead to an artificial smoothing, and hence were not applied for the time being. These alternative methods can will be investigated at a later date if necessary, along with the possibility of lateral and rotational mismatches.

3.3.3.3 Methods Applied to Address Fracture Apertures

There are a number of key measurements in Yasuhara et al. (2006) which allow the calibration of the apertures from the data sets. These include

1) matching average hydraulic apertures by comparing the calculated apertures with the measured flow rates and pressure differentials
2) matching the calculated change in contact area with time with a dissolution model, and with direct observation results
3) matching the calculated rate of change of aperture with the observed rate of change in aperture.

The fracture profile is assumed to define the aperture distribution (see discussion above on mismatch). The hydraulic properties of the fracture can be evaluated from the aperture distribution as discussed below. The change in the hydraulic properties of the fracture with closure or opening of the fracture aperture can be calculated by subtracting (closure) or adding (opening) a minimal value to the aperture profile.

3.3.3.4 Equivalent Parameter Model

For the evaluation of the resolution of the fracture data, we investigate a change in aperture as caused by pressure solution of the contact area. This was assumed to be driven by the removal of the quartz by solution. An equivalent parameter model was developed whereby the average fracture aperture as a function of the time dependent removal of SiO_2. The measured concentration of silica in the fracture fluid provides an estimate of discrete aperture changes and the average channel aperture was related to the hydraulic aperture. This was then used as an initial simple model to test assumptions of the initial aperture distribution.

From Yasuhara et al. (2006) the fracture contact area is estimated from the rate of change of the aperture as a result of silica dissolution. The rate of change of the aperture is given as

$$\frac{db}{dt} = \frac{Q}{R_c}\frac{C_{SiO_2}}{A_f \rho_g} \tag{25}$$

Where A_f is the total fracture area $A_f = 8.95 \times 10^{-3} m^2$, ρ_g is the grain density of quartz (2650 kg/m^3), Q is the flow rate in m^3/s and C_{SiO_2} is the concentration of silica (kg/m^3).

Integrating (25) we can write

$$\Delta b = \frac{Q C_{SiO_2}}{R_c A_f \rho_q} \Delta t \tag{26}$$

Assuming that each measurement point of the aperture represents an equal surface area, the contact area is defined as

$$R_c = \frac{\sum_1^n 1(b_t<0)}{\mathrm{n}} \tag{27}$$

The fracture aperture b_t is given by the subtraction of the lower surface data from the upper surface data set provided by Yasuhara. On subtraction of one data set from the other circa 40% of the surfaces are seen to intersect, suggesting an error with the reference datum. An offset o_t is therefore applied to the data set such that

$$b_t = S_u - S_l + o_t \tag{28}$$

$$o_t = o_{t=0} - \sum_{t=0}^{t=n} \Delta b \tag{29}$$

The value $o_{t=0}$ is set by matching the experimental data. Here the value S_u is the elevation of the upper fracture surface corresponding to the same x,y coordinates of the elevation of the lower fracture surface S_l. A time subscript t is used.

R_c in (27) is evaluated from b in (28), and then Δb for a time increment Δt is calculated in (26). This sequence of equations, (26), (27), (28) and so on is repeated until the sum of the time increments equals the desired time interval.

The equivalent permeability k_{eq} of the open apertures is given by the geometric mean of the open apertures of the fracture at any particular time using the Boussinesq relationship (Boussinesq, 1868), that is

$$k_p = \frac{b_t^2}{12} \tag{30}$$

$$k_{eq} = 10^{\frac{1}{n}\sum_1^n \log_{10} k_p} \tag{31}$$

In this instance the geometric mean is considered to provide a better average of the permeability of a spatially heterogeneous field of values than the average or harmonic means. However it is recognised that this assumption is very dependent on the local aperture structure and this assumption should be revisited in further work. To convert this to the experimentally approximated hydraulic aperture b_h we need to take into account the closed areas of the fracture, therefore

$$b_{eq} = \sqrt{12 k_{eq}} \tag{32}$$

$$b_h = \sqrt[3]{(1 - Rc) b_{eq}^3} \tag{33}$$

And the corresponding measured fracture permeability k_f will be

$$k_f = \frac{b_h^2}{12} \tag{34}$$

3.3.3.5 Results from initial model

Using the methodology above the resolution on the fracture surface was repeatedly reduced to find the largest sampling distance possible whilst still maintaining a satisfactory representation of the behaviour of the fracture. There are aspects of the model which could have been more rigorously developed, however the aim of providing information for a fully discretised finite element model was satisfied.

It was found that a value of $o_{t=0}$ of 0.0175 mm (see equation 29) fits the experimental results appropriately.

For the first 121 hours, where the flow rate was 1 ml / minute, it appears that the dominant process of solution was that of removal of the asperities.

From 121 to 380 hours there appears to be a clear increase in the amount of silicate removed by a process other than pressure solution. This is suggested by the fact that the modelled curve lies underneath the measured hydraulic aperture curve (Figure 3.12). That means that more silica is being transported out of the fracture than can be accounted for by pressure solution alone.

Both Figure 3.13 and Figure 3.14 can be shown to match relatively closely the experimental results and the range expected. Figure 3.15 describes how the results vary with different resolutions of the fracture surface. Sampling at a distance of 0.8 mm still provides a reasonable representation of the characteristics of the surface, whilst reducing the data set from 1.6M points to 6326 points. It can be seen that at 1.6 mm resolution the assumptions used in the model are not providing such a good representation of the fracture surface, and that more model refinement would be necessary should this modelling approach be further pursued.

It should be noted that this approach does not consider mechanical coupling between elements, i.e. other than the general redistribution of stress due to increasing contact points, the effects of local 'bridging' are neglected. This is an area that is likely to require further attention in later steps, especially with the inclusion of temperature related effects.

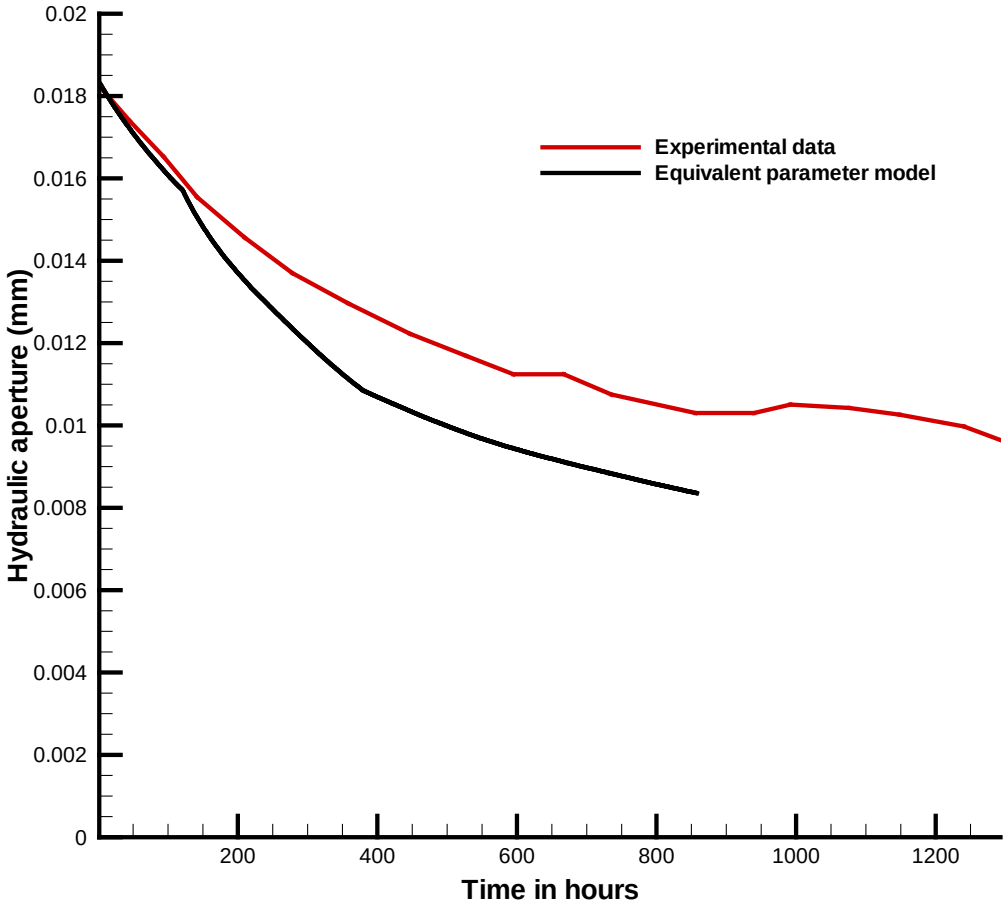

Figure 3.12 Comparison of experimentally observed hydraulic aperture and the equivalent parameter model prediction.

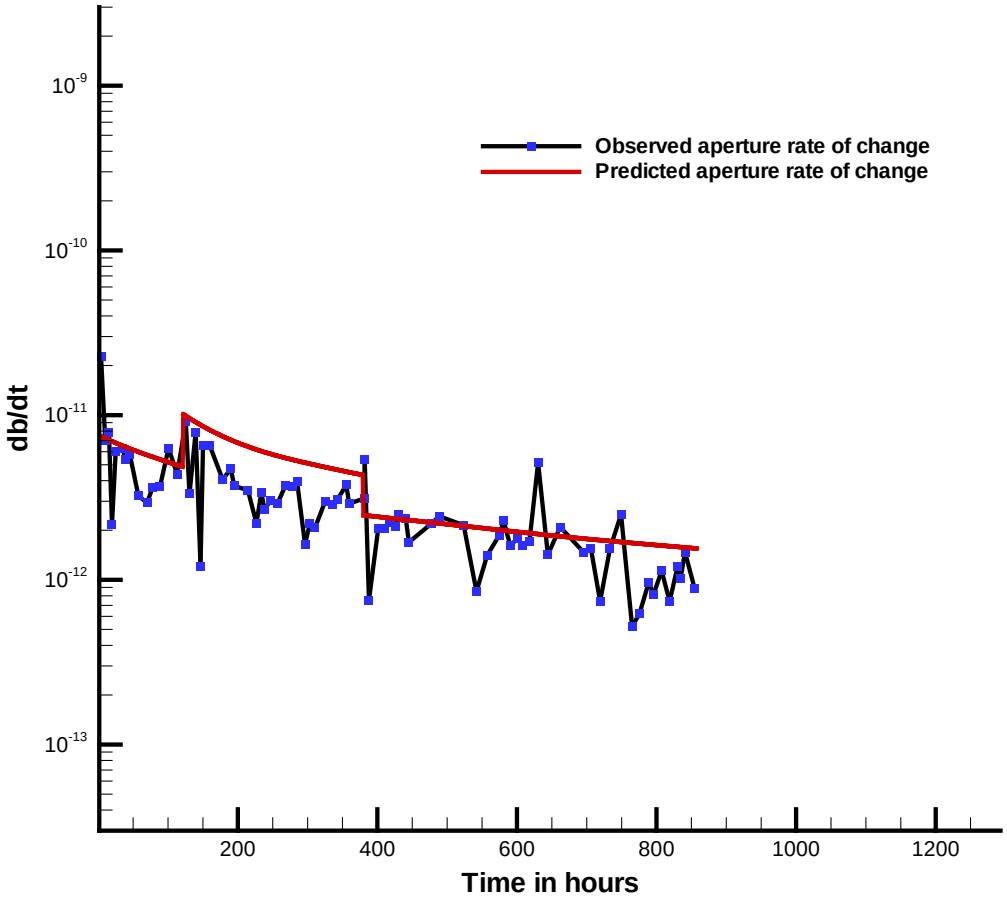

Figure 3.13 Comparison of the rate of change of aperture for the asperity solution model and observed data

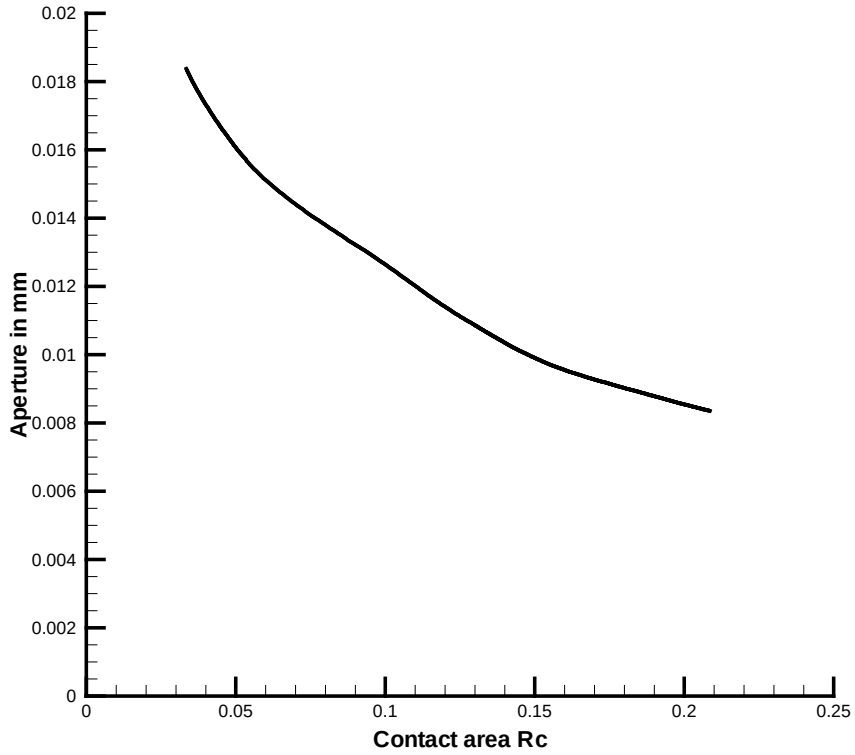

Figure 3.14 Calculated contact area

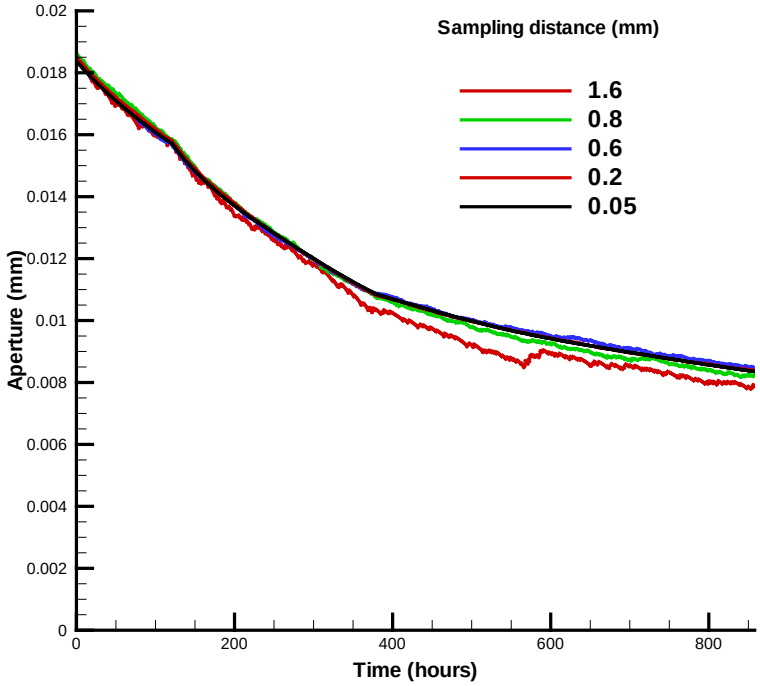

Figure 3.15 Comparison of effect of different sampling distances on the quality of model results.

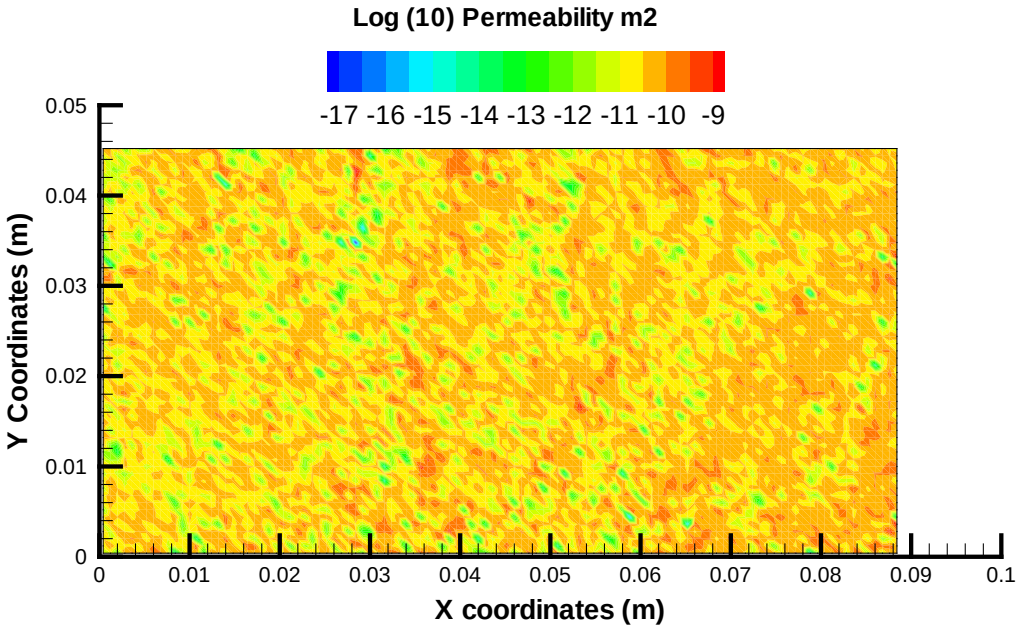

Figure 3.16 Permeability distribution of the fracture surface for the 0.8mm resolution chosen for the development of the FE modelling.

3.3.3.6 2D coupled representation of the fracture

Following the discussion in the previous section, the permeability of each element of the fracture surface, assuming laminar flow, is given by

$$k_{\alpha\beta}^{b} = \frac{b^2}{12} \tag{35}$$

Where b is the aperture. Although this expression overestimates the hydraulic conductivity of rough fractures to some degree, it provides a good approximation of the corresponding permeability distribution given a particular aperture distribution. The fracture plane is discretized into individual elements, and an aperture is mapped to each element (Figure 3.17)

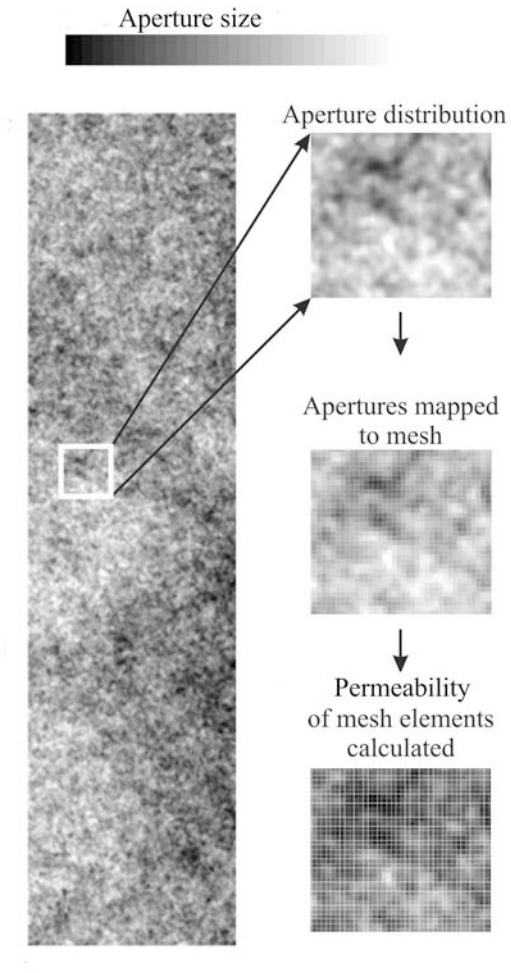

Figure 3.17 Aperture distribution mapped to fracture plane.

Pressure and chemical solution models

Three types of solution of quartz causing changes to the fracture surface are allowed:

1) Pressure solution at the contacts
2) Dissolution at
   a) the contacts
   b) the channel walls

This leads to a natural division between ‘channel’ elements (where flow occurs) and ‘contact’ elements (where the fracture is assumed to be fully in contact), the transition between one and the other being dependent on the channel aperture. For the current case this threshold aperture is set at 11 nm. We note in Yasuhara et al. (2006) the limit was set at the slightly smaller value of 4 nm. This is set such that the permeability of the element with an aperture of this width is effectively zero, but does still allow solution using the finite element approach without having to re-grid the area and exclude inactive flow elements. For the initial models

pressure solution and dissolution in the channel walls will be taken into account. Aqueous dissolution at the contacts will not be taken into account.

Yasuhara et al. (2006) suggest a linear relationship between aperture and stress, for the 80% of closure they attribute to pressure solution. Ignoring temperature effects on pressure solution for an initial approximation suggests a formulation at the element level such that

$$\sigma_c = \frac{\sigma_n}{CA} \tag{36}$$

$$\frac{\partial b}{\partial t} = -a(\sigma_c - u)^c \tag{37}$$

Where b is the aperture, σ_c is the contact stress, a and c are fitting constants, for the linear case c=1. CA is the contact area as a function of the fracture expressed as a value from >0 to 1, whereby 1 means all the fracture is contacting. This model is introduced into OpenGeoSys where c = 1 and the constant a is required.

The work of Gratier et al. (2009) and references therein suggest that the constant a can be expressed in the form

$$a = 2\alpha_p k_+ V_s \tag{38}$$

Where V_s is the molar volume of quartz, given at circa $2.264 \times 10^{-5} mol/m^3$., and k_+ is the kinetics constant for dissolution or precipitation reaction $(mol\, m^{-2}\, s^{-1})$. α_p is a fitting constant (m/Pa), and the 2 is introduced to allow two sides of the fracture to dissolve.

$$\Delta b = -2\alpha_p k_+ V_s (\sigma_c - u)^c \Delta t \tag{39}$$

Other pressure solution models have been proposed (e.g. Gratier et al., 2009), and these will be investigated as the project progresses.

For chemical dissolution, the general model proposed in Section 3.3.1 was adopted for the OpenGeoSys implementation. For this initial evaluation we assume that $Q \approx 0$, i.e. there is no diffusion limitation on the solubility of the quartz.

$$\frac{\partial S}{\partial t} = A_e k_+ \tag{40}$$

Where the term $A(S) = A_e$ the planar area of the element. Converting this equation into a rate of closure requires

$$\frac{\partial b}{\partial t} = 2A_e k_+ \frac{V_s}{A_e} \tag{41}$$

The value 2 is again introduced to allow dissolution from both sides of the fracture.

Equation (41) can be seen to provide a 'velocity of closure' in the units are ms^{-1}. A user defined variable is introduced into OpenGeoSys such that

$$\Delta b = a_c \Delta t \quad (42)$$

Where

$$a_c = 2k_+ V_s \alpha_c \quad (43)$$

In that α_c is a fitting constant.

$$\Delta b = 2k_+ V_s \alpha_c \Delta t \quad (44)$$

This provides a simplified dissolution model that can be applied in 2D. The implementation of these process models in OpenGeoSys is discussed in Appendix A.

2D Model Results

The model was run iteratively, adjusting the calibration of the fitting parameters α_p and α_c to best fit against the available data. Models were run with and without the aqueous dissolution component in order to understand the potential significance of each process, noting that the expectation is that chemical dissolution will be of lower significance at the early stages of the experiment.

The best fit for the pressure solution-only model is shown in Figure 3.18.

Looking at the first part of this curve it is possible to speculate that the initial part should be steeper and then the gradient should become shallower. This would suggest more pressure solution to start with and then less pressure solution as the aperture reduces, should the chemical dissolution effect be minor. Such behaviour will be explored through the non-linear pressure model, described above, during the next phase of work. The corresponding fit to the geochemical data is given below in Figure 3.19 and the normalised differential pressure response as defined by Yasuhara et al. (2006) is shown in Figure 3.20. The fit to the geochemical data is over-estimated, and consistent with that, there is a tendency to over-predict aperture closure after the flow shutdown (approximately 858 to 930 hours).

The best fit for a combined model was achieved by decreasing the degree of pressure solution and then allowing the open portions of the fracture to develop by dissolution led to the fit shown Figure 3.21, Figure 3.22 and Figure 3.23. Using this model, the aperture and normalised pressure distribution are clearly improved and the amount of Si entering solution has been reduced, producing a generally good fit to the observations.

It is also clear that for both models, the aperture increase shown in the data during this flow-shutdown period is not reflected in the model, indeed there is no process implemented in the current models to create this effect, should it be considered significant.

The fitting parameters for the above models are given in Table 3.3.

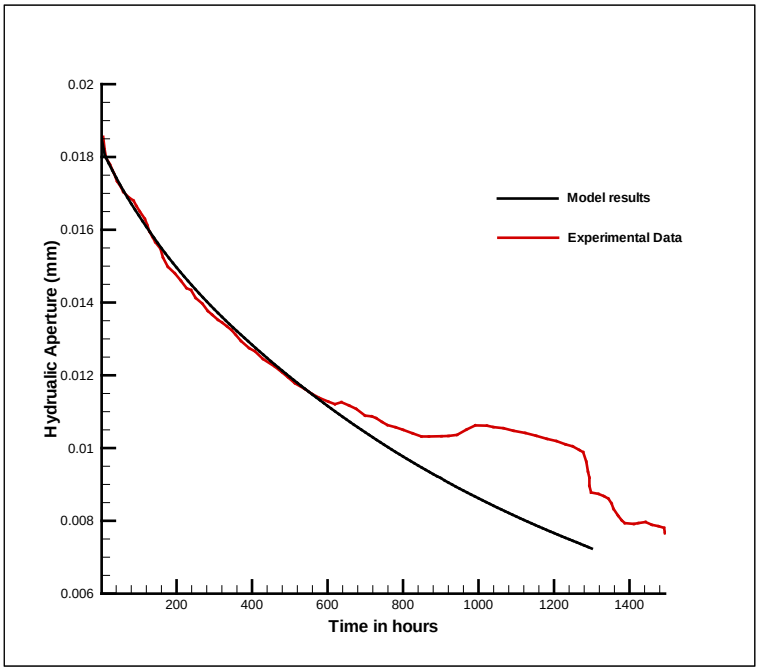

Figure 3.18. Hydraulic aperture closure, pressure solution only model.$\alpha_p = 0.177$. Larger values of alpha will increase rate pressure solution and the gradient of the black curve, and lower values will decrease the gradient.

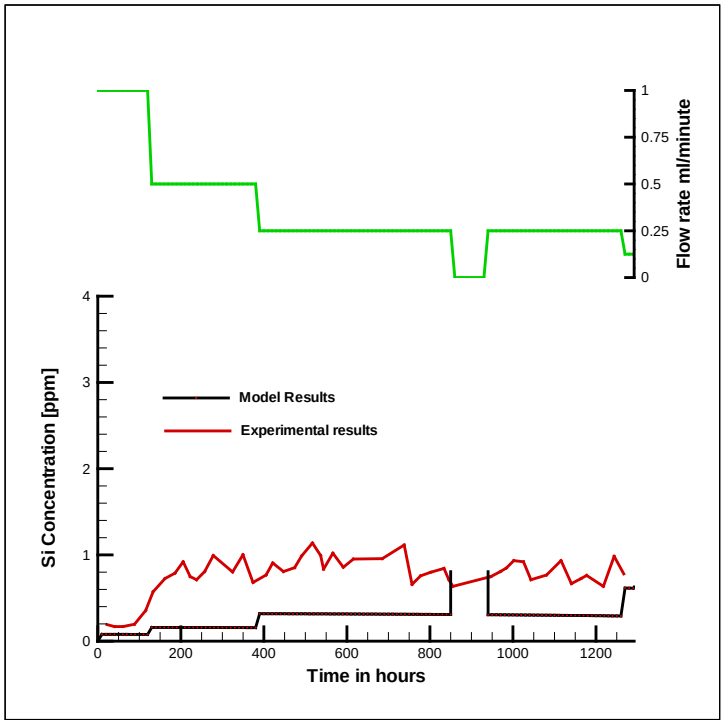

Figure 3.19 Si Concentration for pressure solution only model. The raised concentration during the no flow period is a numerical artefact to be removed in further model development.

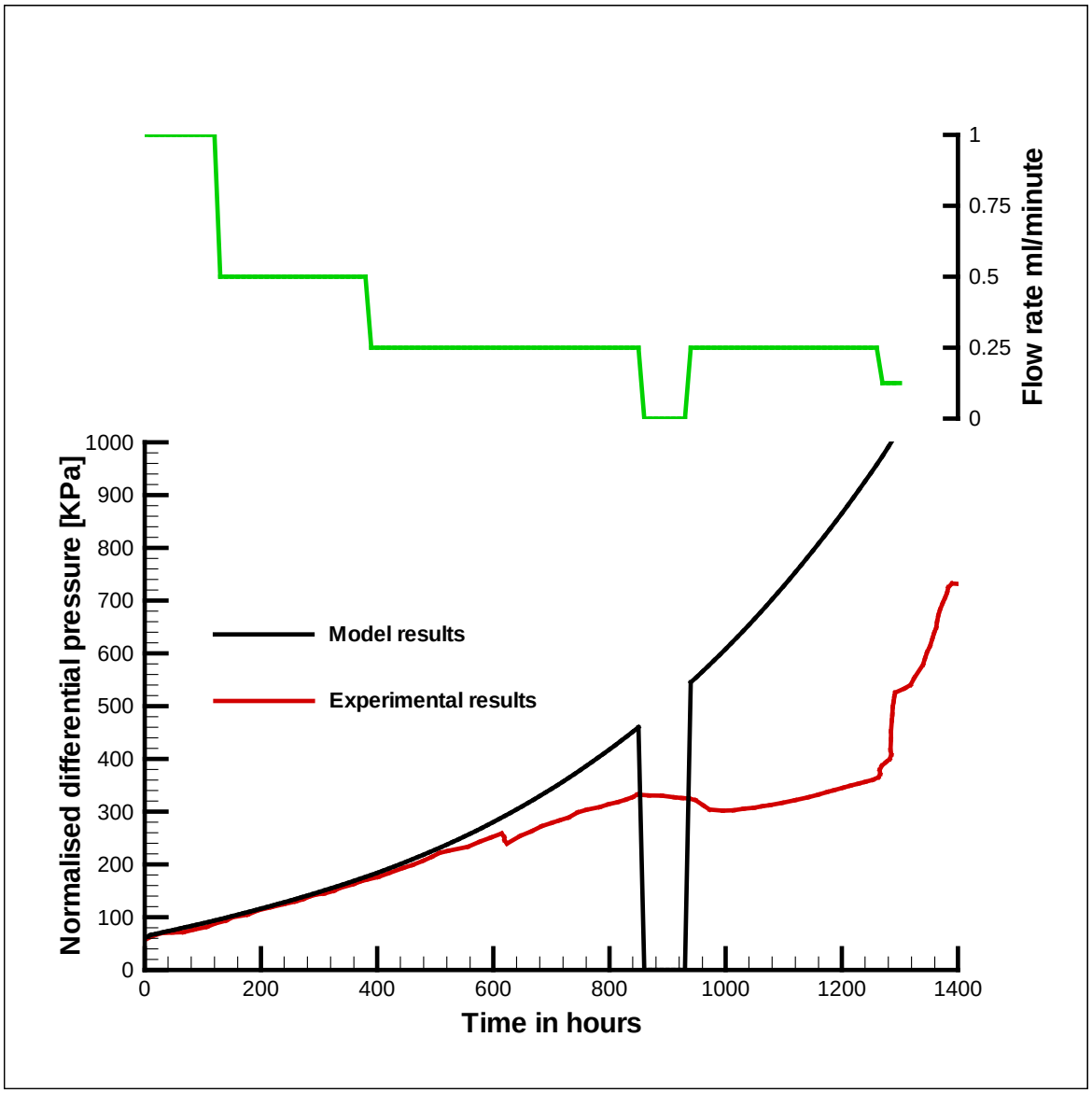

Figure 3.20 Normalised differential pressure for pressure solution only model.

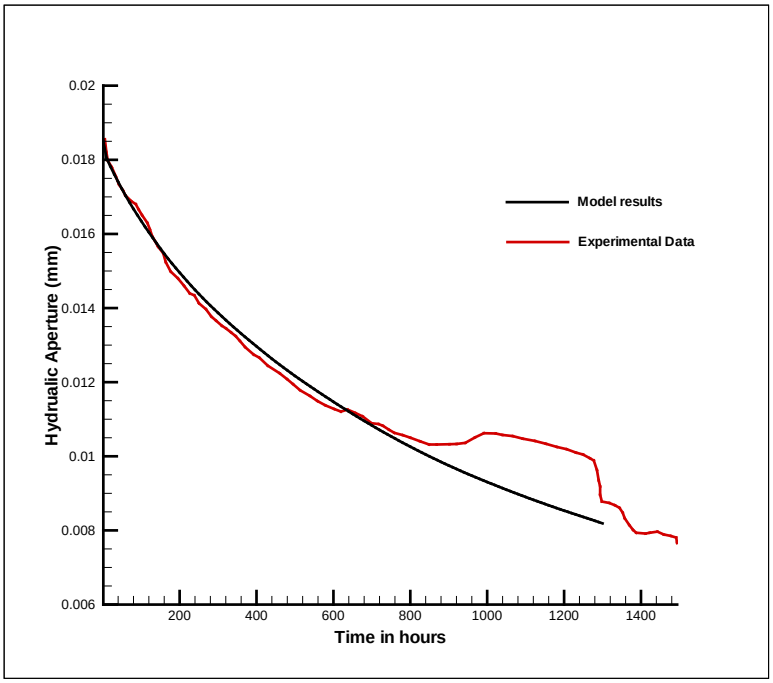

Figure 3.21 Hydraulic aperture closure of pressure solution and chemical etching model, α_p=0.212, α_c=7.79E5

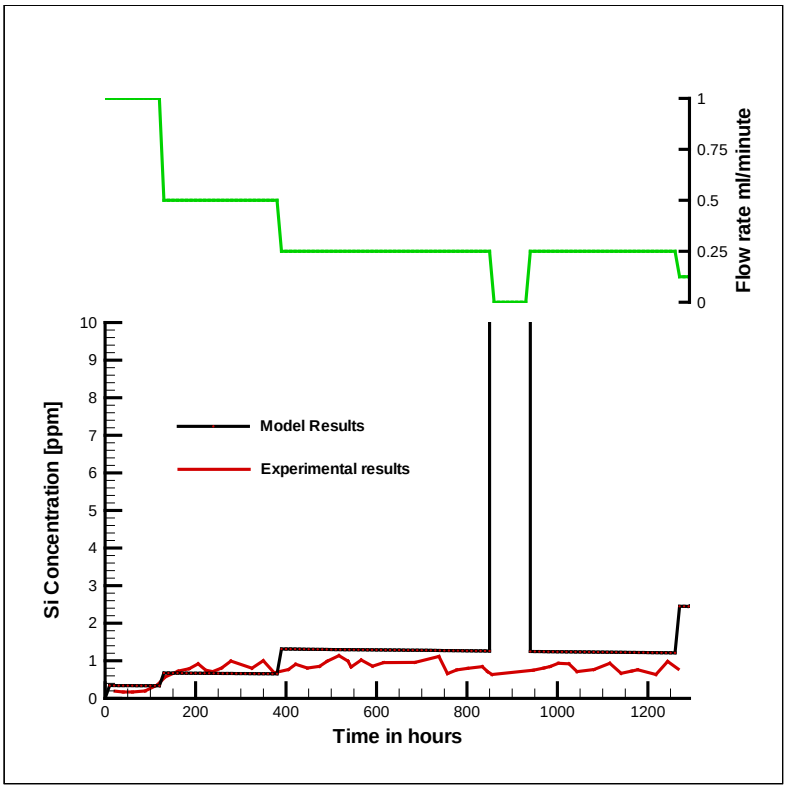

Figure 3.22 Si concentration for pressure solution and chemical etching model. The raised concentration during the no flow period is a numerical artefact to be removed in further model development.

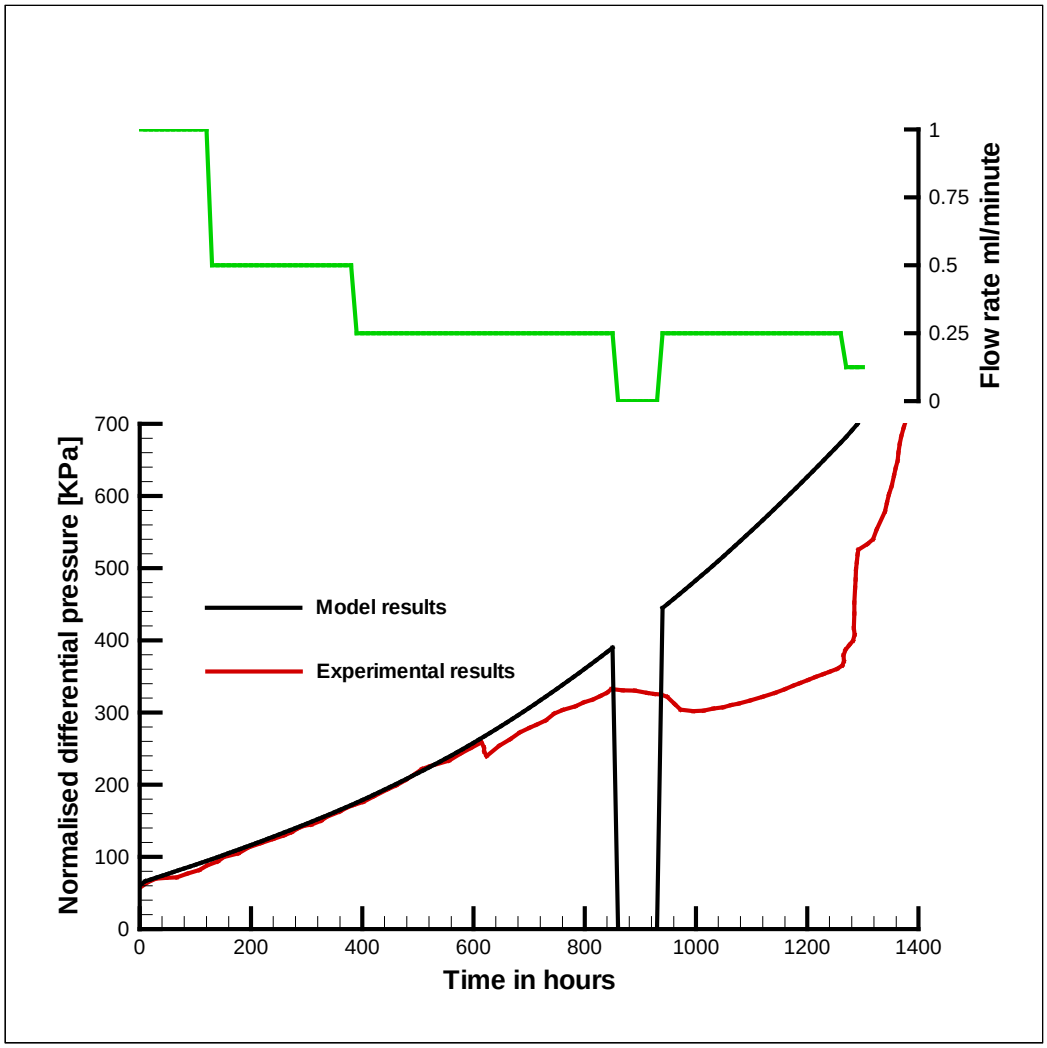

Figure 3.23 Normalised pressure differential for pressure solution and chemical dissolution model.

Table 3.3. Fitting parameters for linear pressure solution model with and without chemical dissolution

	α_p	$2\alpha_p k_+ V_s$ OGS input value	α_c	$2k_+ V_s \alpha_c$ OGS input value
Pressure solution only	0.177	1.95×10^{-19}	0	0
Pressure solution and chemical dissolution	0.212	2.34×10^{-19}	7.79×10^{5}	0.86×10^{-12}

Discussion points

Both the pressure solution only and the pressure solution with chemical etching models can be made to match the experimental data for the change of the hydraulic aperture with time. However, the pressure solution only model matches the chemical experimental data better than the pressure solution and chemical dissolution model.

In contrast to the model results, the chemical data, apart from the initial 121 hours, are independent of the flow rate. This suggests some sort of saturation or pseudo-equilibrium of dissolved SiO_2 has been reached under the flow conditions. The pore volume replacement rate for the fracture at the lowest flow rate of 0.125 ml/minute can be shown to be of the order of 35 seconds. This suggests a rapid equilibrium type relationship, not currently reflected in the model.

Reconciling the above observations requires a model that includes both pressure solution and chemical etching. This model needs to allow the SiO_2 moved during pressure solution to be either fairly instantaneously re-precipitated around contact points or allow plastic deformation of the SiO_2 at the contact points.

Neither model can reproduce the deviation seen around 600 hours that continued until circa 1400 hours. At present the inference is that this signal is either through a faulty resetting of a measuring device, or the faces of the fracture have been jolted in some way due to the loss of fluid and confining pressure during the flow shutdown. It is interesting to note that Yasuhara et al. (2006) “ignore” this feature and fit general curves across it. Discussions are underway with the experimentalists to better understand this feature of the experiment.

Although the pressure solution is not unrealistic, the chemical dissolution model requires high dissolution rate. We note that the dissolution constant is significantly impacted by temperature and at the higher temperatures in the later stages of the test (up to 120°C) the dissolution rate is over four orders of magnitude larger than at 20°C. Also we note in other work that the fracture area is greatly increased by the fractal nature of the fracture surface and that the fracture in the experiment is a freshly broken surface. These factors would augment each other to increase the expected chemical dissolution rate significantly.

The results so far suggest that the pressure solution model should be further developed to include non-linear effects, and the chemical dissolution will become more important for later stages of the experimental test. Plastic deformation or rapid precipitation of quartz will also be investigated as a way of reconciling the above observations, i.e. a method of redistribution SiO_2 from the pressure solution without the SiO_2 entering the fluid.

3.3.4 Homogenised Approach for Step 0

3.3.4.1 Approach

The homogenised approach uses the fracture topography data in a fundamentally different way to that adopted in the previous section. Rather than explicitly characterising the aperture locally, determining the aperture and whether the two sides are in contact, the homogenised approach characterises a distribution of contact ratio (fraction of a given area in contact) with aperture. Given the early stages of this work, the contact-ratio/aperture distribution inferred from the data as used by Yasuhara et al. (2006) was adopted (Figure

3.24). The key advantage of this approach is that it allows the fracture to be represented by a relatively coarse resolution, or as a whole, while retaining some of the critical information of the fracture geometry. However, information on the geometry is lost, and the challenge with such an approach is to make the process model sufficiently complete that the physical representation can be good enough without the explicit representation of the fracture surface topography.

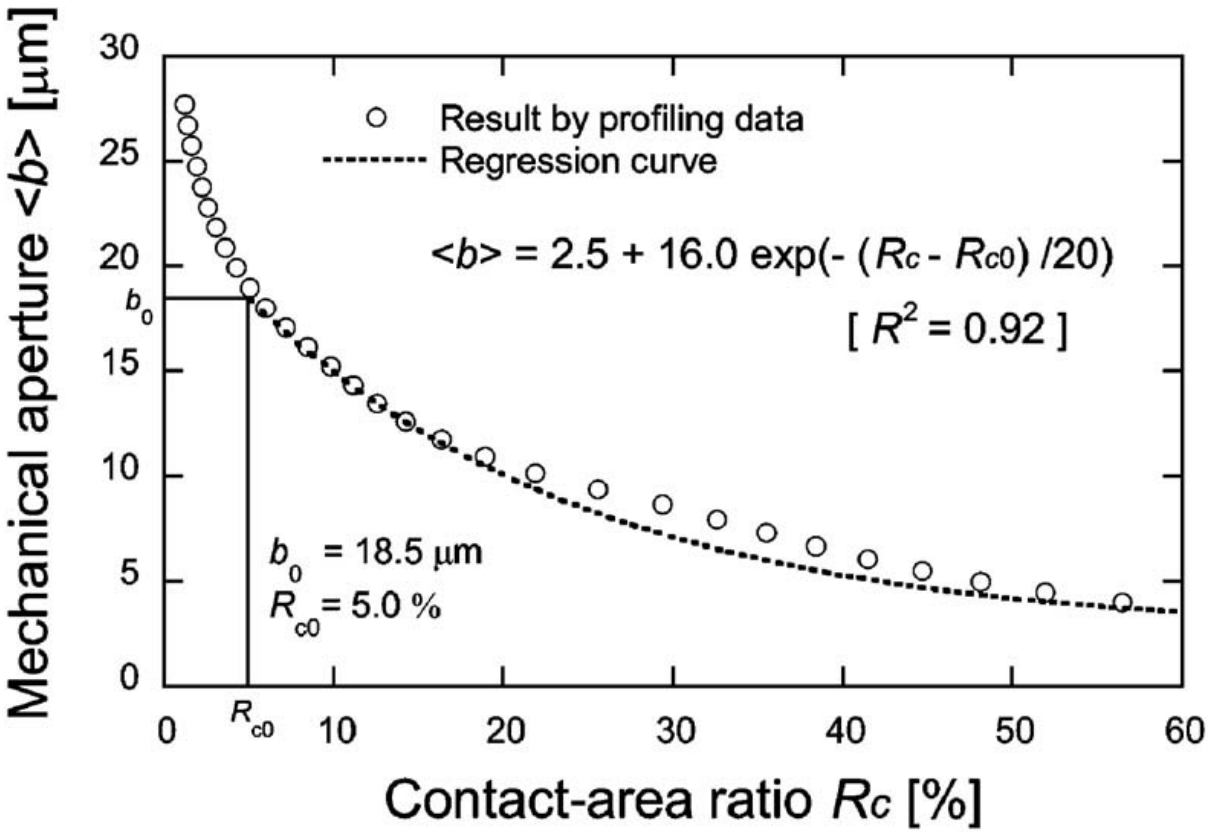

Figure 3.24. Function of contact area versus mechanical aperture used in the homogenised model (from Yasuhara et al., 2006).

The step 0 homogenised model was constructed in QPAC (Quintessa, 2013) using pre-existing 'modules' (pre-built collections of physical process models). No code development was required for this work, as the additional functionality was created through the QPAC input language as part of the model input files. QPAC describes discrete volumes in a model as 'compartments' and the two dimensional intersections between those compartments as 'interfaces' or 'boundaries' when describing the outer surface of the model. A fuller description of QPAC is given in Appendix B

The Step 0 model comprises the following components, using a single compartment to represent the entire fracture:

- Darcy flow: simple single phase, fully water saturated flow of water through porous media and fractures.

- Reactive transport: fate and transport of reactive species and minerals. The module is highly capable, containing far more processes than required in the novaculite case.

- Pressure solution: ad-hoc user created model coupling to the Reactive transport module.

Because the initial model considers only a single compartment, the processes associated with mechanical coupling between adjacent compartments (e.g. local stress redistribution due to bridging or changes in contact ratio) are not required, but could be required in the future.

The implementation of the model and the conceptual model for each process set are described in more detail in the following sections.

3.3.4.2 Model Conceptualisation and Implementation

Water Flow

The system was assumed to be representable as a single volume in which the fracture represents the total open volume in the experiment and the rock represents the remaining volume. Water flow passing through the fracture is assumed to be well-mixed by the time the injected fluid leaves the sample (Figure 3.25). Consistent with the Yasuhara et al. (2006) aperture model, the starting average aperture was assumed to be 18.5 μm.

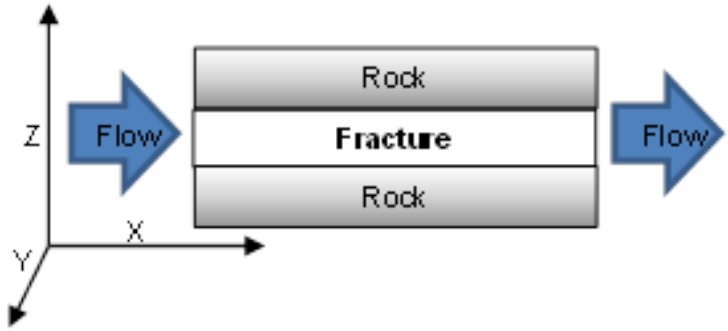

Figure 3.25. Schematic illustration of the Step 0 homogenised model

For the purposes of simple implementation, the system was treated as a porous medium with all the pore space representing the open fracture. This was adopted simply to maintain constant compartment volume and interface areas for Darcy flow and reactive transport modules, so;

fracture volume = porosity × compartment volume

and

fracture aperture = porosity × compartment height

Consistent with the high resolution approach and Yasuhara et al. (2006) a simple parallel plate approximation was adopted, hence the intrinsic permeability of the fracture is given by the Boussinesq approximation (Boussinesq, 1868), as shown in equation (30). Consistent with the use of porosity to represent the fracture volume, the net intrinsic permeability of a given compartment of rock and fracture becomes

$$k_{net} = \theta \frac{b_t^2}{12} \tag{45}$$

where θ is the effective porosity of rock + fracture compartment.

The Darcy velocity (q) is then made available for use by the reactive transport module for the calculation of the advective and diffusive fluxes of aqueous species.

Aperture Change

In the current Step 0 model, consistent with the high resolution model, there are two processes directly affecting aperture change:

1. Chemical dissolution/precipitation
2. Pressure solution.

Aperture opening/closing by surface dissolution/precipitation is handled through the kinetic rate equation described in Section 3.3.1, noting that the effective area for dissolution/precipitation is scaled by one minus the contact ratio.

The effective area used for the fractures was the simple planar area, noting that the small-scale fracture roughness could significantly increase the net dissolution rates.

The model for the decrease in aperture $\frac{\mathrm{db}}{\mathrm{dt}}$ (m s^{-1}) due to pressure solution was taken from Yasuhara et al. (2004), which is based on a purely theoretical model.

$$\frac{\mathrm{db}}{\mathrm{dt}} = \frac{3V_m^2(\sigma_a - \sigma_c)k_+}{RT} \tag{46}$$

where V_m (m^3 mol^{-1}) is molar volume of solid (quartz), σ_a (Pa) is the disjoining pressure (amount by which the stress acting on the grains in contact exceeds the hydrostatic pore pressure), σ_c (Pa) is the critical stress for quartz defined in Eqn (17) Yasuhara et al. (2004), the pressure solution effect only occurs when σ_a exceeds σ_c, k_+ (mol m^{-2} s^{-1}) is the pressure dissolution rate constant, R (J K^{-1} mol^{-1}) is the gas constant, and T (K) is the temperature.

The molar rate of quartz entering solution $\frac{dM_{mol}}{\mathrm{dt}}$ (mol s^{-1}) is then

$$\frac{dM_{mol}}{\mathrm{dt}} = \frac{\mathrm{db}}{\mathrm{dt}} A_c^l \frac{1}{V_m} \tag{47}$$

for local contact area A_c^l (m^2) and the change in volume $\frac{dV_f}{\mathrm{dt}}$ (m^3 s^{-1}) to close the fracture is

$$\frac{dV_f}{\mathrm{dt}} = \frac{\mathrm{db}}{\mathrm{dt}} A_{XY} \tag{48}$$

Figure 3.26 shows how pressure dissolution at a touching part of the fracture affects the fracture aperture, hence maintaining the required local volume.

It should be noted that the actual pressure solution model described in Yasuhara et al. (2004) has the quartz dissolve into a super-saturated water film and then diffuse into the pore water, but this element of the model is simplified out of the functional form adopted, because it is assumed that the concentration gradient is large across such a film (as evidenced by the relatively low Si concentrations in the outflowing water) and hence all dissolved quartz produced by pressure dissolution enters the pore water.

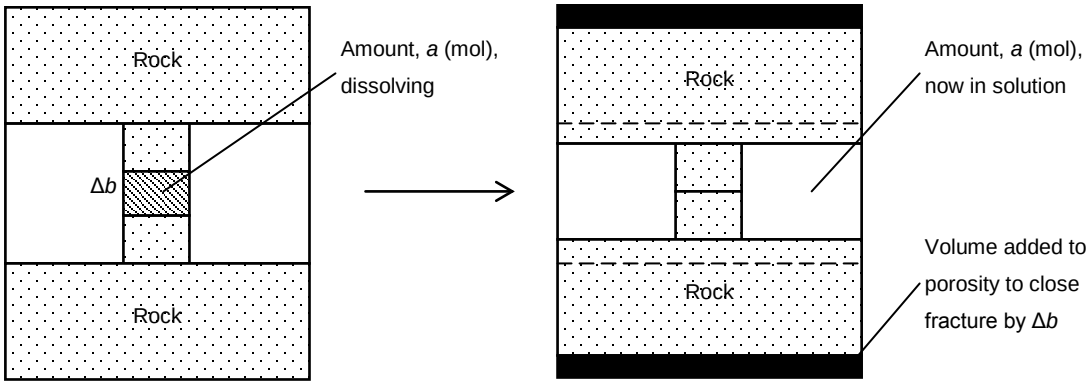

Figure 3.26. Illustration of how the change in aperture due to pressure solution is handled in the QPAC model.

The factors f_c (-) and f_k (-) are introduced to allow calibration and sensitivity analysis of the model to the critical stress and dissolution rate constant respectively, hence equation (46) is rewritten as:

$$\frac{\mathrm{db}}{\mathrm{dt}} = \frac{3V_m^2(\sigma_a - f_c\sigma_c)f_k k_+}{RT} \tag{49}$$

Implementation

The aperture changes by surface dissolution/precipitation and pressure solution effect are applied through the mineral precipitation rate k_0 (mol m^{-2} s^{-1}) of the QPAC reactive transport module by introducing a non-reactive quartz mineral with the same molar weight and molar volume as quartz.

$$k_Q = k_Q^S - \frac{dM_{mol}}{\mathrm{dt}} \frac{1}{m_Q V_{comp} A_{mol,Q}} \tag{50}$$

$$k_I = \frac{dV_f}{\mathrm{dt}} \frac{1}{V_m} \frac{1}{m_I V_{comp} A_{mol,I}} \tag{51}$$

$$k_Q^S = k_{0,Q}\left(\frac{Q}{K} - 1\right) \tag{52}$$

For $i = Q, I$ representing reactive and inert quartz, k_Q^S (mol m^{-2} s^{-1}) is the free surface dissolution rate, $\frac{dV_f}{\mathrm{dt}}$ (m^3 s^{-1}), $\frac{dM_{mol}}{\mathrm{dt}}$ (mol s^{-1}), and V_m (m^3 mol^{-1}) are as described above, m_i (mol m^{-3}) is the amount of mineral per unit volume of the compartment, $A_{mol,i}$ (m^2 mol^{-1}) is the reactive surface area, and V_{comp} (m^3) is the compartment volume.

The QPAC reactive transport module takes k_i (mol m^{-2} s^{-1}) as input and calculates the compartmental mineral growth rate r_i (mol m^{-3} s^{-1}) as given in equation (53). Equations (50) and (51) include divisions by $(m_i V_{comp} A_{mol,i})$ to be compatible with this mineral growth rate and to apply the change in amount/volume independently of the compartment volume.

$$r_i = k_i A_{mol,i} m_i \tag{53}$$

The overall model, despite being only a single compartment, is relatively complex, and the interactions between the component processes are shown in Figure 3.27.

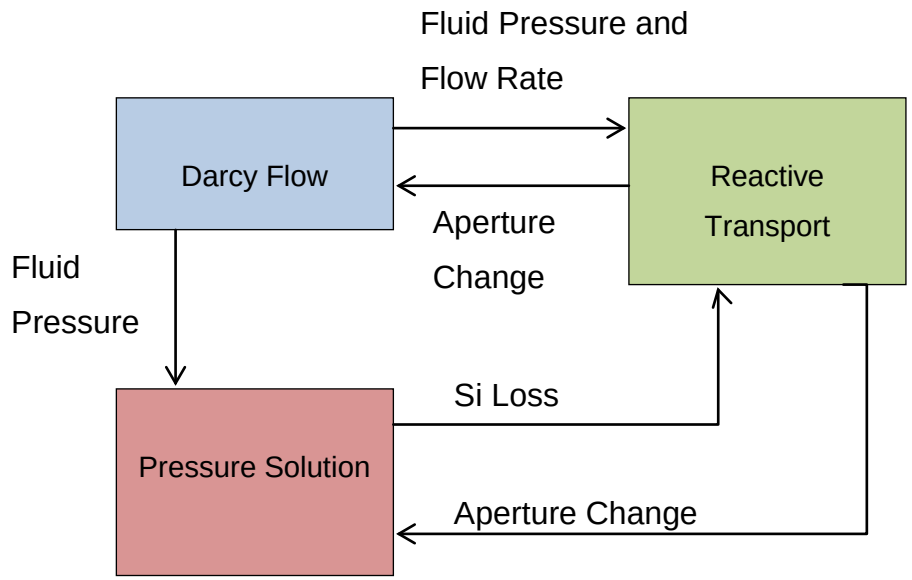

Figure 3.27 Schematic illustration of the coupling in the QPAC Step 0 model.

The model was calibrated to the experimental data by adjusting the f_c and f_k scaling factors; the input parameterisation is summarised in Table 3.4. Results are presented in the following section.

Table 3.4. Reference parameterisation for the calibrated Step 0 homogenised model.

Parameter		Value	Notes
Density water		998 kg m^{-3}	@ 20ºC
Viscosity water		1.002 mPa s	@ 20ºC
Confining stress		1.72 MPa	
Back pressure		345 kPa	
Critical stress (for pressure solution) (Pa)		$\sigma_c = \frac{E_m\left(1-\frac{T}{T_m}\right)}{4V_m}$ E_m = 8.57 kJ mol^{-1} T_m = 1883 K	Eqn (2) Yasuhara et al. (2004), values given for quartz.
Pressure dissolution rate constant (mol m^{-2} s^{-1})		$k_+ = k_+^0 \exp\left(-\frac{E_{k_+}}{RT}\right)$ k_+^0 = 1.59 mol m^{-2} s^{-1} E_{k_+} = 71.3 kJ mol^{-1}	Eqn (2) Yasuhara et al. (2006), values given for quartz.
Molar volume quartz, V_m		22.688 cc/mol	
Molar weight quartz		60.0843 g/mol	
Fracture length		89.5 mm	
Fracture width		50.0 mm	
Aperture contact-ratio relationship (μm)		$\langle b \rangle = 2.5 + 16.0 \exp\left(-\frac{R_c - R_{c0}}{20}\right)$ Note: R_c, R_{c0} in %	Fig. 9 Yasuhara et al. (2006)
Reaction rates and log K values for free surface geochemistry	20ºC	2.437×10^{-14} mol m^{-2} s^{-1}	
	40ºC	2.583×10^{-13} mol m^{-2} s^{-1}	
	80ºC	1.301×10^{-11} mol m^{-2} s^{-1}	
	120ºC	2.953×10^{-10} mol m^{-2} s^{-1}	
f_c (-)		0.05	
f_k (-)		1.6×10^6	

3.3.4.3 Homogenised Model Results

The calibrated results are shown in Figure 3.28, Figure 3.29 and Figure 3.30.

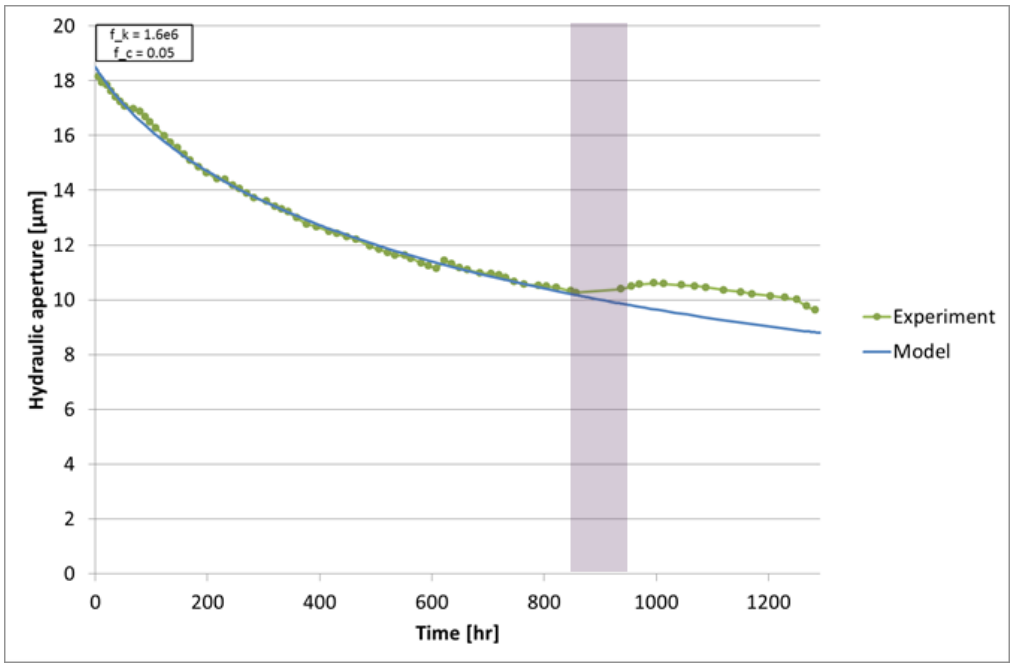

Figure 3.28. Step 0 homogenised model aperture change – zero flow period is marked in red

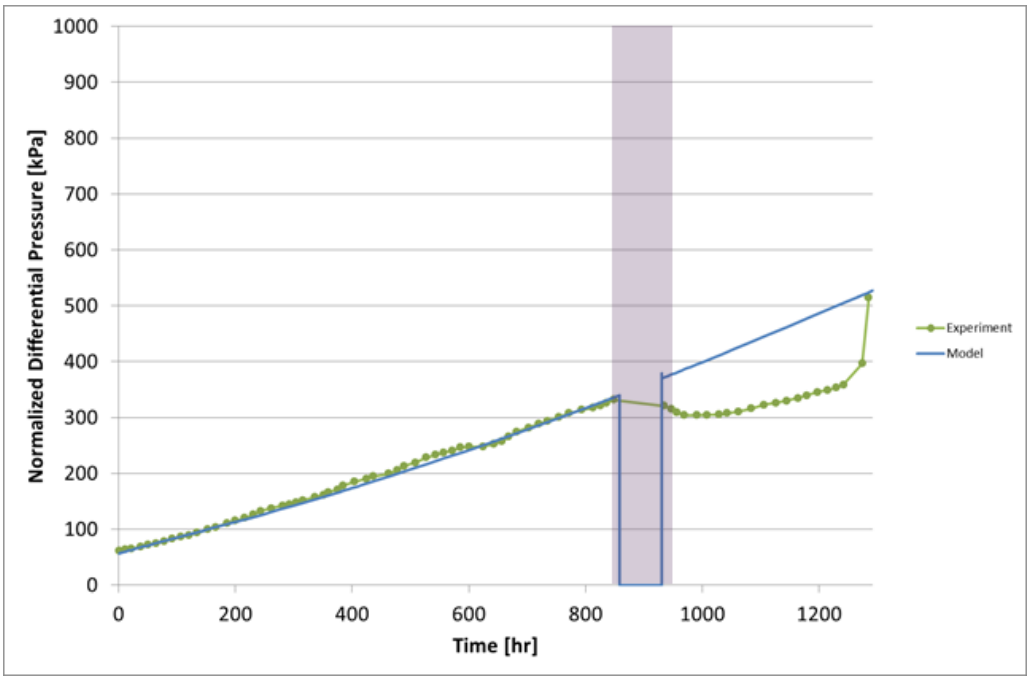

Figure 3.29. Step 0 homogenised model normalized differential pressure – zero flow period is marked in red

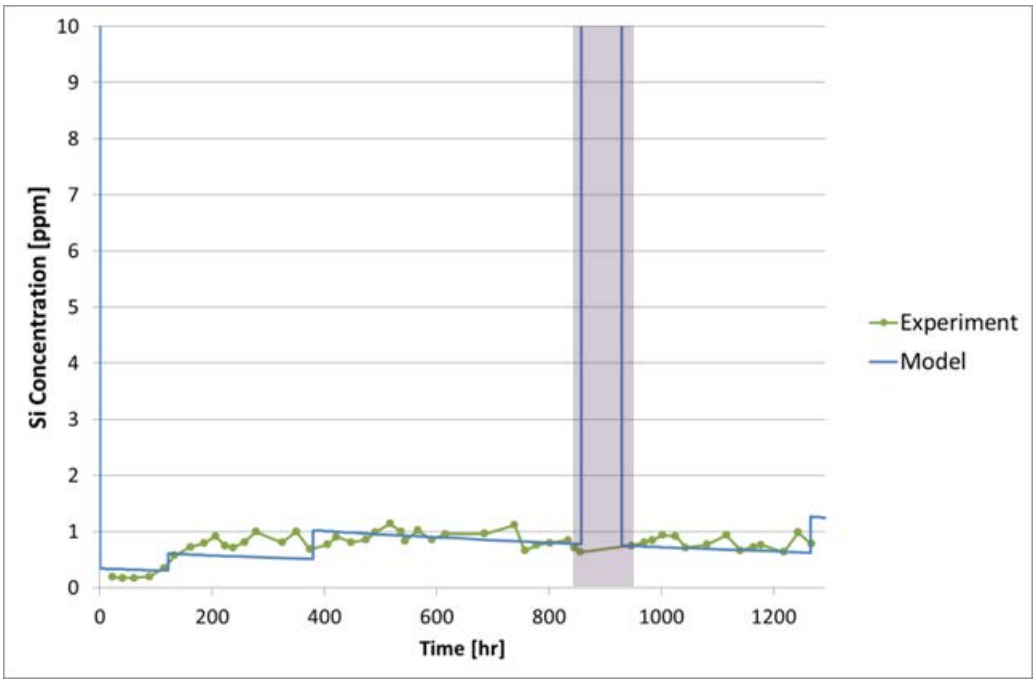

Figure 3.30. Step 0 homogenised model Si concentrations – zero flow period is marked in red

Clearly the model shows a good fit to the experimental data. The clear exception is most notable on the hydraulic aperture and differential pressure plots, where the change in behaviour during the zero flow period is not reflected by the model. The reasons for this have been discussed in the context of the high resolution model, and are a subject for future investigation.

In the process of calibration a series of sensitivity tests were conducted. These results are omitted for brevity, however it was found that the treatment of the critical stress was a major factor in obtaining a good calibration, without recourse to adjustment to the surface areas for chemical dissolution. This is important because the pressure-solution model used in the high resolution model (see previous sections) made the typical assumption of setting the critical stress to zero, i.e. pressure solution occurs at all stresses. In the homogenised model it was observed that the inclusion a small critical stress enables the reproduction of the reduction in rate of aperture closure without recourse to enhanced chemical dissolution to keep the aperture open on average. It is entirely likely that a combination of effects is actually operating and that both enhanced dissolution (through enhanced fracture roughness) and critical stress effects are combining to produce the reduction in net aperture loss with time.

The calibration factors on the theoretical pressure dissolution model are also interesting. The factors cause a decrease in critical stress and the enhancement of the rate of pressure dissolution. Such changes are arguably consistent with the contact ratio model over-estimating contact between surfaces, i.e. stresses are more concentrated than the simple contact ratio model would suggest. Such a result is physically plausible when considering the likely roughness of the artificial fracture surfaces below the scale of the fracture topography information. Thus obtaining a consistent set of parameterisation requires enhancing the rates of pressure solution. The work of Yasuhara et al. (2004, 2006) also required enhancements to the pressure solution rates, so this result is not without precedent.

3.4 Step 1

The high resolution approach is inherently suitable for application to Step 1, so no work was conducted to test this further. However the homogenised model had not been tested when run in a 2D mode, so some simple tests were conducted to ensure the model could be used, and to identify areas for improvement before Step 1 was attempted.

The reference Step 0 homogenised model was expanded to a 20x40 grid, considering aperture closing/opening separately in each compartment. Average apertures were varied across the grid by using the same fracture surface offset model used by the high resolution model (Section 3.3.3), and taking the geometric mean calculated aperture across each cell. The resulting flow vectors are shown in Figure 3.31, and the evolution of aperture across the first 900 hours shown in Figure 3.32 and Figure 3.33.

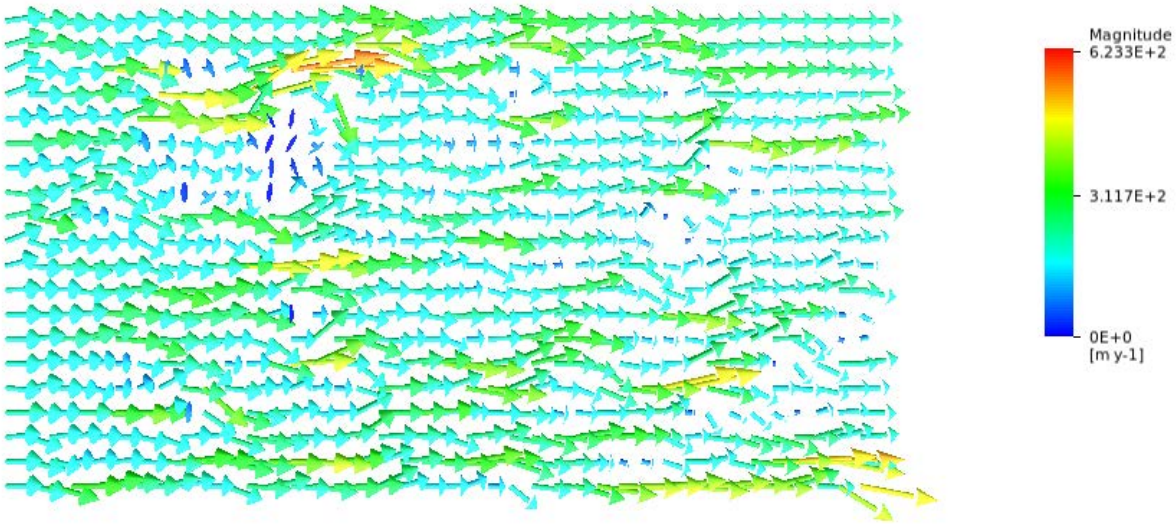

Figure 3.31: Darcy velocity at t=0 (i.e. 1 mL/min flow rate)

While the results appear to be superficially sensible, the process models as implemented are not appropriate because parts of the fracture with no pressure solution (due to the impact of critical stress) do not get closer together, because the compartments are treated independently. This is illustrated by the difference in contact ratios in Figure 3.34 and Figure 3.35. Clearly, the lack of mechanical coupling between compartments creates this unphysical effect, an area that will need to be addressed for Step 1.

It is also the case that the homogenised model uses a constant aperture/contact ratio model. It is likely that consideration of more complex mechanics, microstructure evolution and thermal effects, may require such a simple model to be reconsidered.

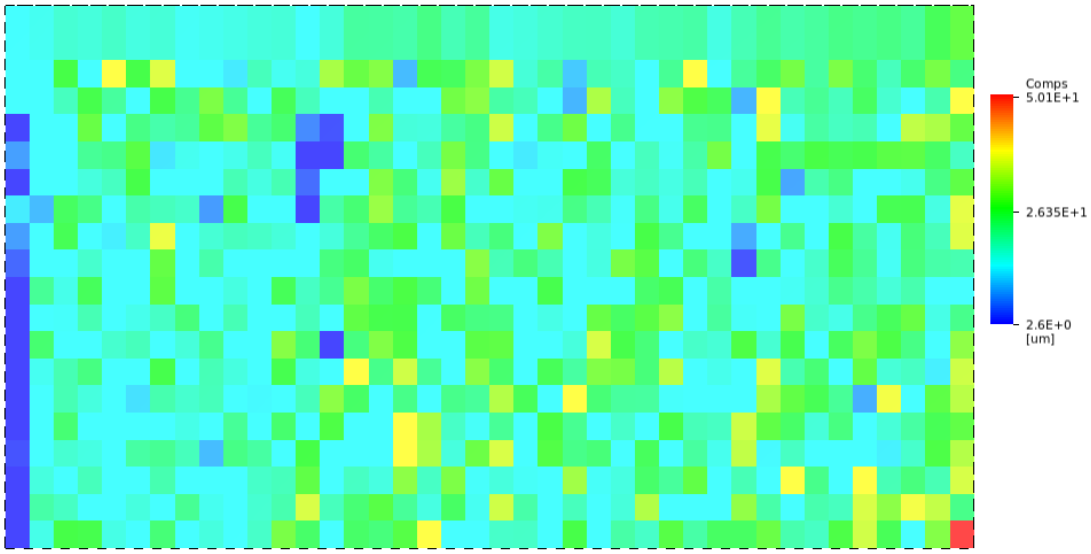

Figure 3.32: Aperture at t=0 hrs.

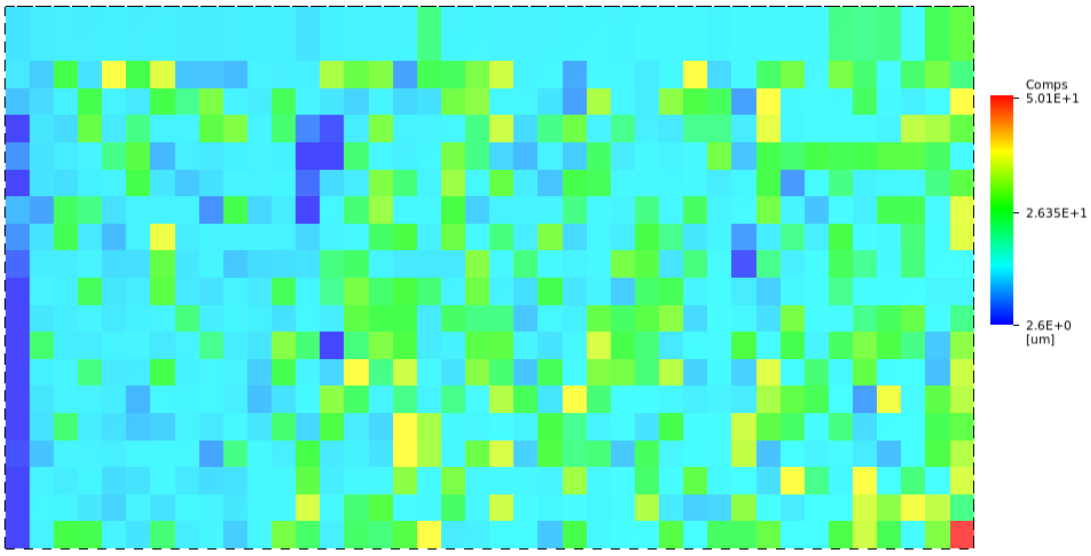

Figure 3.33: Aperture at t= ~900hrs

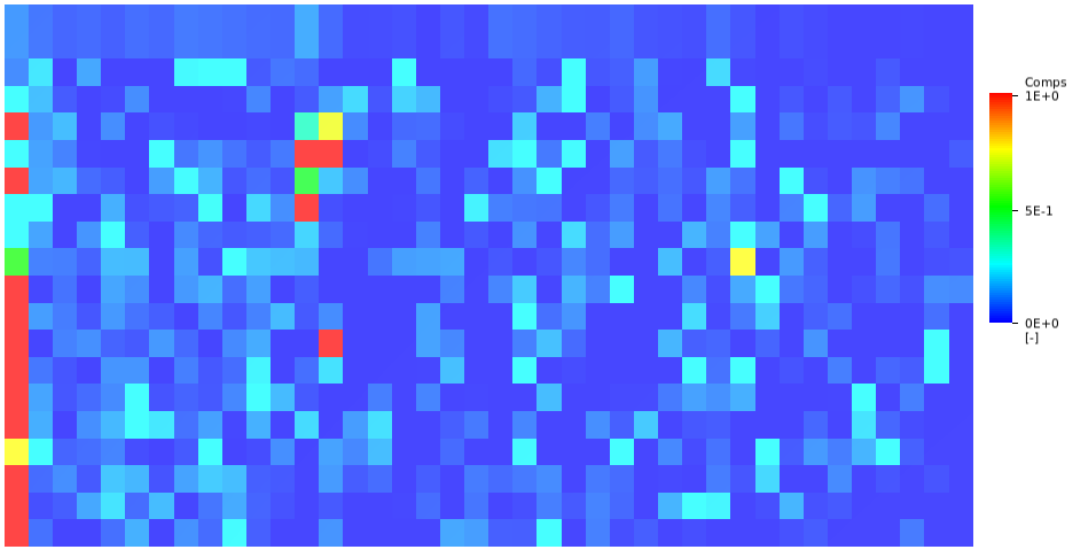

Figure 3.34: Contact ratio at t=0 hrs

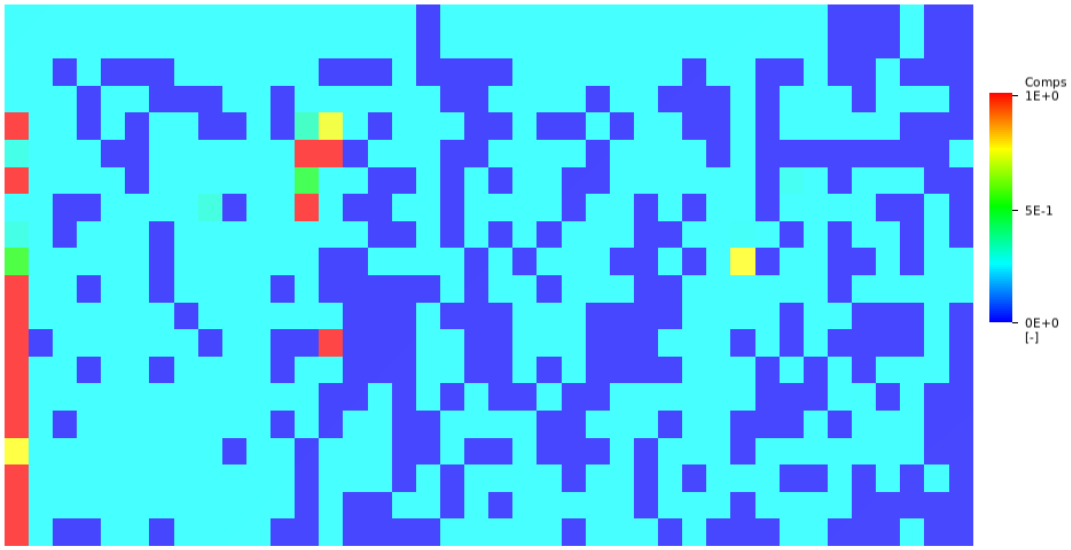

Figure 3.35: Contact ratio at t= ~900 hrs

3.5 Task C Summary

Despite the relatively early stage of Task C, the work so far, using two different modelling approaches to the same data set, is promising. Both approaches were able to represent the early hydro-mechanical-chemical history of the novaculite experiment using similar process models. Both models showed that enhancement to the theoretical rates of pressure dissolution and/or chemical dissolution were required in order to fit the experimental data; the increase in rates being justified by the expected high degree of initial roughness at the microscopic scale of the artificial fractures.

Both models illustrated that the simple pressure solution model alone cannot explain the aperture change during the early part of the experiment and that the pressure solution model itself requires adjusting (non-linearity or the inclusion of a critical stress) or chemical dissolution must be significantly greater than one might initially expect.

There are also consistent issues with the models, in that both predict 'stepped' responses to dissolved silicon concentrations with changing flow rates, however the experimental data do not show this response. Whether this is simply a function of the fracture heterogeneity smearing the responses, the 'noise' in the silicon concentration data, or whether additional processes are required will likely form the basis of the next phase of work.

In particular, the following areas are highlighted for particular attention:

- Revisit the relative potential impacts of critical stress and enhanced dissolution.
- Additional local processes (e.g. plastic mechanical effects, 'stress corrosion')
- Representation of larger-scale mechanical effects (e.g. stress redistribution)
- Understanding the physical changes associated with the zero flow portion of the experiment.

Overall, it has been found that the adoption of two models, with contrasting and complementary approaches, has been extremely useful in this case and the intention will be to continue considering homogenised and detailed models in parallel.

4 Conclusions of the first year of DECOVALEX-2015 work by the AMEC team

4.1 Summary of Progress

Both Task A and C1 have been participated in fully by the RWM team, fully satisfying the requirements of the Task plans, despite the complexity of some of the work.

Task A has illustrated the complexities of understanding hydro-mechanical processes in bentonite-rich materials, even under very well-constrained conditions. Conventional soils approaches clearly struggle to replicate the experimental observations, forcing the use of more complex and non-linear physical representations that are difficult to parameterise without a very wide range of experimental data. Using such approaches, good fits were obtained against the Step 0 hydro-mechanical experimental data, although concerns remain about the uniqueness of the parameterisation and the predictive power of the models. Despite these problems, it appears that reasonable blind predictions have been made against Step 1 (certainly as good as could reasonably be expected given the inconsistencies between the two steps). The use of blind predictions in Task A is an especially useful addition to the body of knowledge on bentonite because it gives a better insight to the level of uncertainty one might expect to have going from partially constraining experimental data to an application. This is in contrast to the majority of previous work where the modelling has considered only retrospective calibration to experimental data.

For Task C1 the combination of two different approaches has produced a consistent view of the issues with the experimental data and both approaches provide a suitable and complementary way forward. It is reasonable to expect that the task will enable the creation of fully-coupled THMC models of single fractures by the end of the project duration, as planned.

Work on a new constitutive model for bentonite-rich materials has started and is showing promising early results. It is expected that the development of this constitutive model along with work using more conventional approaches will aid understanding and boost confidence in the new model.

4.2 Issues of Potential Significance to RWM

No specific issues have been raised by the Task C1 work to date. However the work under Task A has demonstrated the complexity in creating robust, predictive hydro-mechanical models of bentonite-rich materials from single sets of experiments. While models can be created and calibrated to experimental data, creating predictive models is considerably more problematic unless the supporting data used to derive the models completely encompass the conditions under which the prediction is to be made, irrespective of the code being used. It should be expected that any such coupled modelling in the RWM programme will need to take full account of the available literature in order that appropriate models can be set up, and not rely on a sub-set of experimental data.

4.3 Way Forward

For Task C1 the way forward is clear. The discretised and homogenised models of a single fracture both have merits and are complementary in terms of their use. It is proposed that this line of investigation is maintained into Step 1 and 2 of Task C1. However, given the results from Step 0, there is a clear requirement to investigate a wider range of physical processes to try to attempt to explain some of the aspects of the experiments that are not well captured by the existing model. Examination of localised mechanical failure ('stress corrosion') will be a high priority, as will a fuller consideration of the issues around the most appropriate surface areas for the different process sets.

Task A has been delayed from the original programme with Step 2 now no-longer starting until at least November 2013. Given the progress made by the RWM team there are no specific modelling requirements for the meeting in November 2013. This gives an opportunity to continue to develop the new constitutive model, but also to attempt to learn from the results of the Step 1 blind prediction, when the full set of results become available. Given that Step 0 and Step 1 do not provide sufficient data to adequately constrain the hydro-mechanical models used to make reliable predictions (e.g. no information on lateral stresses, or swelling volumes under different stress states), it is proposed that the QPAC Cam-Clay and flow model is extended to be consistent with the full BBM model. This will allow the team to access the results of a wide range of experiments that were modelled using the BBM.

In terms of the work focussing on the new constitutive model, the implementation and testing of the BBM as well as application to Step 0 and Step 1 data would provide a valuable additional dataset to prove the validity of the new model, as well as allowing further consistency and confidence building between the two approaches.

The programme of work continues until November 2015, and future annual progress reports, in addition to a final report, will be published documenting progress and key conclusions.

5 References

Alonso, E. E., Lloret, A., Delahaye, C. H., Vaunat, J., Gens, A., & Volckaert, G. (1998). COUPLED ANALYSIS OF A BACKFILL HYDRATION TEST, *22*(April 1997), 1–27.

ANDRA (2005). Dossier 2005 Argile. Tome Safety evaluation of a geological repository.

Benbow, S. J. and Watson, C. E. (2011). QPAC Reactive Transport Module: Theory and Testing. QRS-QPAC-RTM-2 v1.0.

Bethke, C. M. (2008). Geochemical and Biogeochemical Reaction Modelling. Cambridge University Press.

Bolt, G. H. (1956) Physico-chemical analysis of the compressibility of pure clays: *Geotechnique* VI, 86-93.

Bond, A. E., Maul, P. R., Savage, D. & Wilson, J. (2009). The Use of QPAC-EBS for Project THERESA Full-Scale Tests. Quintessa Report QRS-3009A-2 version 2.0.

Bond, A. E. (2010). A thermal module for QPAC. Quintessa Report QRS-QPAC-THM-1 v1.0.

Bond, A. E. (2013a). A mechanical module for QPAC. Quintessa Report QRS-QPAC-MECH-1 v1.0.

Bond, A. E. (2013b). Specification for DECOVALEX-2015: Task C1. Steps 0 and 1. Quintessa Report to the DECOVALEX-2015 Project. QRS-1612B-S-0-1v1.2.

Bond, A. E. & Benbow, S. J. (2009). QPAC Multi-Phase Flow Module Functional Specification and Architectural Design. Quintessa Report QRS-QPAC-HYD-2 v1.0.

Börgesson L, Johannesson L-E, Sandén T, Hernelind J, (1995). Modelling of the physical behaviour of water saturated clay barriers. Laboratory tests, material models and finite element application. SKB TR 95-20, Svensk Kärnbränslehantering AB.

Börgesson, L. (2007). Canister Retrieval Test, Compilation made for the EBS Task Force.

Borja, R. I. (2004). Cam-Clay plasticity. Part V: A mathematical framework for three-phase deformation and strain localization analyses of partially saturated porous media. *Computer Methods in Applied Mechanics and Engineering*, *193*(48-51), 5301–5338. doi:10.1016/j.cma.2003.12.067.

Borja, R., & Lee, S. (1990). Cam-clay plasticity, part 1: implicit integration of elasto-plastic constitutive relations. *Computer Methods in Applied Mechanics and …*. Retrieved from http://www.sciencedirect.com/science/article/pii/004578259090152C.

Boussinesq J (1868). Mémoire sur l'influence des frottments dans lem mouvemants reguliers des fluids, *J Math. Pure Appl*, **Vol 13, Ser 2**, 377-424.

BRGM (2011). Thermoddem geochemical database, Geochemist's Workbench version 'gwb_lv1_thermoddem_lvl1_no-org_15dec11'. http://thermoddem.brgm.fr/recherche.asp

Carman, P. Z. (1956). Flow of gases through porous media, Butterworths , London.

CoRWM (2009). Report on National Research and Development for Interim Storage andGeological Disposal of Higher Activity Radioactive Wastes, and Management of NuclearMaterials. Committee on Radioactive Waste Management Report to Government.

Croney D., Coleman J.D., Black W.P.M., (1958). Movement and distribution of water in soil in relation to highway design and performance, In Water and its conduction in soils, ed. H.F. Winterkorn, Highway Research Board Special Report no 40, pp 226-253.

Cui, Y. , Yahia-Aissa, M., & Delage, P. (2002). A model for the volume change behavior of heavily compacted swelling clays. *Engineering Geology*, *64*(2-3), 233–250. doi:10.1016/S0013-7952(01)00113-2.

Cui, S.-L., Zhang, H.-Y., & Zhang, M. (2012). Swelling characteristics of compacted GMZ bentonite–sand mixtures as a buffer/backfill material in China. *Engineering Geology*, *141-142*, 65–73. doi:10.1016/j.enggeo.2012.05.004.

Deer, W. A., Howie, R. A., & Zussman, J. (1992). *An introduction to the rock-forming minerals. - 2nd Edition* (p. 695). Pearson Prentice Hall.

Delage, P., Howat, M., & Cui, Y. (1998). The relationship between suction and swelling properties in a heavily compacted unsaturated clay. *Engineering Geology*, *50*(1-2), 31–48. doi:10.1016/S0013-7952(97)00083-5.

Department for Environment, Food and Rural Affairs (Defra), Department for Business, Enterprise and Regulatory Reform, Welsh Assembly Government, and Northern Ireland Department of the Environment (2008). Managing Radioactive Waste Safely: A Framework for Implementing Geological Disposal. Cm 7386, ISBN 0101738625.

Duerk, A. (2005). Hydro-mechanical properties of a water unsaturated sodium bentonite, Laboratory study and theoretical interpretation, Doctoral thesis ISBN 91-973723-6-6.

Gens, A., & Alonso, E. E. (1992). A framework for the behaviour of unsaturated expansive clays. *Canadian Geotechnical Journal*, *29*, 1013–1032.

Gratier, J. P., R. Guiguet, F. Renard, L. Jenatton & D. Bernard (2009). "A pressure solution creep law for quartz from indentation experiments." *Journal of Geophysical Research B: Solid Earth* 114(3).

Gunnarsson, I. & Anórsson, S. (2000). Amorphous silica solubility and the thermodynamic properties of H4SiO°4 in the range of 0° to 350°C at P_{sat}. *Geochimica et Cosmochimica Acta* 64, 2295–2307.

Helgeson, H. C., Delany, J. M., Nesbitt, H. W. & Bird D. K. (1978). Summary and critique of the thermodynamic properties of rock-forming minerals. *American Journal of Science* 278A.

Holmboe, M., Wold, S., & Jonsson, M. (2012). Porosity investigation of compacted bentonite using XRD profile modeling. *Journal of Contaminant Hydrology*, *128*(1-4), 19–32. doi:10.1016/j.jconhyd.2011.10.005.

Howell P., Kozyreff G and J Ockendon (2009). *Applied Solid Mechanics*. ISBN 978-0-521-67109-5.

IRSN (2012). Task A: The SEALEX in-situ experiments. Presentation at 2nd DECOVALEX-2015 Workshop, Leipzig, given by J-D Barnichon, IRSN.

Istok, J. (1989). Groundwater Modeling by the Finite Element Method, American Geophysical Union, 2000 Florida Avenue, NW, Washington, DC 20009.ISBN 0-87590-317-7.Jacinto, A. C., Villar M. and A Ledesma. (2012). *Geotechnique* 62, No. 8, 657–667.

Johnson, J. W., Oeklers, E. H. & Helgeson, H. (1992). SUPCRT92: a software package for calculating the standard molal thermodynamic properties of minerals, gases, aqueous species, and reactions for 1–5000 bar and 0–1000 °C. *Computers & Geosciences* 18, 899–947.

Jönsson, B., Åkesson, T., Jönsson, B., Meehdi, S., Janiak, J., & Wallenberg, R. (2009). Structures and forces in bentonite MX-80. SKB Technical Report TR-09-06.

Josa, A., Alonso, E. E., & Gens, A. (1990). A constitutive model for partially saturated soils. *Géotechnique*, *40*(3), 405–430. doi:10.1680/geot.1990.40.3.405.

Kolditz, O., S. Bauer, L. Bilke, N. Böttcher, J. O. Delfs, T. Fischer, U. J. Görke, T. Kalbacher, G. Kosakowski, C. I. McDermott, C. H. Park, F. Radu, K. Rink, H. Shao, H. B. Shao, F. Sun, Y. Y. Sun, A. K. Singh, J. Taron, M. Walther, W. Wang, N. Watanabe, Y. Wu, M. Xie, W. Xu and B. Zehner (2012). "OpenGeoSys: An open-source initiative for numerical simulation of thermo-hydro-mechanical/chemical (THM/C) processes in porous media." Environmental Earth Sciences 67(2): 589-599.

Komine, H., & Ogata, N. (1996). Prediction for swelling characteristics of compacted bentonite.pdf. *Canadian Geotechnical Journal*, 33, 11–22.

Komine, H., & Ogata, N. (2003). New equations for swelling characteristics of bentonite based buffer materials. *Canadian Geotechnical Journal*, 40(2): 460-475.

Kröhn K (2003). New conceptual models for the resaturation of bentonite. *Applied Clay Science*. *23, 1-4,* 25-33.

Langmuir, D. (1997). Aqueous Environmental Geochemistry. Prentice-Hall.

Lewis, R. W. and B. A. Schrefler (1998). The Finite Element Method in the Static and Dynamic Deformation and Consolidation of Porous Media. Chichester, England, John Wiley & Sons.0-471-92809-7.

Likos, W. J., & Lu, N. (2006). Pore-scale analysis of bulk volume change from crystalline interlayer swelling in Na+ and Ca2+ smectite. *Clays and Clay Minerals*, *54*, 516–529.

Lloret, A., Villar, M. V., Alonso, E. E., Sánchez, M., Gens, A., & Pintado, X. (2003). Mechanical behaviour of heavily compacted bentonite under high suction changes. *Géotechnique*, *53*(1), 27–40. doi:10.1680/geot.2003.53.1.27.

Low, P. F. (1980). . Swelling of Clay: II. The Montmorillonites, *Soil Science Society of America Journal* 44(7832), 667–676.

Low, P. F. (1987). Structural component of the swelling pressure of clays. *Langmuir*, *3*(1), 18–25. doi:10.1021/la00073a004.

MacEwan, D. M. C., & Wilson, M. J. (1980). Interlayer and Intercalation Complexes of Clay Minerals. *Mineralogical Society Monograph No. 5: Crystal Structures of Clay Minerals and their X-Ray Identification* (pp. 197–248). Mineralogical Society.

Manning , C.E. (1994). The solubility of quartz in H_2O in the lower crust and upper mantle. *Geochimica et Cosmochimica Acta* 22, 4831-4839.

Marcial, D., Delage, P., & Cui, Y. J. (2002). On the high stress compression of bentonites, *Canadian Geotechnical Journal* 39(4): 812-820.

Millard, A. & Barnichon, J. (2013). DECOVALEX D-2015: description of Task A (SEALEX experiment). Version 2.

Nagra (2002). Project Opalinus Clay. Safety Report. Demonstration of disposal feasibility for spent fuel, vitrified high-level waste and long-lived intermediate-level waste (Entsorgungsnachweis). Nagra Technical Report 02-05.

NDA (2012). Geological Disposal: RWMD Approach to Issues Management. NuclearDecommissioning Authority Report NDA/RWMD/081 Version 1 March 2012, Harwell.

Nguyen, T. S., Selvadurai, a. P. S., & Armand, G. (2005). Modelling the FEBEX THM experiment using a state surface approach. *International Journal of Rock Mechanics and Mining Sciences*, *42*(5-6), 639–651. doi:10.1016/j.ijrmms.2005.03.005.

Olejnik, S., Posner, A. M., & Quirk, J. P. (1974). Swelling of Montmorillonite in Polar Organic Liquids, *Clays and Clay Minerals*: 22, 361–365.

Palandri, J. L. and Kharaka, Y. K. (2004). A compilation of rate parameters of mineral-water interaction kinetics for application to geochemical modelling. US Geological Survey Open File Report 2004-1068. USA.

Pusch, R. Karnland, O., & Hökmark, H. (1990). GMM — A general microstructural model for qualitative and quantitative studies of smectite clays, (December). SKB Technical Report TR90-43.

Pusch, R, & Yong, R. (2003). Water saturation and retention of hydrophilic clay buffer—microstructural aspects. *Applied Clay Science*, *23*(1-4), 61–68. doi:10.1016/S0169-1317(03)00087-5.

Pusch, R & Yong, R. (2006). *Microstructure of smectite clays and engineering performance* (p. 353). Taylor & Francis. Retrieved from http://books.google.com/books?hl=en&lr=&id=AT-v14NLd04C&oi=fnd&pg=PP1&dq=Microstructure+of+smectite+clays+and+Engineering+performace&ots=zm8ZfFQtkg&sig=a4pW69U-iOo5lY8Ym5YPY3OSBJc.

Quintessa (2013). QPAC: Quintessa's General-Purpose Modelling Software. QRS-QPAC-11. http://www.quintessa.org/repository/files/QRS-QPAC-11(Overview)June2013.pdf.

Robinson, P. C. (2009). A tracer transport module for QPAC. Quintessa Report QRS-QPAC-TTM-1 v1.0.

Rimstidt, J. D. (1997). Quartz solubility at low temperatures. *Geochimica et Cosmochimica Acta* 61, 2553–2558.

Sánchez, M., Gens, A., Do Nascimento Guimarães, L., & Olivella, S. (2005). A double structure generalized plasticity model for expansive materials. *International Journal for Numerical and Analytical Methods in Geomechanics*, *29*(8), 751–787. doi:10.1002/nag.434.

Sánchez, M., Villar M., Lloret A and A Gens. (2007). Analysis of the Expansive Clay Hydration under Low Hydraulic Gradient. Experimental Unsaturated Soil Mechanics. Vol 112, pp 303-318.

Sato, T., Watanabe, T., & Otsuka, R. (1992). Effects of Layer Charge, Charge Location, and Energy Change on Expansion Properties of Dioctahedral Smectites. *Clays and Clay Minerals* 40(1):103–113.

Schofield, A. N. (2006). Disturbed soil properties and geotechnical design, Thomas Telford, p. 216, ISBN 978-0727729828.

SKB (2011). Long-term safety for the final repository for spent nuclear fuel at Forsmark. Main report of the SR-Site project. SKB Report TR-11-01

Taron, J., Elsworth, D. & Min K.B.(2009) .Numerical simulation of thermal-hydrologic-mechanical-chemical processes in deformable, fractured porous media. *International Journal of Rock Mechanics and Mining Sciences*. Volume 46, Issue 5, Pages 842–854.

Tester J. W., Worley W. G., Robinson B. A., Grigsby C. O., & Feerer J. L. (1994). Correlating quartz dissolution kinetics in pure water from 25 to 625°C. *Geochimica et Cosmochimica Acta* 58, 2407-2420.

Tang, A. M., & Cui, Y. J. (2010). Effects of mineralogy on thermo-hydro-mechanical parameters of MX80 bentonite, *2*(1), 91–96. doi:10.3724/SP.J.1235.2010.00091.

Versteeg H. and Malalasekra W. (2007). An Introduction to Computational Fluid Dynamics: The Finite Volume Method (2nd Edition). Pearson Education Limited.

Villar, M. V., Gómez-Espina, R., & Gutiérrez-Nebot, L. (2012). Basal spacings of smectite in compacted bentonite. *Applied Clay Science*, *65-66*, 95–105. doi:10.1016/j.clay.2012.05.010

Walsh, R., C. McDermott and O. Kolditz (2008). Numerical modeling of stress-permeability coupling in rough fractures. *Hydrogeology Journal* 16(4): 613-627.

Wang Q. (2012). Hydro-mechanical behaviour of bentonite-based materials used for high-level radioactive waste disposal. PhD Thesis, Université Paris-Est.

Wang Q., Tang A. M. , Cui Y., Delage P., & Gatmiri, B. (2012). Experimental study on the swelling behaviour of bentonite/claystone mixture. *Engineering Geology* 124 (2012) 59-66. DOI : 10.1016/j.engeo.2011.10.003.

Wayllace, A. (2008). *Volume Change and Swelling Pressure of Expansive Clay in the Crystalline Swelling Regime*. PhD Thesis, University of Missouri.

Wolery, T.J. (1992). EQ3NR, A Computer Program for Geochemical Aqueous Speciation Solubility Calculations: Theoretical Manual, User's Guide, and Related Documentation (Version 7.0). Lawrence Livermore National Laboratory. Livermore, USA.

Yasuhara, H., Elsworth D. and A Polak (2004). *Journal of Geophysical Research*, Vol. 109, B03204, doi:10.1029/2003JB002663.

Yasuhara, H., Polak, A., Mitani, Y., Grader, A., Halleck, P., & Elsworth, D. (2006). Evolution of fracture permeability through fluid-rock reaction under hydrothermal conditions. *Earth and Planetary Science Letters* 244: 186–200.

Yasuhara, H., Kinoshita, N., Ohfuji, H., Lee, D. S., Nakashima, S., & Kishida, K. (2011). Temporal alteration of fracture permeability in granite under hydrothermal conditions and its interpretation by coupled chemo-mechanical model. *Applied Geochemistry* 26: 2074–2088.

Ye, W. M., Cui, Y. J., Qian, L. X., & Chen, B. (2009). An experimental study of the water transfer through confined compacted GMZ bentonite. *Engineering Geology*, *108*(3-4), 169–176. doi:10.1016/j.enggeo.2009.08.003.

Yong, R. (1999). Soil suction and soil-water potentials in swelling clays in engineered clay barriers. *Engineering Geology*, *54*(1-2), 3–13. doi:10.1016/S0013-7952(99)00056-3

Zhang, F., Low, P., & Roth, C. (1995). Effects of monovalent, exchangeable cations and electrolytes on the relation between swelling pressure and interlayer distance in montmorillonite. *Journal of colloid and interface science*, *173*, 34–41. Retrieved from http://www.sciencedirect.com/science/article/pii/S0021979785712933.

Appendix A. OpenGeoSys Formulation and Implementation of HMC model

A.1 Overview

GeoSys / RockFlow is an object oriented C++ code whose architecture is designed around the elements necessary for solving partial differential equations representing mass, or energy balance equations for a modelling domain. Figure A1 illustrates the design of the code, centred around the processes, PCS, to be solved for.

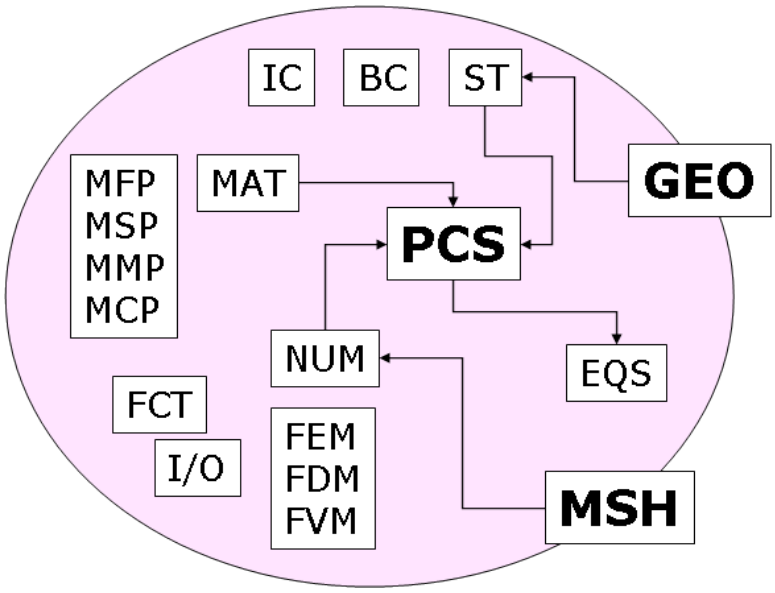

Figure A1: Code architecture of GeoSys / RockFlow

Each box represents a class required for the solution of the equations. Table A1 lists the file types required for construction of a model. For more details on the code construction, method of solution and parameter files the reader is referred to Kolditz et al. (2012).

Table A1: Description of individual elements of the mode code for GeoSys/RockFlow

File Ending (See Figure A1)	Description of Class
PCS	Process
IC	Initial conditions
BC	Boundary conditions
ST	Source terms
GLI (GEO)	Identification of geometrical defined points/polylines/surfaces/ volumes in the model
MSH	Mesh file
EQS	Construct for solver
MFP	Material Fluid Properties
MSP	Material Solid Properties
MMP	Material Medium Properties
MCP	Material Chemical Properties
NUM	Numerical Methods
OUT	I/O Output control
TIM	Time control

A.2 Implementation of the Finite Element Scheme in OpenGeoSys

The model described in this report been integrated into the scientific GeoSys/Rockflow code, a standard Galerkin finite element solver. In the fracture, steady state fluid flow is represented by equation (54) for a unit volume

$$S_s \frac{\partial p}{\partial t} - \frac{\partial}{\partial x_\alpha}\left(\frac{k_{\alpha\beta}}{\mu}\left(\frac{\partial p}{\partial x_\beta} + \rho g \frac{\partial z}{\partial x_\beta}\right)\right) - Q_p = 0 \qquad \alpha, \beta = 1,2,3 \tag{54}$$

where S_s is the storativity coefficient [Pa^{-1}], k denotes the hydraulic conductivity tensor [m^2], p is the fluid pressure in Pa, and Q is source/sink [s^{-1}]. This equation is valid for a saturated, non-deforming porous medium with heterogeneous hydraulic conductivity. The solution of equation (54) using the finite element technique is covered in standard works such as Istok (1989), Lewis and Schrefler (1998).

Equation (54) is integrated over the model area and using the method of weighted residuals we can obtain an approximate solution to the flow equation

$$\int_\Omega \omega_i \left[S_s \frac{\partial p}{\partial t} - \frac{\partial}{\partial x_\alpha}\left(\frac{k_{\alpha\beta}}{\mu}\left(\frac{\partial p}{\partial x_\beta} + \rho g \frac{\partial z}{\partial x_\beta}\right)\right)\right] \partial\Omega = \int_\Omega \omega_i Q_p \partial\Omega \tag{55}$$

This forms a global system of equations which can be expressed as

$$C_{ij}\frac{\partial p_j}{\partial t} + K_{ij}p_j = r_i \tag{56}$$

With

$$C_{ij} = \int_\Omega \phi_i S_s \phi_j d\Omega \tag{57}$$

$$K_{ij} = \int_\Omega \frac{\partial \phi_i}{\partial x_\alpha}\frac{k_{\alpha\beta}}{\mu}\frac{\partial \phi_j}{\partial x_\beta} d\Omega \tag{58}$$

$$r_i = -\rho g K_{ij} z_i - \oint_{\partial\Omega} \phi_i q_n dS + \int_\Omega \phi_i Q_p d\Omega \tag{59}$$

The domain is decomposed into finite elements such that

$$C_{ij} = \sum_{e=1}^{ne} C_{ij}^e \tag{60}$$

$$K_{ij} = \sum_{e=1}^{ne} K_{ij}^e \tag{61}$$

$$r_i = \sum_{e=1}^{ne} r_i^e \tag{62}$$

Both for nodal weighting of the flux across the elements and the interpolation across the element the same shape functions are used, standard for the Galerkin scheme.

The interpolation functions are given as

$$\hat{p} = N_j x_\alpha p_j(t) \qquad N_j = \begin{cases} 1 & j = i \\ 0 & j \neq i \end{cases} \tag{63}$$

Using shape functions, at an element level the contributions can be given as

$$C_{ij}^e = \int_{\Omega^e} N_i S_s N_j d\Omega^e \tag{64}$$

$$K_{ij}^e = \int_{\Omega^e} \frac{\partial N_i}{\partial x_\alpha} S_s \frac{\partial N_j}{\partial x_\beta} d\Omega^e \tag{65}$$

$$r_i^e = -\rho g K_{ij}^e z_i - \oint_{d\Omega^e} N_i q_n dS + \int_{\Omega^e} N_i Q_p \, d\Omega^e \tag{66}$$

Transformation from physical (x,y,z) coordinates to local coordinates (r,s,t) allows the integrals to be evaluated using Gaussian weighting.

$$\boldsymbol{C}^e = \int_{\Omega^e} N S_s N d\Omega^e = \int_{-1}^{1}\int_{-1}^{1}\int_{-1}^{1} N S_s N \, det\, \boldsymbol{J}\, dr\, ds\, dt \tag{67}$$

$$\boldsymbol{K}^e = \int_{\Omega^e} \nabla N \frac{1}{\mu} k \nabla N^T d\Omega^e = \int_{-1}^{1}\int_{-1}^{1}\int_{-1}^{1} \nabla N (\boldsymbol{J}^{-1})^T \frac{1}{\mu} T^T k \boldsymbol{T} \nabla N \boldsymbol{J}^{-1} \, det\, J\, dr\, ds\, dt \tag{68}$$

$$\boldsymbol{r}^e = -\rho g \boldsymbol{K}^e z - \oint_{d\Omega^e} N q_n \, dS + \int_{-1}^{1}\int_{-1}^{1}\int_{-1}^{1} N Q_p \, det\, \boldsymbol{J} \, dr \, ds \, dt \quad (69)$$

These terms can be combined at a global level to give

$$\boldsymbol{r} = \boldsymbol{K}\boldsymbol{p} + \boldsymbol{C}\dot{\boldsymbol{p}} \quad (70)$$

The transient part of the equation system, $\frac{\partial p}{\partial t}$ represented as $\dot{p}$, is approximated using a finite difference approach to allow the formulation of equation system such that

$$([\boldsymbol{C}] + \omega \Delta t [\boldsymbol{K}])\{\boldsymbol{p}\}_{t+\Delta t} = ([\boldsymbol{C}] - (1-\omega)\Delta t [\boldsymbol{K}])\{\boldsymbol{p}\}_t + \Delta t\big((1-\omega)\{\boldsymbol{r}\}_t + \omega\{\boldsymbol{r}\}_{t+\Delta t}\big) \quad (71)$$

where the choice of ω controls the finite difference approximation of the time derivative, and the choice of an explicit ($\omega = 0$) or implicit ($\omega = 1$) solution.

A.3 Task C: Implementation of the H(MC) analytical closure solution in OpenGeoSys

The fracture plane is discretised into closed contact areas and open channel areas. The channel areas allow dissolution; the contact areas are undergoing pressure solution. Flow in the fracture is simulated stepwise, then the change in the fracture aperture evaluated.

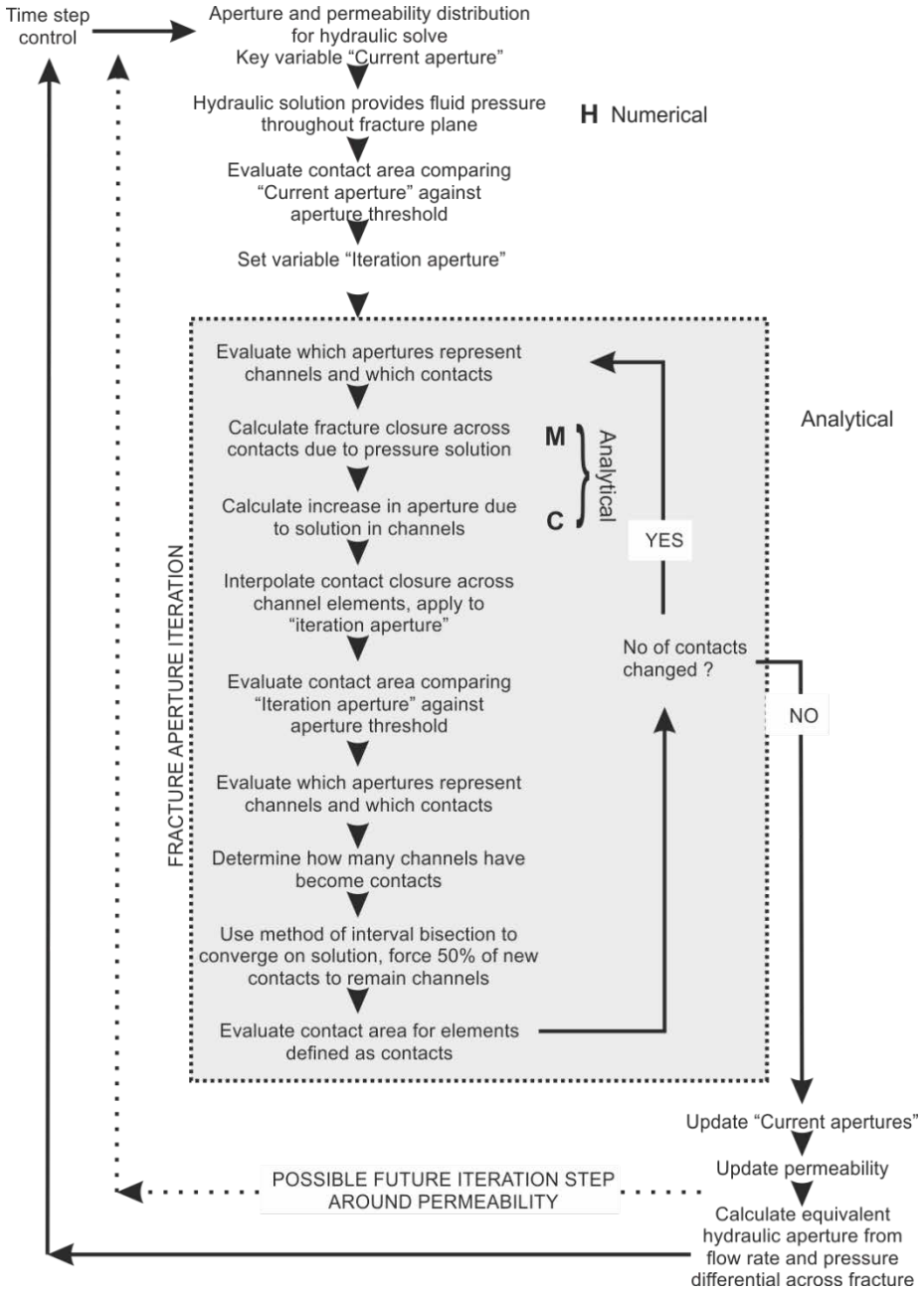

Figure A2. Diagram illustrating the implementation of the H(MC) application for fracture aperture alteration.

Locations of changes in the code

- input function in material properties file for heterogeneous fields
- permeability function dependent on aperture
- permeability model dependent on stress (trigger for analytical mechanical solve)
- during hydraulic solve call permeability model, implement in Coefficient of LaPlace matrix call
- in “Calculations of Secondary variables” after H solve call update new class level variables. Here most of the implementation of the analytical mechanical and chemical is found including iteration control for fracture closure.

At the element level member the following variables are defined

```
double initial_aperture;
double current_aperture;
double iteration_aperture;
double iteration_aperture_closure;
double element_fluid_pressure;
bool channel;
bool change;
bool allow_change;
double fracture_permeability;
double element_contact_stress;
```

At an mmp (material properties) class level the following variables are defined

```
double aperture_threshold;                    Threshold of aperture for contact
double confining_stress;                      External confining stress
double contact_area;                          Contact area of material group
double average_contact_stress;
double average_channel_aperture;
double equivalent_hydraulic_conductivity;
bool material_group_analytical_mechanical;
double dz;                                    Possible global alteration of aperture
double a;                                     a, see linear pressure solution model
double a_C;                                   a_C, see chemical solution model
```

The following member functions are implemented in the process class.

```
void CalcSecondaryVariablesAnalyticalFractureMechanics(CRFProcess* m_pcs);
long CalcSecondaryVariablesAnalyticalFractureMechanicsContactsChannels(CRFProcess*
m_pcs, int mode);
long CalcSecondaryVariablesAnalyticalFractureMechanicsEvaluateContactArea(CRFProcess*
m_pcs, int mode);
void CalcSecondaryVariablesAnalyticalFractureMechanicsInterpolateClosure(CRFProcess*
m_pcs, double max_u);
void CalcSecondaryVariablesAnalyticalFractureChemistryInterpolateOpenning(CRFProcess*
m_pcs, double max_u);
long CalcSecondaryVariablesAnalyticalFractureMechanicsSortChanges(CRFProcess* m_pcs);
void CalcSecondaryVariablesAnalyticalFractureMechanicsUpdateApertures(CRFProcess*
m_pcs);
```

At an element level the actual contact stress is evaluated by subtracting the fluid pressure from the average contract stress. For ease the formulation is given again, at an element level

$$\frac{\partial b}{\partial t} = -a(\sigma_c - u)^c \quad (72)$$

The amount of material lost through pressure solution per element is calculated, and summed. This provides a solution for Δb_t which is then weighted across the whole fracture plane. The iteration is controlled such that the change in fracture aperture is not allowed to exceed 5% of the fracture aperture at any time. The control being provided by the time step.

Once the total amount of closure across the model is known as the contacts close, the closure needs to be distributed to the channel. Currently the distribution is weighted according to the fluid pressure in the channel. That is, areas with lower fluid pressure see higher aperture change than those with high fluid pressure. The element weighting factors, w_{el}, are given by

$$w_{el} = \left(1 - \frac{u_e}{max(u_e)}\right) + 0.5 \quad (73)$$

where u_e is the fluid pressure in the element, and max u_e the largest fluid pressure seen in the whole of the fracture plane. The aperture change for the channel elements is given as

$$b_{el} = b_t \cdot w_{el} \quad (74)$$

Future improvement will include the development of an interpolation model with a distance weighting function to reflect the redistribution of stress across the fracture surface.

Appendix B – QPAC Formulation

Here follows a brief description of the formulation of QPAC and the pre-built process sets (modules) that are available for use.

B.1 System Discretisation

The modelled system can be broken down into a number of *subsystems*. Inside each subsystem the set of processes to be modelled is defined. In a systems-level model, separate subsystems will often be used to represent different parts of the system, where the types of processes that are being modelled vary. In a detailed model, separate subsystems can be used to break the system down in order to reduce the amount of work to be done (i.e. reduce the number of variables to be solved for).

Each subsystem is broken down into *compartments* (sometimes referred to as control volumes) with interfaces between these. In every compartment in a given subsystem the set of processes that may be active is the same.

Subsystems can be linked by *joiners*. Joiners control how quantities simulated in one subsystem affect, or are transported into, the other subsystem.

Collections of compartments corresponding to Cartesian or cylindrical polar grids can be defined, or compartments can be specified individually (not in grids), which need not necessarily have a fixed location in space and the collections need not be 'space filling'. Grids and individually specified compartments can both be used within the same subsystem and their positions and volumes may change with time.

Discretisation in QPAC is illustrated in Figure B1.

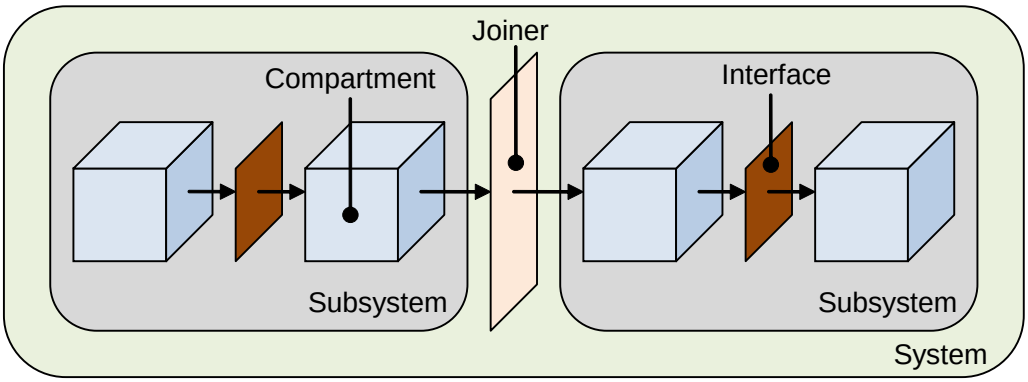

Figure B1: Discretisation in QPAC

B.2 Process Models and Variables

Both evolving and algebraic variables are considered in QPAC. Evolving variables are those whose evolution in time is determined by an ordinary differential equation, with given initial conditions; algebraic variables are constrained by the solution of algebraic (non-differential) equations. If the evolving variables are written as U_E and the algebraic ones as U_A then QPAC can solve equations of the form

$$\begin{aligned} \dot{U}_E &= f(U_E, U_A, t) \\ 0 &= g(U_E, U_A, t). \end{aligned} \tag{75}$$

Here the U_E represents local values for globally conserved quantities (e.g., mass, or energy) and a dot indicates a derivative with respect to time, *t*. Writing the full set of variables as U this can be generalised to:

$$m(\dot{U}, U, t) = f(U, t)\,. \tag{76}$$

The function m is referred to as a mass function, which is just $\dot{U}_E$ for a conserved quantity. It is more general than the mass matrix that arises in finite element approaches and has a different purpose. The mass function arises from the physical equations whereas the finite-element mass matrix arises from the discretisation scheme. Rows of *m* corresponding to algebraic variables evaluate to zero.

A distinction is made between compartment and interface (including boundary) variables. In a single subsystem each compartment has the same set of variables and each interface can have a second set of variables. There is no difference in the way that algebraic variables are handled, but evolving variables are treated differently in compartments and on interfaces. If U is an evolving compartment variable, then

$$m(\dot{U}, U, t) = \sum_I (\pm) F_I(U, t) + S_C(U, t)\,. \tag{77}$$

Here $S_C(U,t)$ are sources within the compartment (depending on variables within the compartment) and $F_I(U,t)$ are fluxes across the compartment interfaces (depending on variables on the interface and within the two compartments that share it). Boundaries are treated as interfaces with only one associated compartment and fluxes are applied consistently to the compartments connected by a given interface in order to ensure conservation of the evolving variables. The source part of the equation can also be used for reactions within a compartment, for example simple decay processes.

On an interface, evolving variables only have the source part of the equation; they can be used, for example, to calculate an integrated flux over time across an interface.

The functional forms that can be used for the source and flux terms are completely general, since QPAC allows any algebraic expression to be used to relate properties to variables and then to use these properties in the specification of the sources and fluxes.

In summary, QPAC can solve a general system of differential and algebraic equations within a compartmentalised system. The form of these equations is determined by the particular model being implemented. The equations that QPAC solves need not arise from a system of partial differential equations, but when a system of partial differential equations is to be solved, the discretisation of these equations is part of the model specification.

B.3 The Finite Volume Method

Although QPAC does not impose the approach that is to be used for spatially discretising the system of partial differential equations (PDEs), the finite volume (or control volume) approach is generally used (see, for example, Versteeg and Malalasekra, 2007). It is possible to implement directly a finite-difference approach and in simple cases this will lead to the same equations as the finite volume approach.

In the finite volume method, volume integrals in a PDE that contain a divergence term can be converted to surface integrals, using the divergence theorem, enabling the original partial differential equation to be replaced by ordinary differential equations for the volume-averaged variables. Advantages of this approach include:

- It does not require a structured grid, although a structured grid can be used.
- Problems on irregular geometries can be considered.
- Because the flux entering a given volume is identical to that leaving the adjacent volume, variables are readily conserved.
- Boundary conditions are easy to apply.

The alternative approach that is commonly used for continuum problems is the finite element approach. This shares some of the advantages of the finite volume approach, particularly in handling irregular geometries. The most significant difference between the approaches is in the way that fluxes between volumes are treated. In the finite volume approach there is a clear flux between volumes, ensuring that the relevant quantity (e.g. mass) is conserved locally. In the finite element approach, there is no unique flux between elements – the normal gradients will generally differ across the interface – and local conservation is lost. For application areas where QPAC has been used, local conservation of evolving quantities (such as mass) and the ability to see how these are transported through the system are important – hence the choice of the finite volume approach.

Consider, for example, a system of PDEs for a conserved quantity u

$$\frac{\partial u}{\partial t} = \nabla \cdot J(u,t) + q(u,t), \tag{78}$$

where J is a flux term and q is a source term. Within a particular volume (a compartment), the above equation is solved in an averaged sense, so that

$$\int_V \frac{\partial u}{\partial t} dV = \int_V \nabla \cdot J(u,t)\, dV + \int_V q(u,t)\, dV . \tag{79}$$

Using the divergence theorem, this becomes

$$\int_V \frac{\partial u}{\partial t} dV = \int_{\partial V} J(u,t) \cdot \underline{n}\, dA + \int_V q(u,t)\, dV \,, \tag{80}$$

where ∂V denotes the boundary of the volume, $\underline{n}$ is normal to that boundary and A is the surface area.

The compartment variable relates to the volume integral

$$\int_V u\, dV \rightarrow U_C \,, \tag{81}$$

the boundary of the volume is split into the various interfaces so that

$$\int_I J(u,t) \cdot \underline{n}\, dA \rightarrow F_I \,, \tag{82}$$

and the final sources and reactions term becomes the compartment source,

$$\int_V q(u,t)\, dV \rightarrow S_C \,. \tag{83}$$

Typically, the flux terms will involve local gradients which become differences in the discretised scheme. This can be done with just compartment variables, taking appropriate averages of any properties that are involved. The approach that is generally taken in QPAC models is to define an interface variable to be an average of the continuous variable on the interface and to use this in defining the flux on the interface. The value of the interface variable is determined by imposing the required flux consistently across an interface which gives a guarantee of conservation of mass or energy.

The source term is commonly treated by using the averaged variable directly, so that

$$S_C = Vq\left(\frac{U_C}{V}, t\right). \tag{84}$$

This implicitly assumes that the variable of interest is uniformly distributed in the compartment. If this is known to be inappropriate, other averaging could be used and the integral could be evaluated explicitly or approximately.

Where a compartment is adjacent to the external boundary, the flux term will be determined by the boundary condition. If a Neumann (specified flux) condition applies, then this is used directly. If a Dirichlet (fixed value) condition is specified, then this determines the value of the interface variable and again is simply handled.

B.4 Modules

The modules that are currently available include:

Thermal processes. (Bond, 2010) This is a comparatively simple module where the standard equations for heat conduction, convection and radiation are implemented.

Multiphase phase flow (MPF). (Bond and Benbow, 2009) Several modules for the representation of fluid flow in porous media have been developed. The 'classic' multiphase flow relationships effectively assume a well-mixed disposition of fluids with the relative permeability for a compartment being isotropic. This approach is applied where the saturation changes over length scales large in comparison with the grid size. An alternative conceptual model is that used for large-scale groundwater flow modelling, where the fluids are assumed to be poorly mixed and there is a distinct 'free-surface'. This conceptual model is typically used where the grid size is large in comparison with the length scale over which the saturation changes and where capillary effects are of secondary importance.

Tracer transport. (Robinson, 2010) In conjunction with fluid flow calculations, it is often required to model the transport of trace materials or contaminants. The processes modelled include: advection with dispersion; diffusion; equilibrium sorption; solubility limitation; and radioactive decay and ingrowth. Matrix diffusion is a special case of the diffusion process; it is generally modelled as a one-dimensional process perpendicular to the flow direction along a fracture.

Reactive transport. (Benbow and Watson, 2011) This module is designed to simulate the chemical interactions of groundwater and other subsurface fluids with rocks and manmade materials. These interactions play an important role in both fundamental geological processes and the evolution of engineered structures. In an open system the interactions in the water-rock system are represented by reactive transport equations, which couple the fluid flow equations to those representing the geochemical reactions between the porewater components and the solid materials. The equations are fully coupled in the sense that alteration processes in the rock and manmade materials feed back into the fluid flow through variations in porosity and other material properties such as permeability and tortuosity.

Mechanical processes. (Bond, 2013a). This module allows the representation of classical small-strain elastic deformations in structured and unstructured grids, for both transient (e.g. pressure waves) and instantaneous static analyses. The module supports non-linear elasticity, orthotropic anisotropy, poro-elasticity and thermo-elasticity. In addition the module allows the user to couple-in arbitrary non-elastic strains, providing the capability to include customised elastic-plastic or visco-elastic models. The Mohr-Coulomb failure model, modified Cam-Clay model and various ‘creep’ models have all been used successfully with the mechanical module.

AMEC
Registered Address:
Booths Park
Chelford Road
Knutsford
Cheshire
WA16 8QZ